universität wien

DIPLOMARBEIT

Titel der Diplomarbeit

„Properties of silicon nitride – An *ab-initio* study of the crystalline phases and amorphous silicon-nitrogen alloys“

Verfasser

Thomas Watts

angestrebter akademischer Grad

Magister der Naturwissenschaften (Mag.rer.nat.)

Wien, 2011

Studienkennzahl lt. Studienblatt:	A 411
Studienrichtung lt. Studienblatt:	Physik
Betreuerin / Betreuer:	Univ.-Prof. Dipl.Ing. Dr. Georg Kresse

Contents

Zusammenfassung

Theoretische *Ab-initio* Methoden haben sich in der Materialphysik etabliert, da sie wichtige Erkenntnisse liefern als Bestätigung, Ergänzung und Erweiterung von experimentellen Befunden. Die gegenständliche Studie berechnet physikalische Eigenschaften von kristallinem Siliziumnitrid und amorphen Silizium-Stickstoff Legierungen mit dem Vienna *Ab-initio* Simulation Package VASP, welches auf der Dichtefunktionaltheorie basiert. Die Arbeit implementiert ein optimiertes Potential zur Behandlung der amorphen Legierungen mittels vorhergehender Bestimmung der strukturellen, elektronischen, optischen und Schwingungseigenschaften von α-, β-, und γ-Si_3N_4 mit einem regulären Potential.
Es wird bestätigt, dass es sich bei der Raumgruppe der stabilen Phase, β-Si_3N_4, um $P6_3m$ handelt. Die generelle Bandstruktur von kristallinem Siliziumnitrid zeigt zwei flache Valenzbänder, welche durch eine Lücke getrennt werden. Breite indirekte Kohn-Sham PBE Bandlücken zwischen 3.3 eV und 4.7 eV werden beobachtet, wie auch optische Absorption ab Photonenenergien von 5.0 eV. Schwingungsfrequenzen von 180 cm^{-1} bis 1030 cm^{-1} treten auf. Sodann werden die Berechnungen der kristallinen Phasen mit den optimierten Potentialen durchgeführt und verglichen. Es wird gezeigt, dass die Potentiale zur Behandlung der amorphen Legierungen angemessen sind. Ein optimiertes Potential wird ausgewählt und zur Berechnung der strukturellen und elektronischen Eigenschaften von hydrierten und unhydrierten amorphen Silizium-Stickstoff Legierungen eingesetzt.
Den Hauptfokus stellen die Legierungen a-Si_3N_3, a-Si_3N_4, a-Si_3N_3:H und a-Si_3N_4:H dar. Eine Bestimmung der mittleren Abstandsquadrate und Diffusionskoeffizienten, der partiellen Paarkorrelationsfunktionen, der Bindungswinkelverteilungen, der Koordinationszahlen und der strukturellen Defekte wird durchgeführt. Die elektronische Struktur von Valenzband, Leitungsband und Bandlücke sind ähnlich wie die der kristallinen Phasen. Die amorphen Silizium-Stickstoff Legierungen weisen KS PBE Bandlücken von 1.4 eV bis 2.8 eV auf, je nach Stöchiometrie Si/N und Wasserstoffgehalt. Festgestellt wird eine Tendenz zur Bandlückenaufweitung für an Si_3N_4 annähernde Stöchiometrien sowie, obwohl weniger ausgeprägt, für hydrierte Legierungen. Die Hydrierung zeigt einen ausheilenden Effekt auf elektronische Defektzustände durch Reduzierung der Lokalisierung von Valenzelektronen. Wasserstoff bildet Bindungen zu N sowie Si in a-Si_3N_3:H, aber bevorzugt N in a-Si_3N_4:H. Zustände in der Bandlücke werden in a-Si_3N_3 und a-Si_3N_3:H beobachtet. Energielevels in der Nähe des Valenzbandes stammen großteils von Koordinierungsdefekten, jedoch Zustände beim Leitungsband sind durch Beiträge von Atomen innerhalb des Si Perkolationsnetzwerkes ausgezeichnet. Es wird bestätigt, dass, neben dem Auftreten struktureller Defekte, je mehr Si Atome Teil des Perkolationsnetzwerkes sind, desto mehr schrumpft die Bandlücke aufgrund Lokalisierung von Defektzuständen.

Abstract

Theoretical *ab-initio* methods have been established in materials physics, as they supply important insights to verify, supplement and extend experimental findings. The present study calculates physical properties of crystalline silicon nitride and amorphous silicon-nitrogen alloys with the Vienna *ab-initio* simulation package VASP, based on density functional theory. We implement an optimized potential for treating the amorphous alloys by first determining structural, electronic, optical and vibrational properties of α-, β-, and γ-Si_3N_4 with a regular potential.
The space group of the stable polymorph, β-Si_3N_4, is confirmed as $P6_3m$. In general, the band structure of crystlline silicon nitride exhibits two flat valence bands separated by a gap. Wide indirect Kohn-Sham PBE band gaps between 3.3 eV and 4.7 eV are observed as well as an absorption of photons above 5.0 eV. Vibrational frequencies range from 180 cm^{-1} to 1030 cm^{-1}. Then the calculations of the crystalline phases are performed with the optimized potentials and compared. In following we establish that the potentials are adequate for treating the amorphous alloys. One optimized potential is selected and used for obtaining the structural and electronic properties of amorphous silicon-nitrogen alloys, unhydrogenated and hydrogenated.
The main focus is placed on a-Si_3N_3, a-Si_3N_4, a-Si_3N_3:H and a-Si_3N_4:H. A determination of mean square displacements and diffusion coefficients, partial pair correlation functions, bond angle distributions, coordination numbers and structural defects is conducted. The electronic structures of valence band, conduction band and band gap are similar to those of the crystalline phases. The amorphous silicon nitrogen alloys display KS PBE band gaps between 1.4 eV and 2.8 eV, depending on stoichiometry and hydrogen content. We observe a tendency of band gap widening for stoichiometry approaching a-Si_3N_4 and, less distinct but noticeable, for hydrogenated alloys. Hydrogenation has a curing effect on the electronic levels of defects, by reducing the localization of valence electrons. Hydrogen bonds to N and Si in a-Si_3N_3:H, but prefers N in a-Si_3N_4:H. Gap states are observed in a-Si_3N_3 and a-Si_3N_3:H. Levels close to the valence band originate mainly from coordination defects, whereas the levels in the vicinity of the conduction band are dominated by contributions from atoms within the Si random percolation network. We confirm that, aside from structural defects, the more Si atoms are part of the random percolation network, the more the band gap decreases due to tailing of levels into the gap.

Chapter 1

Introduction

The present work applies density functional theory with the Vienna *ab-initio* simulation package VASP to the insulator silicon nitride. Silicon nitride is used as deposited surface layer for high performance silicon solar cells [1]. It is also suitable for high temperature ceramics applications [2], due to its tensile strength. In the amorphous alloys there is an uncertainty in stoichiometry depending on the formation process, additionally usually some hydrogen is present. Thus the formula Si_3N_4 is only applicable for the crystalline phases or for the pure amorphous alloy.

The main focus of this work is the modelling of amorphous silicon nitride and amorphous silicon-nitrogen alloys. Specifically of interest is the issue of structural defects and the connection to electronic states, as well as possible curing of defects through hydrogenation. Hydrogen has been found to have a passivating effect [3], thus the principal bonding partner and the effect of hydrogenation on the electronic defect levels are investigated in this work. A previous study [4] suggests that structural defects are not easily assigned to specific electronic levels in the band structure of the amorphous silicon-nitrogen alloys. Therefore a thorough analysis of the local environment is performed in combination with an assignment of localized electronic states at certain energy levels to specific atoms.

The considered structural defects are under- and overcoordinated atoms, Si clusters and random percolation networks, square structures, N vacancies and Si antisites. Si clusters and random percolation networks are bound to exist if not sufficient N is present to saturate every Si dangling bond. Experimental findings are scarce and show conflicting tendencies [5, 6]. Recent calculations point to formation of such networks [4]. Thus the conditions for appearance of a Si network are investigated by performing calculations with two different Si/N-ratios.
The square structure has been previously documented in *ab-initio* simulations [7] and experimentally as nitrogen defect in amorphous silicon [8]. It is best described as a four-membered ring of alternating Si and N atoms arranged in a quasi-planar square. As each Si atom shares two N atoms with another Si atom in this configuration, the resulting tetrahedra centered on the Si atoms are edge-sharing. The regular configuration in crystalline α- and β-Si_3N_4 contains only corner-sharing SiN_4 tetrahedra, whereas in the high pressure phase γ-Si_3N_4 edge-sharing tetrahedra are present. The dominance of one type of configuration over the other is inspected in the amorphous silicon-nitrogen alloys.
Reference [9] suggests two more structural defects, the N vacancy and the Si antisite. Basically, in reference [9] the N vacancy was modelled by removing one nitrogen atom from a crystalline Si_3N_4 network, thus the silicon neighbors are left undercoordinated. In this work the N vacancy is not treated as a separate defect, but considered indirectly through threefold coordinated Si atoms. The Si antisite in reference [9] was obtained by replacing one nitrogen atom in a crystalline Si_3N_4 network by a silicon atom. This can be regarded as an extreme case of a percolation network, in which one quarter of the Si atoms are threefold coordinated. In the present work, the Si antisite is analysed together with other Si atoms within the random percolation network.

Creation of the amorphous models requires long and slow annealing, therefore optimized potentials are used that need to be tested beforehand. This diploma thesis first gives a short introduction on density functional theory and the applied methods in chapter 2. Chapter 3 contains the results of calculations for the crystalline phases with a regular reference potential. These are treated as reference values for the same calculations with two different optimized potentials in chapter 4, a soft and a very soft potential. After the reliability of the optimized potentials has been established, the very soft potential is used in chapter 5 to obtain the amorphous model structures. The conclusions in chapter 6 sum up the findings of this work.

Chapter 2

Density functional theory

This chapter begins with the time-independent many electron Schrödinger equation for describing solids quantum mechanically. Then the basic theorems of density functional theory are given and the energy functional in Kohn-Sham formalism is presented. The quantum mechanic harmonic theory of vibrations is used to determine the crystal's potential energy and the Bloch theorem is applied to electronic wave functions in the crystal's periodic potential. Implementation of the density functional theory procedure and methods in VASP is then outlined. The computational details selected in this work are given.

2.1 Many electron Schrödinger Equation

Quantum mechanically, properties of solids are obtained with the time-independent many particle Schrödinger equation. This partial differential equation handles solids as a system of electrons and nuclei through stationary wave functions. The time-independent many particle Schrödinger equation is

$$\hat{H}^{\text{fund}}\psi(\mathbf{r}_1,\mathbf{r}_2,...,\mathbf{r}_N;\mathbf{R}_1,\mathbf{R}_2,...,\mathbf{R}_M) = E^{\text{fund}}\psi(\mathbf{r}_1,\mathbf{r}_2,...,\mathbf{r}_N;\mathbf{R}_1,\mathbf{R}_2,...,\mathbf{R}_M)\,, \tag{2.1}$$

where E^{fund} is the total energy of the system and the eigenvalue of the fundamental Hamiltonian $\hat{H}^{\text{fund}}$. The $\psi(\mathbf{r}_1,\mathbf{r}_2,...,\mathbf{r}_N;\mathbf{R}_1,\mathbf{R}_2,...,\mathbf{R}_M)$ denote stationary wave functions that depend on the positions $\mathbf{r}_1,\mathbf{r}_2,...,\mathbf{r}_N$ of the electrons and $\mathbf{R}_1,\mathbf{R}_2,...,\mathbf{R}_M$ of the nuclei. Contributions to the total energy E^{fund} from electrons as well as from nuclei have to be regarded. This is performed with the fundamental Hamiltonian

$$\hat{H}^{\text{fund}} = \hat{T}_e + \hat{T}_n + \hat{U}_{ee} + \hat{U}_{en} + \hat{U}_{nn}\,. \tag{2.2}$$

The index e stands for electronic contributions and n for contributions from nuclei in the kinetic energies $\hat{T}$ and potential energies $\hat{U}$. This Hamiltonian is more explicitly given as

$$\begin{aligned}\hat{H}^{\text{fund}} = &-\frac{\hbar^2}{2m_e}\sum_{i=1}^{N}\nabla_i^2 - \sum_{n=1}^{M}\frac{\hbar^2}{2M_n}\nabla_n^2 + \frac{e^2}{2}\sum_{i,j=1;i\neq j}^{N}\frac{1}{|\boldsymbol{r}_i-\boldsymbol{r}_j|}\\ &-\sum_{n}^{M}\sum_{i}^{N}\frac{Z_n e^2}{|\boldsymbol{r}_i-\boldsymbol{R}_n|} + \frac{e^2}{2}\sum_{n,m=1;n\neq m}^{M}\frac{Z_n Z_m}{|\boldsymbol{R}_n-\boldsymbol{R}_m|}\,.\end{aligned} \tag{2.3}$$

In equation (2.3) N and M are the number of electrons and nuclei, respectively. $\boldsymbol{r}_i, \boldsymbol{r}_j$ denote the locations of the electrons and $\boldsymbol{R}_n, \boldsymbol{R}_m$ those of the nuclei. $e = 1.60219\cdot10^{-19}$ C is the elementary charge, $\hbar = 1.054572\cdot10^{-34}$Js $= 6.582119\cdot10^{-16}$eV s the reduced Planck constant, $m_e = 9.1096\cdot10^{-31}$ kg the electron mass, $M_n = 1.6726\cdot10^{-27}$ kg the proton mass and Z the atomic number. The first and second term in the Hamiltonian $\hat{H}^{\text{fund}}$ describe the kinetic energy of electrons $\hat{T}_e$ and nuclei $\hat{T}_n$, respectively. The third

and fifth term give the repulsive interactions between particles of the same type, namely electron-electron interaction $\hat{U}_{ee}$ and nuclei-nuclei interaction $\hat{U}_{nn}$. The fourth term in equation (2.3) denotes the electron-nuclei interaction $\hat{U}_{en}$. The kinetic energy contribution $\hat{T}_n$ of the nuclei is a constant shift and can therefore be chosen as $\hat{T}_n = 0$, reducing the terms of the fundamental Hamiltonian to

$$\hat{H}^{\text{fund}} = \hat{T}_e + \hat{U}_{ee} + \hat{U}_{en} + \hat{U}_{nn} \,. \tag{2.4}$$

In the static nuclei approximation, as applicable for a crystal lattice or an amorphous solid, the classical positions $\mathbf{R}_1, \mathbf{R}_2, ..., \mathbf{R}_M$ of the nuclei in the structure are fixed. Thus in the Hamiltonian for constant positions of the nuclei the term $\hat{U}_{nn}$ is also constant. The potential energy contribution $\hat{U}_{en}$ is considered as a lattice periodic potential for the electrons

$$V^{\text{ext}}(\mathbf{r} + \mathbf{R}) = V^{\text{ext}}(\mathbf{r}) \,, \tag{2.5}$$

where $\mathbf{R}$ is an arbitrary lattice vector. The static nuclei Hamiltonian is

$$\hat{H} = \hat{T}_e + \hat{U}_{ee} + V^{\text{ext}} \,. \tag{2.6}$$

The static nuclei Hamiltonian $\hat{H}$ solves the many electron Schrödinger equation

$$\hat{H}\psi(\mathbf{r}_1, \mathbf{r}_2, ..., \mathbf{r}_N) = E\psi(\mathbf{r}_1, \mathbf{r}_2, ..., \mathbf{r}_N) \,, \tag{2.7}$$

with the many electron wave functions $\psi(\mathbf{r}_1, \mathbf{r}_2, ..., \mathbf{r}_N)$.

2.2 Hohenberg-Kohn theorems and Kohn-Sham method

The theoretical foundation of density functional theory are the Hohenberg-Kohn theorems [10]. They state that for a class of Hamiltonians of the form of equation (2.6) the energy is a functional of the density. The energy functional is expressed as

$$E[n(\mathbf{r})] \equiv \int V^{\text{ext}}(\boldsymbol{r}) n(\boldsymbol{r}) d^3r + F[n] \tag{2.8}$$

with a universal functional

$$F[n] = \min_{\psi|n} \left[\langle\psi| \hat{T}_e + \hat{U}_{ee} |\psi\rangle \right] . \tag{2.9}$$

It results in the correct ground state energy associated with $V^{\text{ext}}(\boldsymbol{r})$. In the Kohn-Sham method [11] a one particle Hamiltonian for a non-interacting reference system is defined

$$\hat{H}^{\text{KS}} = \hat{T}_e + V^{\text{KS}} \,. \tag{2.10}$$

The ansatz for the Kohn-Sham potential is

$$V^{\text{KS}}(\mathbf{r}) = V^{\text{ext}}(\mathbf{r}) + V^{\text{H}}(\mathbf{r}) + V^{\text{XC}}(\mathbf{r}) \,. \tag{2.11}$$

$V^{\text{ext}}(\mathbf{r})$ is the lattice periodic potential of the nuclei, $V^{\text{H}}(\mathbf{r})$ is the electrostatic or Hartree potential and $V^{\text{XC}}(\mathbf{r})$ is the exchange-correlation potential.

Thus the energy functional is

$$E[n] = \hat{T}_e[\psi_1, \psi_2, \ldots, \psi_N] + E^{\mathrm{H}}[n] + E^{\mathrm{ext}}[n] + E^{\mathrm{XC}}[n] + E^{\mathrm{ion}}\,, \tag{2.12}$$

with

$$\hat{T}_e = -\frac{\hbar^2}{2m_e}\sum_i^N \left\langle \psi_i(\mathbf{r})|\nabla_i^2|\psi_i(\mathbf{r})\right\rangle \qquad \text{the electronic kinetic energy}$$

$$E^{\mathrm{H}}[n] = \frac{e^2}{2}\int d^3r d^3r' n(\mathbf{r}')\frac{1}{|\mathbf{r}-\mathbf{r}'|}n(\mathbf{r}) \qquad \text{the (electrostatic) Hartree energy}$$

$$E^{\mathrm{ext}}[n] = \int d^3r V^{\mathrm{ext}}(\mathbf{r})n(\mathbf{r}) \qquad \text{the electronic energy in potential of nuclei}$$

$$E^{\mathrm{XC}}[n] \qquad \text{the exchange-correlation energy}$$

and E^{ion} the electrostatic energy from nuclei-nuclei interaction.
The Kohn-Sham potential $V^{\mathrm{KS}}(\boldsymbol{r})$ solves the Kohn-Sham equations

$$\varepsilon_i\psi_i(\boldsymbol{r}) = \left[-\frac{\hbar^2}{2m_e}\nabla^2 + V^{\mathrm{KS}}(\boldsymbol{r})\right]\psi_i(\boldsymbol{r})\,, \tag{2.13}$$

$$n(\boldsymbol{r}) = \sum_i^N |\psi_i(\boldsymbol{r})|^2\,, \tag{2.14}$$

where equation (2.14) is the condition for self consistency. Summation over the energy eigenvalues ε_i results in

$$\begin{aligned}\sum_{i=1}^N \varepsilon_i =& \sum_{i=1}^N \left\langle \psi_i(\mathbf{r})|\hat{H}^{\mathrm{KS}}|\psi_i(\mathbf{r})\right\rangle = \\ =& \hat{T}_e[\psi_1, \psi_2, \ldots, \psi_N] + 2E^{\mathrm{H}}[n_0] + E^{\mathrm{ext}}[n_0] + \int d^3r n_0(\mathbf{r})E^{\mathrm{XC}}[n_0(\mathbf{r})]\,.\end{aligned} \tag{2.15}$$

By comparison with the energy functional in equation (2.12) the Kohn-Sham energy functional for the ground state density n_0 results in

$$E^{\mathrm{KS}} \doteq E[n_0] = \sum_{i=1}^N \varepsilon_i - E^{\mathrm{H}}[n_0] + E^{\mathrm{XC}}[n_0] - \int d^3r V^{\mathrm{XC}}[n_0(\mathbf{r})]n_0(\mathbf{r}) + E^{\mathrm{ion}}\,. \tag{2.16}$$

2.3 Quantum harmonic crystal

The potential energy of the nuclei in the crystal lattice is obtained within the framework of the quantum theory of crystals [12]. The Hamiltonian for the movement of the nuclei is formulated in the harmonic approximation

$$\hat{H}^{\text{harm}} = \hat{T}_n + \hat{U}_{nn}\,. \tag{2.17}$$

The energy eigenvalues E_i' of stationary state i of the crystal are obtained from considerations concerning the lattice vibrations, or phonons. A N-atomic crystal can be described as a system of coupled harmonic oscillators. With linear transformation normal coordinates can be introduced which lead to equations of motion for independent oscillators. Each of the $3N$ normal modes with frequency $\omega_s(\mathbf{k})$ contributes a discrete set of values $(n_{\mathbf{k}s} + \frac{1}{2})\hbar\omega_s(\mathbf{k})$ to the energy of the crystal in the stationary state i

$$E_i' = \sum_{\mathbf{k}s}(n_{\mathbf{k}s} + \frac{1}{2})\hbar\omega_s(\mathbf{k})\,. \tag{2.18}$$

$n_{\mathbf{k}s} = 0, 1, 2, \ldots$ are the excitation numbers of the normal mode of branch s with wave vector $\mathbf{k}$. s ($s = 1, \ldots, 3N$) denotes the different dispersion branches. Instead of using the description that the normal mode of branch s with wave vector $\mathbf{k}$ is in its $n_{\mathbf{k}s}$th excited state, it is equivalent to say that there are $n_{\mathbf{k}s}$ phonons of type s with wave vector $\mathbf{k}$ present in the crystal. The frequency branches $\omega_s(\mathbf{k})$ have the periodicity of the reciprocal lattice. The acoustic branches with $\omega = c\mathbf{k}$ are characteristic of sound waves, at small $\mathbf{k}$. They vanish linearly with $\mathbf{k}$ in the long-wavelength limit. Optical branches do not vanish in the long-wavelength limit. The phonon dispersion curve of a N-atomic crystal has 3 acoustic and $3(N-1)$ optical branches, totalling $3N$.

The expectation value of the crystal's energy is formulated in the canonical ensemble as

$$E^{\text{harm}} = \frac{\sum_i E_i' \exp(-\beta E_i')}{\sum_i \exp(-\beta E_i')}\,, \tag{2.19}$$

where E_i' is the energy of stationary state i of the crystal and $\beta = 1/k_B T$ with the Boltzmann constant $k_B = 8.617$ eV K^{-1}. By inserting the E_i' from equation (2.18) the expectation value of the energy of a quantum mechanic harmonic crystal at temperature T is

$$E^{\text{harm}} = E^{\text{eq}} + \sum_{\mathbf{k}s}\frac{1}{2}\hbar\omega_s(\mathbf{k}) + \sum_{\mathbf{k}s}\frac{\hbar\omega_s(\mathbf{k})}{\exp(\beta\hbar\omega_s(\mathbf{k})) - 1}\,. \tag{2.20}$$

The second term denotes the zero point vibrations of the normal modes and E^{eq} the energy of the equilibrium configuration. The energy of the equilibrium configuration is

$$E^{\text{eq}} = \frac{1}{2}\sum_{\mathbf{r}\mathbf{r}'}\phi(\mathbf{r} - \mathbf{r}') = \frac{N}{2}\sum_{\mathbf{r}\neq 0}\phi(\mathbf{r})\,. \tag{2.21}$$

if $\phi(\mathbf{r} - \mathbf{r}')$ is the potential contribution from a pair of nuclei and the summation goes over pairs $\mathbf{r}\mathbf{r}'$ of nuclei.

2.4 Bloch electrons in a periodic potential

Any three dimensional crystal consists of a lattice $\{n_1\mathbf{R}_1 + n_2\mathbf{R}_2 + n_3\mathbf{R}_3, n_i \in \mathbb{Z}\}$. Reciprocal lattice vectors $\{\mathbf{G}_1, \mathbf{G}_2, \mathbf{G}_3\}$ can be defined that relate to the lattice vectors through

$$\mathbf{R}_i\mathbf{G}_j = 2\pi\delta_{ij}\,. \tag{2.22}$$

According to the Bloch theorem the eigenstates or wave functions ψ to the single electron Hamiltonian with lattice periodicity can be described as

$$\psi_{n\mathbf{k}}(\mathbf{r}) = \mathsf{u}_{n\mathbf{k}}(\mathbf{r})\exp(i\mathbf{k}\mathbf{r}) = \sum_{\mathbf{G}} c_{n\mathbf{k}}(\mathbf{k}+\mathbf{G})\exp(i\mathbf{r}(\mathbf{k}+\mathbf{G}))\,. \tag{2.23}$$

The condition is that the function $\mathsf{u}_{n\mathbf{k}}$ is lattice periodic $\mathsf{u}_{n\mathbf{k}}(\mathbf{r}) = \mathsf{u}_{n\mathbf{k}}(\mathbf{r}+\mathbf{R})$. As the single electron wave functions ψ are used in the Kohn-Sham equations (2.13), the Bloch theorem is applicable in density functional theory for periodic structures. Amorphous structures can also be calculated if the super cell contains sufficient formula units so that after *simulated annealing*, which is discussed later, the resulting distribution can be considered random. This super cell is periodically repeated into all three spatial dimensions and a quasi-random crystal is used for the determination of the amorphous solid's properties.

2.5 Vienna Ab-Initio Simulation Package

In this work the Vienna Ab-Initio Simulation Package (VASP) is used to perform density functional theory calculations. A number of methods are implemented to efficiently solve the Kohn-Sham equations. Specifically, the Bloch theorem is used. Thus only the smallest unit cell is required to build up the crystal. Also, that the single electron energies can be obtained as continuous functions of crystal impulse $\mathbf{k}$ is considered by $\mathbf{k}$-point sampling. Lastly, the wave functions can be formulated with the PAW method.

Numerically a basis set is constructed to describe the Bloch electrons, for which VASP applies a cut-off energy E_{cut}

$$\frac{\hbar^2}{2m}|\mathbf{k}+\mathbf{G}_{\max}|^2 < E_{\text{cut}}\,, \tag{2.24}$$

where $\mathbf{G}_{\max}$ is the maximal reciprocal lattice vector used in the plane wave expansion. The cut-off energy is related to the choice of $\mathbf{k}$-point mesh. The larger the number of $\mathbf{k}$-points, the lower E_{cut} can be. If the expansion of the potential from equation (2.11), $V^{\text{KS}}(\mathbf{r}) = V^{\text{ext}}(\mathbf{r}) + V^{\text{H}}(\mathbf{r}) + V^{\text{XC}}(\mathbf{r})$, is performed with lattice periodic plane waves

$$V(\mathbf{r}) = \sum_{\mathbf{G}} V(\mathbf{G})\exp\left(i\mathbf{r}\mathbf{G}\right), \tag{2.25}$$

the Kohn-Sham equations present themselves as a system of equations for coefficients $c_{n\mathbf{k}}(\mathbf{k}+\mathbf{G})$ of wave functions $\psi_{n\mathbf{k}}(\mathbf{r})$ for a fixed value of $\mathbf{k}$

$$\sum_{\mathbf{G}'} \hat{H}^{\text{KS}}_{\mathbf{G},\mathbf{G}'} c_{n\mathbf{k}}(\mathbf{k}+\mathbf{G}) = \varepsilon_{n\mathbf{k}} c_{n\mathbf{k}}(\mathbf{k}+\mathbf{G})\,, \tag{2.26}$$

where the Kohn-Sham Hamiltonian is

$$\hat{H}^{\mathrm{KS}}_{\mathbf{G},\mathbf{G}'} = -\frac{\hbar^2}{2m_e}|\mathbf{k}+\mathbf{G}'|^2\delta_{\mathbf{G},\mathbf{G}'} + V(\mathbf{G}-\mathbf{G}')\,. \tag{2.27}$$

The procedure implemented in VASP is as follows. First, from the coefficients $c_{n\mathbf{k}}(\mathbf{k}+\mathbf{G})$ the cell periodic part of the wave functions $\psi_{n\mathbf{k}}(\mathbf{r})$ in equation (2.23) is calculated. Then the multiplication of $V(\mathbf{r})\mathrm{u}_{n\mathbf{k}}(\mathbf{r})$ is performed in real space. Finally, the result is transformed into reciprocal space. This is done by implementing the fast fourier transform (FFT) [13] for any periodic function, here given for the three dimensional case

$$f_{k_1,k_2,k_3} = \sum_{n_1,n_2,n_3=0}^{N} c_{n_1,n_2,n_3} e^{-2\pi i \frac{n_1k_1+n_2k_2+n_3k_3}{N}}\,, \tag{2.28}$$

$$c_{n_1,n_2,n_3} = \frac{1}{N^3}\sum_{k_1,k_2,k_3=0}^{N} f_{k_1,k_2,k_3} e^{2\pi i \frac{n_1k_1+n_2k_2+n_3k_3}{N}} \tag{2.29}$$

to transform results between real and reciprocal space.

k-point sampling describes the method of replacing the integral with a weighted sum

$$\frac{1}{\Omega_{\mathrm{BZ}}}\int_{\Omega_{\mathrm{BZ}}} \rightarrow \sum_{\mathbf{k}_i} \omega_{\mathbf{k}_i} \tag{2.30}$$

at certain **k**-points. By including symmetries of the first Brillouin zone the number of required $\mathbf{k}_i$ is reduced further. In addition to **k**-point sampling so called smearing methods with partial occupancies f are applied to speed up convergence, in which the discontinuous Heaviside step function Θ is replaced by a smooth function. Commonly used is the *Gaussian method* [13]

$$f(\varepsilon_{n\mathbf{k}}) = 2\Theta(\varepsilon_F - \varepsilon_{n\mathbf{k}}) \rightarrow f_s^{\mathrm{G}}(\varepsilon_{n\mathbf{k}}) = 1 - \mathrm{erf}(\frac{\varepsilon_{n\mathbf{k}}-\varepsilon_F}{\sigma})\,. \tag{2.31}$$

It contains the smearing parameter σ as a variable of the Gaussian error function. A generalized free energy $F(\sigma) = E(\sigma) - \sigma S(\sigma)$ is minimized instead of the energy E and then the energy is extrapolated to $\sigma \rightarrow 0$ with

$$E_{\sigma\rightarrow 0} = \frac{F(\sigma)+E(\sigma)}{2}\,. \tag{2.32}$$

Another smearing method used in VASP is the Methfessel-Paxton scheme [14]. This further development of the Gaussian method expands the smooth function $f_s(\varepsilon_{n\mathbf{k}})$ into Hermite polynomials. Usually one correction term is sufficient. In this work, most calculations with VASP are performed with the linear tetrahedron method with Blöchl corrections [15]. This algorithm interpolates the energy eigenstates between values at selected **k**-points. Its greatest drawback is that the forces acting on ions cannot be accurately calculated, which makes this method unsuitable for relaxation runs with VASP.

As the properties of solids are mostly determined through their valence electrons, which participate in bonding, the *projector augmented-wave (PAW) method* [16,17] is applied for construction of the wave functions. It is a full potential all-electron method and retains

the nodal structure inside the augmentation spheres. The softer a potential, the less plane waves it applies to construct the wave functions. This causes calculation time to decrease, but might deteriorate the results. The PAW method gives a Hamiltonian $\mathbf{H}^{\mathrm{PAW}}$ for the Kohn-Sham equations. The energy eigenvalues are obtained by solving the system of equations

$$\mathbf{H}^{\mathrm{PAW}}|\tilde{\psi}_n\rangle = \varepsilon_n \mathbf{S}|\tilde{\psi}_n\rangle\,, \tag{2.33}$$

where $\tilde{\psi}_n$ are the pseudo wave functions of the method. The overlap matrix $\mathbf{S}$ can be constructed from the condition that the all-electron wave functions $|\psi_n\rangle$ are orthogonal to one another.

In reciprocal space this problem presents itself as

$$\sum_{\mathbf{G}'} \hat{H}_{\mathbf{G},\mathbf{G}'} c_{n\mathbf{k}}(\mathbf{G}') = \varepsilon_{n\mathbf{k}} \sum_{\mathbf{G}'} \hat{S}_{\mathbf{G},\mathbf{G}'} c_{n\mathbf{k}}(\mathbf{G}') \tag{2.34}$$

for Bloch vector $\mathbf{k}$. Equivalent to minimizing the energy E of the system is to solve this eigenvalue problem numerically by diagonalization of the Hamiltonian matrix, but direct diagonalization schemes have a high computational cost. A more effective way are iterative schemes based on the variational principle. The lowest eigenvalue is obtained by variation of

$$\hat{\varepsilon}(\mathbf{c}) = \frac{\langle\psi|\mathbf{H}|\psi\rangle}{\langle\psi|\mathbf{S}|\psi\rangle} = \frac{\mathbf{c}^\dagger\hat{\mathbf{H}}\mathbf{c}}{\mathbf{c}^\dagger\hat{\mathbf{S}}\mathbf{c}}\,, \tag{2.35}$$

where $\hat{\mathbf{H}}$ and $\hat{\mathbf{S}}$ are matrices with respect to lattice periodic plane waves and $\mathbf{c}$ is the vector of expansion coefficients of the wave function ψ. The global minimum of the energy $\hat{\varepsilon}(\mathbf{c})$ is obtained if ψ is eigenvector with the lowest eigenvalue. For normalized wave functions this leads to the gradient vector or residual vector $\mathbf{g}$

$$\mathbf{g}(\mathbf{c}) = (\hat{\mathbf{H}} - \mathbf{c}^\dagger\hat{\mathbf{H}}\mathbf{c})\mathbf{c} = (\hat{\mathbf{H}} - \hat{\varepsilon})\mathbf{c}\,. \tag{2.36}$$

Thus the residual vector $\mathbf{g}$ requires minimization. Among the methods available to VASP are *steepest descent*, *conjugate gradient*, and *jacobi relaxation* [13]. Higher eigenstates can be obtained by keeping the orbital orthogonal to previously calculated states.

In VASP it is possible to perform ionic relaxations, which is a minimization of the total energy with respect to the ionic configuration. The negative derivative of the total energy with respect to ion I, if the electronic configuration describes the ground state and the wave functions are normalized, is exactly the force $\mathbf{f}_I$ acting on ion I

$$\mathbf{f}_I = -\frac{dE}{d\mathbf{R}_I} = -\frac{\partial E}{\partial \mathbf{R}_I}\,. \tag{2.37}$$

The practical approach to relaxation is to start with an ionic configuration, from which the electronic ground state and forces on separate ions I are calculated. Then the new ionic configuration is determined with a minimization algorithm, such as the conjugate gradient method. For this new ionic configuration the electronic ground state and forces are determined and the procedure repeated until the total energy is well-converged. A possible source of errors in the calculation is that the electronic ground state is obtained iteratively, and thus approximatively, thus convergence of the total energy is important. Another factor is the dependency of basis vectors on ionic coordinates. In plane wave

basis codes this applies only if the basis vectors of the super cell and with them the size of the Brillouin zone are changed. With constant cut-off energy E_{cut} the number of plane waves used in the expansion vary. In the PAW method the augmentation regions depend on the ionic positions and the forces acting on an ion result in additional terms, see reference [17] for details. Small super cells are treated with PAW projectors in reciprocal space, whereas large cells with many atoms are calculated in real space. The former is more exact but requires more computational time than the latter. Another way VASP handles different super cells is that in the relaxation quasi-Newton schemes are applied for small cells, such as RMM-DIIS [18]. For large cells damped molecular dynamics are conducted, which are implemented through a velocity Verlet algorithm or Störmer algorithm [13]. Ionic relaxation schemes, unlike electronic relaxations, can lead to different configurations with local total energy minima. To search for other minima outside the region of phase space sampled by ionic relaxation *simulated annealing* [13] is applied. In this method intermediate configurations with higher energy than the ground state can be overcome to reach a global minimum.

2.6 Computational details

The following settings are applied in VASP throughout this work. The crystalline and amorphous phases of silicon nitride are calculated without considering spin orientations. **k**-point sampling is conducted with the Monkhorst-Pack scheme [19], which applies an equidistant mesh of **k** -points. For the occupancy of the energy eigenvalues the 1^{st} order method of Methfessel-Paxton [14] as well as the linear tetrahedron method with Blöchl corrections [15] are applied. The wave functions are constructed with the PAW method [16]. The exchange-correlation energy functional per electron and its gradient are parametrized with the Perdew-Burke-Ernzerhof (PBE) scheme [20] in the generalized gradient approximation (GGA). The calculations in the following chapters are performed on the phases of silicon nitride for three distinct pairs of plane wave potentials. Specifically, three different combinations of silicon and nitrogen potentials are applied by file concatenation.

The valence electrons of nitrogen are highly localized in real space. Therefore they span a wide range in reciprocal space, making high cut-off energies E_{cut} necessary. Silicon shows hybrid orbitals of covalent character that require only low cut-off energies, but in combination with nitrogen higher E_{cut} are used. The first VASP potential file, POTCAR.SiN, with a cut-off energy of 520 eV (for variable cell volume calculations) or 400 eV (for fixed cell volume) permits the construction of a plane waves basis set with 250 plane waves per atom. The softer potential file, POTCAR.$\mathrm{Si_sN_{vs}}$, needs a cut-off energy of 260 eV (variable volume) or 200 eV (fixed volume). The softest used potential, POTCAR.$\mathrm{Si_{vs}N_{es}}$, requires a cut-off energy of 210 eV (variable volume) or 160 eV (fixed volume) for 32 plane waves per atom.

Chapter 3

Fundamental properties of crystalline silicon nitride

Three crystalline phases of silicon nitride, α-, β- and γ-Si_3N_4, exist. Two phases of crystalline silicon nitride occur naturally, namely the α- and β-phase. Additionally a high pressure γ-phase exists. Transformations of α to β [21] as well as γ to β [22] can be observed.

The calculations in this chapter are conducted with the hard PAW PBE potential. It leads to roughly 250 plane waves per atom at a plane wave cut-off of 520 eV. The structural, electronic, optical and vibrational properties of the crystalline phases of silicon nitride are examined. Optimization of the structure is carried out at a set of volumes. At each volume all parameters, specifically the lattice constants as well as the atomic positions, are optimized. The values are fitted with the non-linear Birch-Murnaghan equation of state to obtain the ground state energy and bulk modulus. The transition pressures from α- to γ-Si_3N_4 and from β- to γ-Si_3N_4 are then calculated. Elastic constants are calculated separately. Band structure and density of states are determined as well. The optical properties are characterized by determination of the dielectric tensor. An examination of zone center phonons is carried out.

3.1 Convergence tests

As discussed in chapter 2.5 the cut-off energy E_{cut} as well as the **k**-point mesh affect the absolute and relative convergence of the calculation significantly. Therefore it is important to establish the most suitable settings. The cut-off energy is set to $E_{\text{cut}} = 520$ eV. For the insulator silicon nitride the **k**-point mesh is optimized, to allow for further efficient calculations.

	α-Si_3N_4 [a]	β-Si_3N_4 [b]	γ-Si_3N_4 [c]
a (Å)	7.7545	7.608	7.7339
c (Å)	5.6215	2.911	
$\frac{c}{a}$	0.7249	0.383	
V (Å^3)	73.186	72.960	57.824
k-point mesh	$4 \times 4 \times 4$	$4 \times 4 \times 8$	$6 \times 6 \times 6$

[a] High-resolution synchrotron powder diffraction data from ref. [23].
[b] X-ray diffraction data from ref. [24].
[c] Synchrotron powder diffraction data for a from ref. [25].

Table 3.1: Optimized **k**-point mesh and unit cell parameters of crystalline silicon nitride phases.

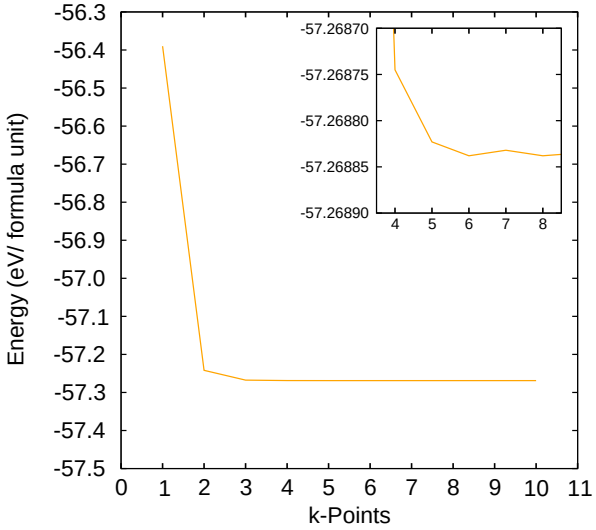

Figure 3.1: **k**-Point optimization for alpha phase of crystalline silicon nitride. The inset shows a close-up when results are converged.

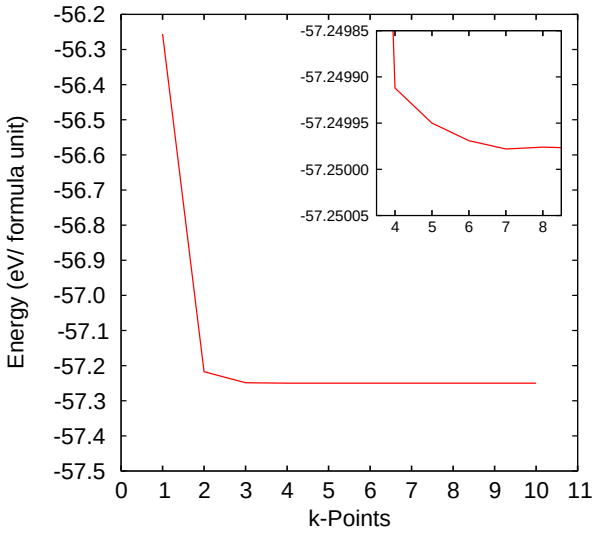

Figure 3.2: **k**-Point optimization for beta phase of crystalline silicon nitride. The inset shows a close-up when results are converged.

Initial calculations for each **k**-point mesh are carried out at the experimental volume with a Gaussian smearing of 0.1 eV. The volumes V per formula unit of α-, β- and γ-Si_3N_4 are calculated from the respective experimental references of the lattice constants a and c. Table 3.1 shows all used unit cell parameters. Specifically, the lattice constants a and c of α-Si_3N_4 are given in reference [23]. Experimental results for a and c of β-silicon nitride are taken from reference [26], which presents the original results of reference [24]. The cubic γ-phase has only the lattice constant a, which is taken from reference [25]. The ratio c/a determines whether the **k**-point mesh should be chosen symmetric. Alpha and gamma silicon nitride are therefore calculated with a mesh of $k \times k \times k$, whereas for the beta phase a $k \times k \times 2k$ mesh is used. In the calculation the structure is allowed to relax

with the quasi-Newton algorithm RMM-DIIS [18] into the ground state by changing cell shape as well as adjusting the atomic positions. The resulting structure is relaxed twice to ensure a sufficiently converged energy. Then the number of **k**-points is increased and the entire procedure repeated.

The figures 3.1, 3.2 and 3.3 show the ground state energy per formula unit in relation to the number of **k**-points for the α-, β- and γ-phase, respectively. The insets present a close-up of the values for four to eight **k**-points, where the calculations reach the required convergence accuracy. As an upper bound a difference in ground state energy between two consecutive calculations of $\Delta E = 10$ μeV per formula unit is reasonable. The calculations for alpha silicon nitride result in convergence for a $4 \times 4 \times 4$ mesh. β-Si_3N_4 converges sufficiently with a $4 \times 4 \times 8$ mesh. The gamma phase should be calculated with a mesh of $6 \times 6 \times 6$.

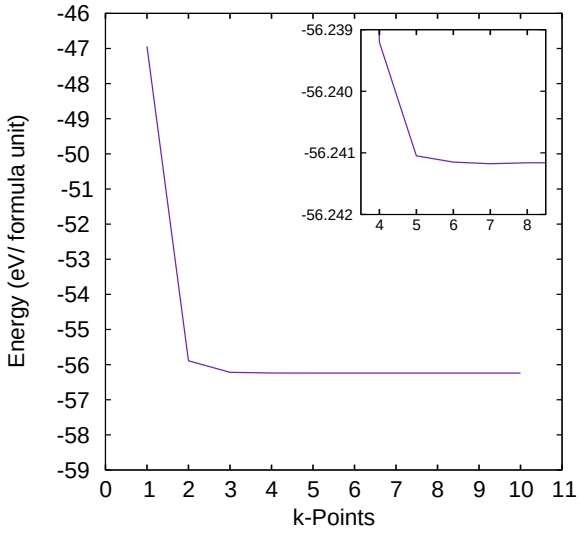

Figure 3.3: **k**-Point optimization for gamma phase of crystalline silicon nitride. The inset shows a close-up when results are converged.

3.2 Structural properties

First the build-up of each unit cell is considered and the correct space group established. Then the ground state energy as well as energy differences between phases are determined. A calculation of the elastic constants and bulk moduli is conducted. Finally the transition pressure between β-Si_3N_4 and γ-Si_3N_4 is determined, as well as between the α- and γ-phase.

3.2.1 Symmetry considerations

The basic building unit of both the α- and β-phase are tetrahedra of SiN_4, with silicon at the center and one nitrogen in each corner. These tetrahedra form a spatial structure by sharing corners in a way that each nitrogen has three silicon neighbors. α- and β-Si_3N_4 can be described in a hexagonal lattice. In the γ-phase, the nitrogen atoms form a roughly face centered cubic (fcc) lattice. This permits SiN_6 octahedra in γ-Si_3N_4, in addition to the SiN_4 tetrahedra that are also present in both other phases. Thus silicon not only lies in the tetrahedral interstices, but also in some of the octahedral sites of the nitrogen lattice. A simplified view of the chemical bonding of neighboring atoms in the crystalline phases of Si_3N_4 is a bonding between sp^3 hybrid orbitals of Si atoms and sp^2 hybrid orbitals of N atoms. One non-bonding p orbital of each nitrogen atom remains with a two electrons.

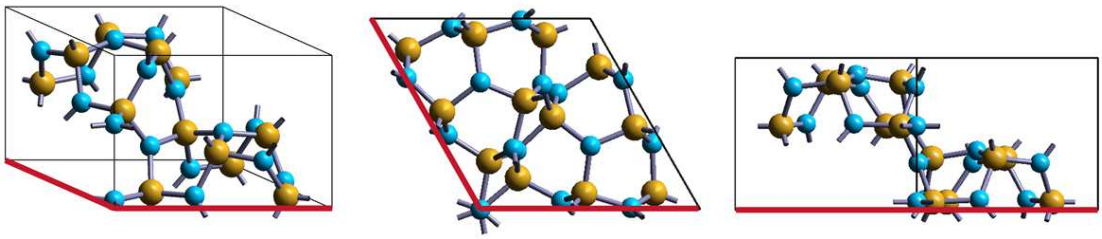

Figure 3.4: α-phase of crystalline silicon nitride. Si atoms are yellow and N atoms are blue.

α-Si_3N_4			atomic positions [a]		
site	Wyckoff	atomic environment	x	y	z
Si1	6c	tetrahedron N_4	0.08194	0.51161	0.65788
Si2	6c	tetrahedron N_4	0.25362	0.16730	0.45090
N1	6c	almost coplanar triangle Si_3	0.65368	0.6100	0.4301
N2	6c	almost coplanar triangle Si_3	0.3159	0.3189	0.6974
N3	2b	coplanar triangle Si_3	1/3	2/3	0.5990
N4	2a	coplanar triangle Si_3	0.0	0.0	0.4502

[a] High-resolution synchrotron powder diffraction data from ref. [23]. Coordinates are given in fractional units.

Table 3.2: Structural data of α-silicon nitride. The space group number is 159, the symbol $P31c$, the Miers crystal class ditrigonal polar, the Lewis crystal class rhombohedral V, and the Schönflies notation C_{3v}^4.

α-Si_3N_4 is of the Miers crystal class ditrigonal polar, in Schönflies notation C_{3v}^4 , and crystallizes in space group $P31c$ [27]. It is a metastable phase of silicon nitride. For historical reasons it was labelled as α-phase, even though the stable modification is β-Si_3N_4. The unit cell of α-Si_3N_4, illustrated in figure 3.4, is hexagonal with 28 atoms (four formula units per unit cell) [23, 28]. The unit cell of the α-phase consists of $\dots ABCDABCD \dots$ layers in the direction of the c-axis. AB as well as CD layers show a similar structure as the β-phase, but instead of having the same spatial alignment the CD layers are rotated by 180° with respect to AB layers.
The atomic environment of nitrogen in α-Si_3N_4 are triangles of Si_3. Silicon forms tetrahedra with nitrogen at the cornes. The atoms can be labelled as Si1, Si2, N1, N2, N3 and N4, as shown in table 3.2. Their respective multiplicity is given by the Wyckoff-position. The symmetry operations required for the atomic positions of the duplicates are taken from reference [29]. Si1 and Si2 atoms are in a tetrahedral configuration, fourfold coordinated, and in special positions ($6c$). N1 and N2 atoms are in almost coplanar configuration, threefold coordinated, and also in special positions ($6c$). N3 atoms are in a coplanar configuration, threefold coordinated, in positions ($2b$) and N4 atoms are in a coplanar configuration, threefold coordinated, in special positions ($2a$).

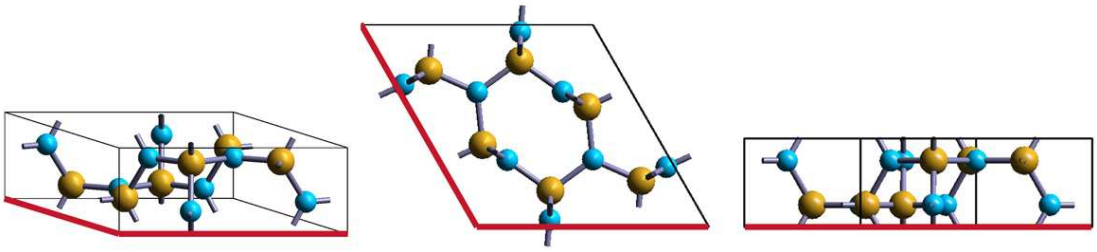

Figure 3.5: β-phase of crystalline silicon nitride. Si atoms are yellow and N atoms are blue.

The unit cell of β-Si_3N_4 is hexagonal with 14 atoms, but there has been ongoing scientific dispute for over 50 years as to the exact symmetry. The earliest classification was to the space group $P6_3m$ [24, 26, 30–35] and therefore to Miers crystal class hexagonal equatorial C_{6h}^2. Then other experiments found that β-Si_3N_4 has only space group $P6_3$ [36, 37], i.e. the mirror plane is lacking, and belongs to class hexagonal polar with Schönflies notation C_6^6. Other groups found that bulk β-Si_3N_4 displays the horizontal symmetry that places its structure within the space group $P6_3m$, whereas thin crystals may show the tendency to form $P6_3$ structure [38]. Recent experimental findings [39], as well as results from *ab-initio* calculations [40, 41], suggest that this is indeed the correct description of this structure.

To correctly establish which space group of β-Si_3N_4 is thermodynamically more stable two separate VASP calculations are performed with relaxation, one starting from the structure with space group $P6_3$ and the other with $P6_3m$. Selective dynamics are applied to fix the position of the silicon atom Si1 at $z = 0.25$. Thus the atomic positions between the two possible β-phases can easily be compared. After the calculation the structure has relaxed $P6_3$ to $P6_3m$ symmetry, as shown in the rightmost column of table 3.3. This holds regardless of the initial structure, as the nitrogens' z-coordinates of the calculation with the $P6_3m$ symmetry remained at $z = 0.25$ within VASP's precision. The atomic positions that differ in these two symmetry groups have a remaining difference of ≤ 0.0005

site	$\Delta\left((P6_3)_i - (P6_3)_r\right)$ [a] (%)	$\Delta\left((P6_3m)_r - (P6_3)_r\right)$ (%)
Si1	0.0	0.0
N1	1.275	0.005
N2	-1.039	-0.041

[a]Single-crystal x-ray diffraction data for the $P6_3$ structure from ref. [37]. Single crystal photograph data for the $P6_3m$ structure from ref. [26].

Table 3.3: Differences in z-coordinates of atoms in β-Si_3N_4 from the plane $z = 0.25$, stated in percent of the lattice parameter c. The first column of values describes the difference of the positions between the initial and the relaxed $P6_3$ structure calculated with VASP. The second column gives the difference between the atomic positions of the relaxed $P6_3$ and relaxed $P6_3m$ structure.

in relative coordinates or ≤ 0.05 % of the lattice parameter $c = 2.911$Å. This is negligable. The relaxation of β-Si_3N_4 to $P6_3m$ has also been found by other groups, for example in reference [40]. Therefore, in this work, the atomic positions for β-Si_3N_4 are selected according to the space group $P6_3m$, as depicted in figure 3.5. The sequence of the layers along the c-axis is $\ldots ABAB \ldots$. Half of the atoms are located in the plane $z = \frac{1}{4}c$ and the other half in the plane $z = \frac{3}{4}c$.
β-Si_3N_4 has nitrogen in coplanar and non-coplanar configurations, with one N and three Si atoms each. The atomic environment of silicon are again tetrahedra of SiN_4. Table 3.4 contains the atoms labelled as Si1, N1 and N2 as well as their respective multiplicity. The symmetry operations are taken from reference [42]. Si1 atoms are in a distorted tetrahedral configuration, fourfold coordinated, and in special positions ($6h$). N1 atoms are in a non-coplanar configuration, threefold coordinated, in special positions ($6h$), wheras N2 atoms are in a coplanar configuration, threefold coordinated, in fixed positions ($2c$) at $(\frac{1}{3},\ \frac{2}{3},\ \frac{1}{4})$ and $(\frac{2}{3},\ \frac{1}{3},\ \frac{3}{4})$.

β-Si_3N_4			atomic positions [a]		
site	Wyckoff	atomic environment	x	y	z
Si1	$6h$	tetrahedron N_4	0.1733	-0.2306	1/4
N1	$6h$	non-coplanar triangle Si_3	0.3323	0.0314	1/4
N2	$2c$	coplanar triangle Si_3	1/3	2/3	1/4

[a]Single crystal photograph data from ref. [26] . Coordinates are given in fractional units.

Table 3.4: Structural data of β-silicon nitride. The space group number is 176, the symbol $P6_3m$, the Miers crystal class hexagonal equatorial, the Lewis crystal class hexagonal II, and the Schönflies notation C^2_{6h}.

γ-Si_3N_4 has the inverse spinel structure and does not occur naturally. It is a high pressure phase used in ceramics applications [2]. γ-Si_3N_4 has space group $Fd\overline{3}m$ [25, 43–45] and falls into the Miers crystal class ditesseral central with Schönflies notation O^7_h . The cubic unit cell consists of 56 atoms, whereas a smaller primitive fcc cell can be constructed from

14 atoms (6 silicon and 8 nitrogen atoms). Figure 3.6 illustrates the γ-phase.
The silicon atoms in γ-Si_3N_4 are either tetrahedrally or octahedrally coordinated, with the nitrogen atoms located in the center of non-coplanar triangles. Table 3.4 contains the atoms labelled as Si1, Si2 and N1. The multiplicity of the atoms needs to be divided by four to obtain the correct number of atoms used in the primitive fcc cell. The symmetry operations are taken from reference [46]. Si1 atoms are in tetrahedral configuration, fourfold coordinated. They make up one third of the unit cell's Si atoms, and are in fixed position ($8a$) at $(0, 0, 0)$. Si2 atoms are in octahedral configuration, sixfold coordinated. These silicon atoms, which make up two thirds of all Si atoms of the unit cell, are in fixed position ($16d$) at $(\frac{5}{8}, \frac{5}{8}, \frac{5}{8})$. N1 atoms are in a non-coplanar configuration, threefold coordinated, and in fixed positions ($32e$) at (x, x, x) where $x = 0.3833$. They form an fcc lattice.

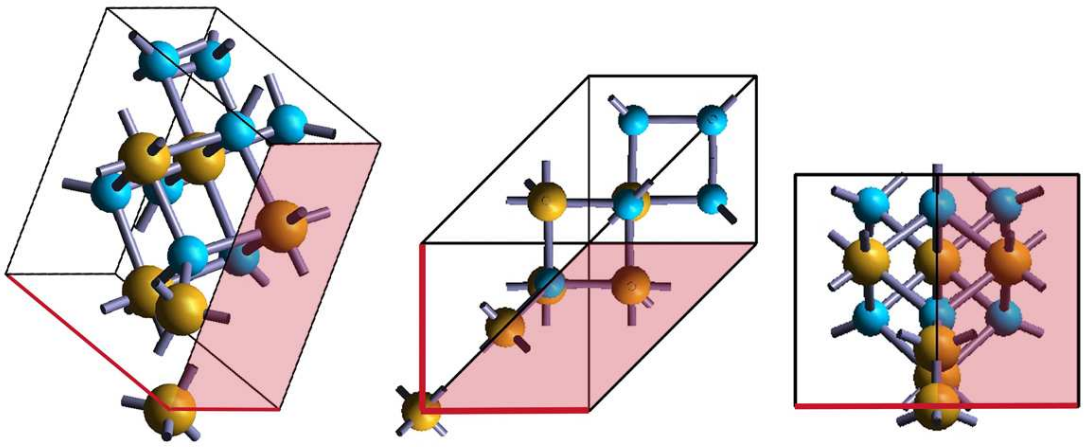

Figure 3.6: γ-phase of crystalline silicon nitride. Si atoms are yellow and N atoms are blue.

γ-Si_3N_4			atomic positions [a]		
site	Wyckoff	atomic environment	x	y	z
Si1	$8a$	tetrahedron N_4	0.0	0.0	0.0
Si2	$16d$	octahedron N_6	5/8	5/8	5/8
N1	$32e$	non-coplanar triangle Si_3	0.3833	0.3833	0.3833

[a] X-ray powder diffraction data from ref. [25]. Coordinates are given in fractional units.

Table 3.5: Structural data of γ-silicon nitride. The space group number is 227, the symbol $Fd\overline{3}m$, the Miers crystal class ditesseral central, the Lewis crystal class cubic II, and the Schönflies notation O_h^7.

3.2.2 Equilibrium volume

The equilibrium volumes as well as the ground state energies of the crystalline silicon nitride phases are obtained by relaxing the cell structure and atomic positions for each volume. Then the energy-volume curve is fitted to the Birch-Murnaghan equation of state (EoS) to extract the minimum. The Birch-Murnaghan equation of state [47] is given as

$$E(V) = E_0 + B_0 V_0 \frac{9}{16}\left[B_0'\left(\left(\frac{V_0}{V}\right)^{\frac{2}{3}} - 1\right)^3 + \left(\left(\frac{V_0}{V}\right)^{\frac{2}{3}} - 1\right)^2\left(6 - 4\left(\frac{V_0}{V}\right)^{\frac{2}{3}}\right)\right], \quad (3.1)$$

where E_0 is the ground state energy, V_0 is the equilibrium volume, B_0 is the bulk modulus and B_0' is the first derivative of the bulk modulus.

	α-Si_3N_4			β-Si_3N_4			γ-Si_3N_4		
property	exp. [a]	sim. [b]	present work	exp. [c]	sim. [d]	present work	exp. [e]	sim. [f]	present work
a_0 (Å)	7.755	7.808	7.8083	7.608	7.667	7.6612	7.734	7.789	7.7839
c_0 (Å)	5.622	5.660	5.6590	2.911	2.928	2.9246			
$\frac{c}{a}$	0.725	0.725	0.7247	0.383	0.382	0.3817			
V_0 (Å^3)	73.19	74.71	74.70	72.96	74.53	74.33	57.82	59.07	58.96
E_0 (eV)			-57.267			-57.269			-56.218
ΔE (meV)			1.4			0.0			1050.2

[a] High-resolution synchrotron powder diffraction data from reference [23].
[b] *Ab-initio* data from reference [48]. VASP calculations with the Perdew-Zunger parametrization of the Ceperly-Alder functional within local density approximation (LDA) are performed. The wave functions are constructed with the PAW method.
[c] Single crystal photograph data from reference [26].
[d] *Ab-initio* data from reference [49]. VASP calculations with the Perdew-Wang parametrization of the exchange-correlation energy functional within GGA as well as some calculations with the Ceperly-Alder functional within LDA are performed. The wave functions are constructed with the PAW method.
[e] X-ray powder diffraction data from reference [25].
[f] *Ab-initio* data from reference [50]. VASP calculations within GGA as well as LDA are performed. The exchange-correlation energy functionals are not stated. The wave functions are constructed with the PAW method.

Table 3.6: Lattice constants a_0 and c_0 as well as ratio c/a of unit cells after relaxation. Equilibrium volume V_0 and ground state energy E_0, both per formula unit, of the crystalline silicon nitride phases. The difference in ground state energy to the stable phase β-Si_3N_4 is given in meV.

The atomic positions for all three POSCAR files are constructed from experimental values in combination with space group considerations, and are listed in tables 3.2, 3.4 and 3.5. The applied script first calculates the minimal energy at a given volume with a relaxation of both cell shape and atomic positions for a Γ-centered **k**-point mesh. Γ-centered meshes are centered around the origin $(0, 0, 0)$. The relaxation is controlled using the tag ISIF=4 in file INCAR. This relaxes all internal degrees of freedom (DoF) except the volume. IBRION=2 selects the conjugated gradient algorithm as relaxation method [13]. Initially this mesh

contains $1 \times 1 \times 1$ **k**-points. For β-Si_3N_4 a mesh of $k \times k \times 2k$ is applied instead, due to the smaller ratio c_0/a_0. The first relaxation therefore uses a $1 \times 1 \times 2$ mesh. After this first relaxation the output file of the cell dimension and atomic positions, the file CONTCAR, is renamed to POSCAR to be used as input file for another calculation with identical relaxation parameters. This procedure is repeated a second time to further optimize the positions. Then the script continues with a new calculation of the minimal energy for the next larger cell volume using the optimized CONTCAR file from the previous volume. After the entire set of curves has been calculated in this manner, the number of **k**-points are manually increased by 1 in each direction and the calculation is then started again. To speed up the calculation, the CONTCAR files with **k**-point mesh $1 \times 1 \times 1$ from the respective volumes are used here. This procedure is carried out for α-Si_3N_4 up to a mesh of $4 \times 4 \times 4$ **k**-points, for β-Si_3N_4 to $4 \times 4 \times 8$ ($k \times k \times 2k$), and up to $6 \times 6 \times 6$ for γ-Si_3N_4. Table 3.6 lists the calculated lattice constants a_0 and c_0, the ratio c/a, the cell volume per formula unit of the silicon nitride phases as well as their ground state energy per formula unit and the relative energy difference between the phases. The ground state energy is derived from the parameter E_0 in equation (3.1), whereas the cell volume is given by V_0. To obtain E_0 and V_0 per formula unit (Si_3N_4), the calculated total ground state energy and cell volume are divided by 4, 2 and 2 for α-, β- and γ-silicon nitride, respectively.

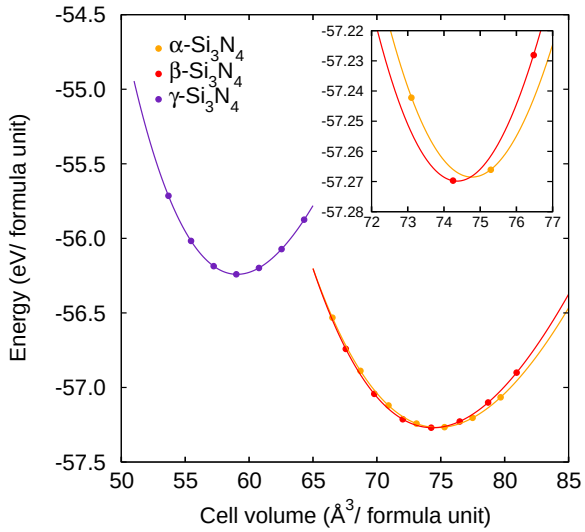

Figure 3.7: Equations of state of crystalline silicon nitride for all three phases. The EoS of the α-phase is orange, of the β-phase red and of the γ-phase indigo.

The lattice constants of α-Si_3N_4 are determined as $a_0 = 7.8083$ Å and $c_0 = 5.6590$ Å. The β-phase is built up from a unit cell with $a_0 = 7.6612$ Å and $c_0 = 2.9246$ Å, and the lattice constant of the cubic γ-phase is $a_0 = 7.7839$ Å. The lattice constants of all three crystalline silicon nitride phases are in good agreement with experimental results [23, 25, 26], as shown in table 3.6. The VASP calculations tend to overestimate the lattice constants, but only in the order of a few picometers. Previous VASP calculations conducted by other groups [48–50] report slightly higher results for the lattice constants a_0 and c_0. The ratios c/a for α-Si_3N_4 and β-Si_3N_4 are obtained as 0.7247 and 0.3817, respectively. The equilibrium volume of α-Si_3N_4 is $V_0 = 74.70$ Å^3. The result for the β-phase is $V_0 = 74.33$ Å^3, and γ-Si_3N_4 has an equilibrium volume of $V_0 = 58.96$ Å^3. The equilibrium volumes of the three crystalline silicon nitride phases are each in accordance

with the referenced experiments and ab-initio calculations. The volume of β-Si_3N_4 is slightly less than that of α-Si_3N_4. The high pressure γ-phase has the smallest equilibrium volume.

The α- and β-phase have a very similar energy at the minimum. The energy difference between these two naturally occuring phases is below 20 meV per formula unit. γ-Si_3N_4 on the other hand can easily be differentiated from the other two phases due to its higher ground state energy. The ground state energy difference between α- and γ-phase or β- and γ-phase is $\approx$ 1.0 eV per fomula unit. The chart in figure 3.7 shows the values that are calculated for the three phases including the respective fits. In the inset the fits of the α- and β-phase around the minimum are displayed. It can be easily seen that the β-phase has the lowest ground state energy of the three crystalline silicon nitride phases. This low ground state energy indicates unambiguously that β-Si_3N_4 is the thermodynamically stable phase.

3.2.3 Elastic constants and bulk modulus

Classical elastic theory [12] gives the potential energy of the harmonic crystal as

$$U^{\text{harm}} = \frac{1}{2}\sum_{\sigma\tau\mu\nu}\int d\mathbf{r}(\frac{\partial}{\partial x_\sigma}u_\mu(\mathbf{r}))(\frac{\partial}{\partial x_\tau}u_\nu(\mathbf{r}))\bar{E}_{\sigma\mu\tau\nu}\,, \tag{3.2}$$

where $\mathbf{u}(\mathbf{r})$ is a continuous displacement field. With the volume v of the primitive cell the elastic tensor $E_{\sigma\mu\tau\nu} = v\bar{E}_{\sigma\mu\tau\nu}$ is obtained. From the elastic tensor $E_{\sigma\mu\tau\nu}$ of the fourth rank describing all possible displacements of a harmonic crystal the strain tensor $\varepsilon_{\sigma\mu}$ can be derived. The strain tensor $\varepsilon_{\sigma\mu}$ is commonly described by the stain components $e_{\mu\nu}$, which are simplified to e_α using the Voigt notation

$$xx \to 1, \quad yy \to 2, \quad zz \to 3, \quad yz \to 4, \quad zx \to 5, \quad xy \to 6\,. \tag{3.3}$$

The potential energy of the crystal is thus given as

$$U = \frac{1}{2}\sum_{\alpha\beta}\int d\boldsymbol{r}e_\alpha C_{\alpha\beta}e_\beta\,. \tag{3.4}$$

The number of independent elastic constants $C_{\alpha\beta}$ varies for different crystal classes. Reference [51] states that crystals of class C_{3v} have six, crystals of class C_{6h} have five, and cubic systems, such as class O_h, have only three independent elastic constants. Specificially, the elastic constants C_{11}, C_{12} C_{13}, C_{15}, C_{33} and C_{44} are independent for α-Si_3N_4. For β-silicon nitride the constants C_{11}, C_{12}, C_{13}, C_{33} and C_{44} are independent and for the γ-phase the elastic constants C_{11}, C_{12} and C_{44} are independent.

Apart from the elastic constants the bulk modulus B_0 is calculated from the equation of state. The bulk modulus B_0 corresponds to the mean tension or pressure as type of stress [51]. Mean tension or pressure on a solid results in cubical dilatation as strain type. The bulk modulus B_0 is also known as modulus of compression and given by

$$B_0 = \frac{1}{K} = -V\frac{\partial P}{\partial V}, \tag{3.5}$$

where K is the compressibility, V is the volume and P is the pressure.

A special VASP simulation is carried out to determine the elastic constants, in which finite distortions of the lattice are applied. The used settings in the INCAR file are IBRION=6 and ISIF=3. For calculation of the bulk modulus an optimization of the structure is carried out at a set of volumes. At each volume all parameters, specifically the lattice constants as well as the atomic positions, are optimized. The corresponding tag in the INCAR file is ISIF=4. This procedure is detailed in chapter 3.2.2. The values are fitted with the non-linear Birch-Murnaghan equation of state (3.1) to obtain the bulk modulus B_0 and the results are given in table 3.7.

	α-Si_3N_4		β-Si_3N_4		γ-Si_3N_4	
property (GPa)	ref. [a]	present work	ref. [b]	present work	ref. [c]	present work
bulk modulus B_0	256	220	273	234	300	292
ΔB_0 (%)		14.1		14.3		2.7
C_{11}	526	399.7	409.3	413.3	499.6	514.2
C_{12}	128	136.3	271.2	198.4	191.0	182.7
C_{13}	106	119.1	200.6	115.6		
C_{15}		13.5				
C_{33}	574	435.1	603.6	544.0		
C_{44}		124.9	108.0	98.8	349.4	327.0

[a] X-ray diffraction data for bulk modulus and *ab-initio* data for elastic constants from reference [23]. C_{15} and C_{44} are not stated. The *ab-initio* data is obtained from VASP calculations with the PBE parametrization of the exchange-correlation energy functional within GGA. The wave functions are constructed with the PAW method.

[b] X-ray diffraction data for bulk modulus from reference [52]. *Ab-initio* data for elastic constants from reference [53], which is obtained from an orthogonalized linear combination of atomic orbitals (OLCAO) approach based on DFT/LDA.

[c] Raman spectroscopy, TEM and EDX data for bulk modulus from reference [45]. *Ab-initio* data for elastic constants from reference [44]. VASP calculations with the Perdew-91 (PW91) parametrization of the exchange-correlation energy functional within GGA as well as with the Ceperly-Alder functional within LDA are performed. The wave functions are constructed with the Vanderbilt ultrasoft pseudopotential (US-PP) method.

Table 3.7: Calculated bulk moduli B_0 and elastic constants of crystalline silicon nitride phases. ΔB_0 denotes the deviation of the present results to experimental reference values in percent.

The elastic constants C_{11} and C_{33} of α-Si_3N_4 are lower than the reference values. The elastic constant C_{11} is only marginally lower than C_{33}, as in the literature. The difference of $\approx$ 9 % implies a fairly isotropic behaviour. The elastic constants C_{12} and C_{13} are slightly higher when compared to literature, by $\approx$ 10 % and have almost the same values. This implies only minimal anisotropy in response to shear stresses. Reference [23] does not state values for C_{15} and C_{44}. In reference [53] the elastic constant C_{44} is given as 119-132 GPa, in excellent agreement with the present result. The calculated elastic constants of β-Si_3N_4 are lower than the reference values, except for C_{11}. C_{11} is only higher by $\leq$ 1 % and can be regarded as being in very good agreement. C_{12}

and C_{13} are much lower, whereas C_{33} and C_{44} are lower by $\approx$ 10 %. The significant difference between the elastic constants C_{11} and C_{33} of β-Si_3N_4 points to a higher elastic anisotropy of the β-phase compared to α-Si_3N_4. The elastic constant C_{11} of γ-Si_3N_4 is slightly higher, by $\leq$ 3 %, than the reference value. C_{12} is lower by $\approx$ 6 % and C_{44} is also lower than in the literature. The degree of Cauchy violation $C_{44}/C_{12} \neq 1$, as suggested in reference [44], is found to be $C_{44}/C_{12} = 1.79$ and thus indicates covalent bonding.

All calculated bulk moduli are lower than the reference values. The greatest deviation, 14.3 %, of B_0 to reported results is for β-Si_3N_4, as shown in table 3.7. The underestimation of the bulk modulus in α-Si_3N_4 is very similar. The results for the bulk modulus in γ-Si_3N_4 show a very good agreement with the reference value.

3.2.4 Transition pressure

A solid with a certain configuration can transform into a different phase of the same material. Thermodynamically this corresponds to a transition pressure which must be overcome. From the ground state energy E_0 and volume V_0

$$E = H - pV \ , \ -\frac{\partial E}{\partial V} = p \tag{3.6}$$

the transition pressure p_t is obtained by constructing a common tangent between the two phases in question. This can be either performed geometrically or analytically. Here the transitions of Si_3N_4 from the stable β-phase to the high pressure γ-phase as well as from the metastable α- to the γ-phase are discussed. The values for E_0 and V_0 are taken from table 3.6. The slopes of the tangents yield the transition pressures $p_t^{\beta\to\gamma}$ and $p_t^{\alpha\to\gamma}$, respectively, as shown in table 3.8.

transition pressure (GPa)	ref. [a]	present work
$p_t^{\beta\to\gamma}$	13.0	11.0
$p_t^{\alpha\to\gamma}$		10.7

[a] Raman spectroscopy, TEM and EDX data for β-γ transition pressure from reference [45].

Table 3.8: Transition pressures of crystalline silicon nitride phases for the transition from stable β-Si_3N_4 to γ-Si_3N_4 as well as from the metastable α- to the γ-phase.

As the α- and β-phase show similar E_0 and V_0 the corresponding transition pressures $p_t^{\alpha\to\gamma}$ and $p_t^{\beta\to\gamma}$ are also close to each other. The transition pressure $p_t^{\beta\to\gamma}$ of β-Si_3N_4 to γ-Si_3N_4 is in good agreement with experiments. Compared to the experimental results of reference [45], the calculation with VASP underestimates the transition pressure of β to γ-phase. This is most likely a DFT/PBE error, as the method is known to overestimate the equilibrium volume, which in turn may cause the calculated transition pressure to decrease. The deviation from experimental findings is within 16% for the transition of β-Si_3N_4 to γ-Si_3N_4.

3.3 Electronic properties

The following electronic properties of the crystalline silicon nitride phases are calculated. First a calculation of the density of states and band structure is performed. Then the local density of states are interpreted.

3.3.1 Density of states and band structure

The insulator silicon nitride forms crystals with predominantly covalent character and due to the presence of nitrogen, an element from group III, the bonds are slightly ionic. Hybrid orbitals between Si and N are formed, which differ considerably from the original atomic orbitals. More specifically, the energy levels of the valence electrons in the presence of the ion cores' periodic potential need to be taken into account, as discussed in chapter 2.4. As a result, the electron levels form bands and forbidden zones in between. The forbidden zone between occupied and unoccupied energy levels, within DFT, is called the Kohn-Sham one electron energy gap (KS band gap)

$$E_g = \varepsilon_c - \varepsilon_v \,. \tag{3.7}$$

It is obtained from the energy difference between the conduction band (CB) minima ε_c, the lowest unoccupied crystal orbital (LUCO), and the valence band (VB) maxima ε_v, the highest occupied crystal orbital (HOCO). The band gap can be crossed by valence electrons through either direct or indirect interband transitions, if sufficient energy in form of temperature or photonic excitation is supplied. When a photon with energy $\hbar\omega$ and momentum $\hbar\mathbf{q}$ is absorbed in the crystal lattice, a crystal momentum conservation law applies to the possible change in the electron wave vector $\mathbf{k}'$ because of the translational symmetry of the nuclei's periodic potential. It is given by

$$\mathbf{k}' = \mathbf{k} + \mathbf{q} + \mathbf{G} \,, \tag{3.8}$$

where $\mathbf{G}$ describes a shift by a vector of the reciprocal lattice and $\mathbf{q}$ is a wave vector of the absorbed or emitted photon. A comparison of energies leads to the conclusion that the wave vector of a Bloch electron is essentially unchanged when it absorbs a photon at typical optical energies in the range $150 - 400$ nm [12]. The change of the electron energy by $\hbar\omega$ of the order of a few eV by transition from one electronic band to another, without significant change in wave vector, is the direct interband transition, where the frequency of the optical threshold is $\omega = E_g/\hbar$. In indirect interband transitions the electron wave vector $\mathbf{k}$ is not conserved and a phonon is created. Here the optical threshold occurs at $E_g/\hbar - \omega(\mathbf{q})$ because the necessary phonon with crystal momentum $\hbar\mathbf{q}$ additionally supplies an energy $\hbar\omega(\mathbf{q})$, effectively lowering the KS gap. This effect is in general around $10 - 200$ meV and thus only important in materials with small band gaps. If the interband transitions within a material result in an observable conductivity below the melting point, the material is a semiconductor. Crystalline silicon nitride has a fairly wide KS gap, comparable to diamond, with only photons in the UV range containing enough energy to bridge the band gap, thus it is considered an insulator.

First a self consistent structural relaxation is performed with VASP by using the tag ISMEAR=-5 in INCAR file for the tetrahedron method with Blöchl corrections [15]. The number of grid points in the density of states (DoS) calculation is set to NEDOS=2001.

	α-Si_3N_4, β-Si_3N_4			γ-Si_3N_4		
symmetry point	x	y	z	x	y	z
Γ	0.0	0.0	0.0	0.0	0.0	0.0
A	0.0	0.0	0.5			
H	-0.333	0.667	0.5			
K	-0.333	0.667	0.0	0.375	0.75	0.375
L	0.0	0.5	0.5	0.5	0.5	0.5
M	0.0	0.5	0.0			
W				0.25	0.5	0.75
X				0.0	0.5	0.5

Table 3.9: Symmetry points of the three crystalline polymorphs of silicon nitride. The positions of the symmetry points are given in fractional coordinates, in terms of the reciprocal lattice of the primitive cell.

The tag IBRION=1 selects the quasi-Newton algorithm RMM-DIIS [18], and with ISIF=3 all internal degrees of freedom are relaxed. Then the optimization of DoS and band structure is carried out along a designated path in **k**-space with the Gaussian smearing method ISMEAR=0 and SIGMA=0.1 at the equilibrium volume V_0. Again the tag NEDOS=2001 is used to specify the number of grid points in the DoS. Some empty bands are included in the optimization run with the tag NBANDS set to a larger value than the number of valence electrons in the unit cell. In this second VASP run the charge density from the self consistent calculation is applied. This is achieved by setting the tag ICHARG=11, which reads in the file CHGCAR from the previous run and then keeps the charge density constant during the electronic minimization. Therefore energy eigenvalues and DoS for each **k**-point are obtained independently. The energy eigenvalues are used for band structure plots. The sampling path in **k**-space for α- and β-Si_3N_4 is selected as $\Gamma - K - H - A - \Gamma - M - L - A$ and for γ-Si_3N_4 as $\Gamma - K - X - \Gamma - L - X - W - L$. The positions of these specific points is given in table 3.9. The number of bands in α-Si_3N_4 is twice as large as in β-Si_3N_4 or γ-Si_3N_4, because the unit cell of the α-phase contains four formula units instead of two. The results obtained for the band structure and density of states of the three crystalline polymorphs of Si_3N_4 are shown in figures 3.8, 3.9 and 3.10 and summed up in table 3.10. They are in overall excellent agreement with experiments and *ab-initio* calculations.

The width of the valence band of α-Si_3N_4 is 18.4 eV using PBE. The lower part of the VB is between -18.4 eV and -14.5 eV. The upper part of α-Si_3N_4's VB starts at -9.7 eV and goes up to 0.0 eV. VASP places the Fermi level ε_F not at mid gap, but close to the top of the VB. The band structure calculations for the α-phase of crystalline silicon nitride indicate that the highest point of the VB is the K-point. The energy difference between K- and M-point however is only 0.2 meV, which can be argued is below the certainty of the method. *Ab-initio* calculations [54] performed by another group have found the M-point to be the maximum of the VB. The conduction band minimum of α-Si_3N_4 is at the Γ-point. Thus the indirect Kohn-Sham PBE band gap E_g of the α-phase is established as 4.7 eV. Compared to the experimental result of the optical threshhold 4.4 eV in reference [55] the KS PBE band gap E_g is overestimated. This overestimation

indicates that the experimental findings may be too low, as DFT underestimates the band gaps always [48]. In crystalline silicon nitride the error is expected to be $1-2$ eV. In comparison to other *ab-initio* results [48, 54], the calculated KS PBE band gap of α-Si_3N_4 is slightly larger, but within a few meV. The direct KS PBE band gap at the Γ-point is calculated as 4.7 eV, which is also in excellent agreement with other *ab-initio* results [54].

	α-Si_3N_4			β-Si_3N_4			γ-Si_3N_4	
property (eV)	exp. [a]	ref. [b]	present work	exp. [c]	ref. [d]	present work	ref. [e,f]	present work
CB min.		Γ	Γ		Γ	Γ	Γ	Γ
VB max.		M	M, K		$\Gamma \to A$	$\Gamma \to A$	$\Gamma \to K$	$\Gamma \to K$
E_g min.	4.4	4.63	4.65	4.6-5.5	4.3	4.25	3.40	3.34
E_g at Γ		4.67	4.71		4.5	4.45	3.45	3.38
bottom 1st VB	-12	-10.15	-9.73		-10.2	-10.14	-10.25	-10.90
top 2nd VB	-16	-14.20	-14.45		-14.0	-14.73	-13.50	-13.72
bottom 2nd VB	-22	-18.36	-18.41		-18.2	-18.52	-18.82	-19.23
width 1st VB	12	10.15	9.73	10-12	10.2	10.14	10.25	10.90
width 2nd VB	6	4.16	3.96	4-5	4.2	3.79	5.32	5.51
full width VB	22	18.36	18.41		18.2	18.52	18.82	19.23

[a] Soft x-ray spectroscopy and photoelectron spectroscopy (PES) data from reference [55].
[b] *Ab-initio* data from reference [54], which is obtained from an OLCAO approach based on DFT/LDA.
[c] Data cited in reference [41], which is obtained from XPS and Bremsstrahlung isochromat spectroscopy (BIS) as well as from photoemission experiments.
[d] *Ab-initio* data from reference [41], which is obtained from a pseudopotential method based on DFT/LDA.
[e] No experimental data on optical threshold or bandwidths known to the author at the time of research, thus the column is omitted.
[f] *Ab-initio* data from reference [56], which is obtained from an OLCAO approach based on DFT/LDA.

Table 3.10: Kohn-Sham PBE band gap E_g of the three crystalline phases of Si_3N_4, minimum as well as direct at the Γ-point. The other *ab-initio* results are DFT band gaps, whereas the experimental values for E_g denote the optical band gaps. The location of the CB minimum, the VB maximum and the bandwidths of the valence bands are also detailed.

The β-phase of crystalline silicon nitride shows a VB with a bandwidth of 18.5 eV. The lower part of the VB of β-Si_3N_4 lies between -18.5 eV and -14.7 eV. The upper VB starts at -10.1 eV and the VB maximum lies partway between the Γ-point and the A-point. The lowest point of the CB is located at the Γ-point. Therefore the minimal KS PBE band gap E_g of β-Si_3N_4 is 4.3 eV, an indirect interband threshold. The direct KS PBE band gap of the β-phase at the Γ-point is 4.5 eV. Both the direct and the indirect Kohn-Sham PBE band gaps of β-Si_3N_4 are within the range of *ab-initio* results reported by other groups, specifically 4.2 eV from reference [48] and 4.3 eV from reference [41]. Experimentally determined optical band gaps, as cited in reference [41], are larger by approximately $0.3-1.2$ eV, which is likely to be attributable to the aforementioned deficiency of density functional theory.

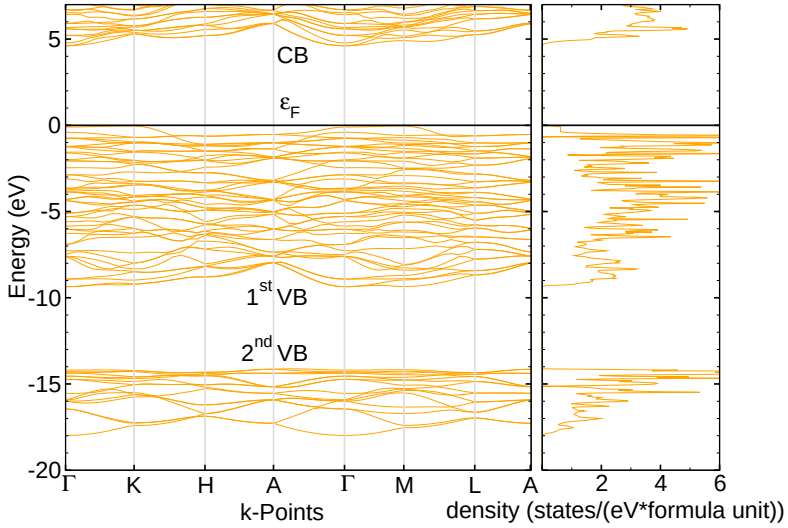

Figure 3.8: Band structure and DoS for α-silicon nitride. The DoS is of the first Brillouin zone, as obtained in chapter 3.3.2.

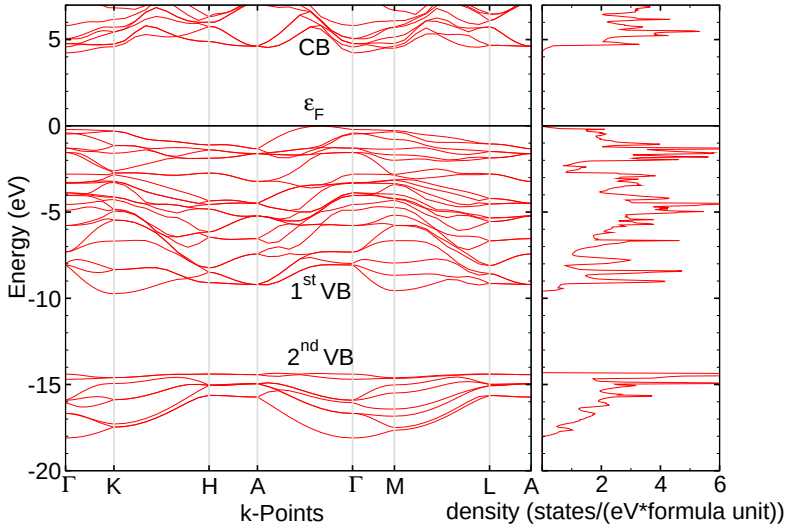

Figure 3.9: Band structure and DoS for β-silicon nitride. The DoS is of the first Brillouin zone, as obtained in chapter 3.3.2.

The width of the valence band of γ-Si_3N_4 is 19.2 eV. The lower part of the valence band is between -19.2 eV and -13.7 eV. The upper VB of γ-Si_3N_4 lies above -10.9 eV. The VB maximum is located between the Γ-point and the K-point. The lowest point of the γ-phase's conduction band is at the Γ-point. Thus the indirect Kohn-Sham PBE band gap E_g of γ-Si_3N_4 is 3.3 eV, slightly smaller than other *ab-initio* calculations [56]. The direct KS PBE band gap of the γ-phase is obtained as 3.4 eV.

The crystalline polymorphs of Si_3N_4 show very similar characteristics in their band structure. The **k**-point sampling path is the same for the α-phase as for β-Si_3N_4, thus the band structure of these two can be especially well compared. Of the valence bandwidths

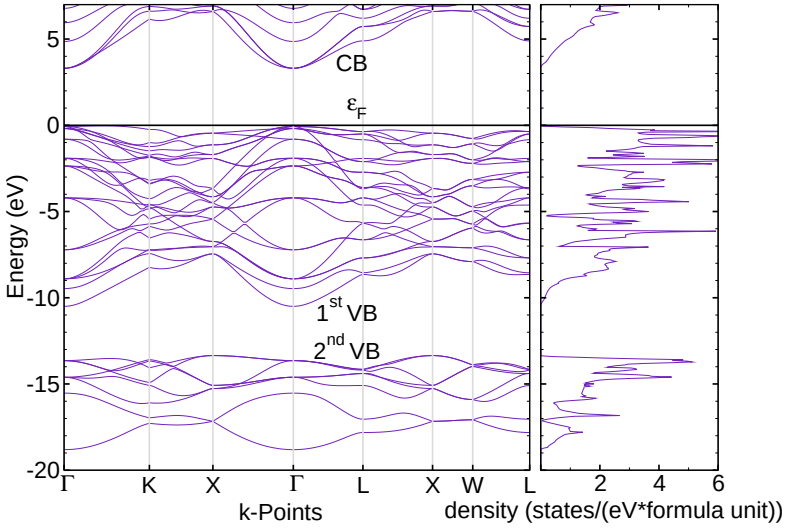

Figure 3.10: Band structure and DoS for γ-silicon nitride. The DoS is of the first Brillouin zone, as obtained in chapter 3.3.2.

of the three crystalline silicon nitride polymorphs the α-phase has the smallest VB and γ-Si_3N_4 has the largest VB. The VB maximum lies at different points in reciprocal space for α-, β- and γ-Si_3N_4. The CB minima of the crystalline phases of Si_3N_4 are each located at the respective Γ-point. Thus all three polymorphs of crystalline silicon nitride have indirect interband thresholds as minimal Kohn-Sham PBE band gaps E_g. γ-Si_3N_4 has the smallest indirect KS PBE band gap, followed by β-Si_3N_4 and finally α-Si_3N_4 with the largest indirect KS PBE band gap of the three polymorphs. This tendency is also observed for the direct Kohn-Sham PBE band gaps. The high pressure γ-phase has the smallest direct KS PBE band gap. The direct KS PBE band gap E_g of the metastable α-phase is larger than that of the stable β-phase.

3.3.2 Partial density of states

The orbital-resolved partial density of states gives insight into the origin of the valence band and the conduction band by supplying data about which types of electrons are predominant in which band. The different orbitals are assigned to the bands of the bulk material by projecting the wavefunctions onto the according spherical harmonic of the atomic orbital. Thus the type of bonding between the atoms can be deducted. If bands cross hybridization can occur. As can be seen from figures 3.8, 3.9 and 3.10 in the previous chapter 3.3.1, the band structure in the crystalline polymorphs of silicon nitride displays many crossings of bands, indicating a high degree of hybridization. A large energy dispersion of bands indicates a large overlap of the orbitals and therefore a high probability for electrons between the atoms. These bands are often similar to the parabolic bands of free electrons. Bands with little dispersion are associated with a high electron probability around the nucleus.

In the present work the s and p orbital-resolved partial density of states (PDoS) of the three crystalline polymorphs of Si_3N_4 are determined. s and p electrons are found in bands

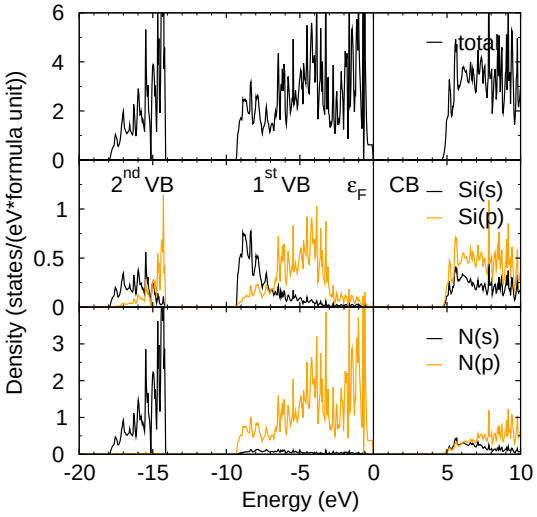

Figure 3.11: PDoS for α-silicon nitride.

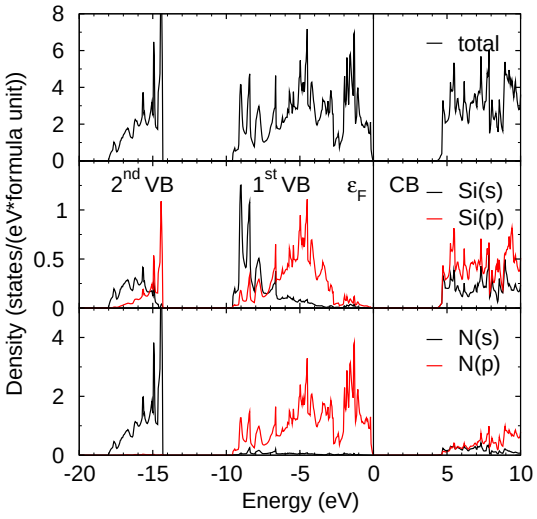

Figure 3.12: PDoS for β-silicon nitride.

with large dispersion. Of interest in γ-Si_3N_4 are the orbital- and site-resolved partial DoS (local DoS or LDoS) of the silicon atoms, as they are either tetrahedrally (Si1) or octahedrally (Si2) coordinated. In order to obtain the PDoS for α-Si_3N_4 and β-Si_3N_4, and the LDoS for γ-Si_3N_4, a similar procedure as for the DoS calculation is carried out, albeit in the entire first Brillouin zone and not along a designated path in **k**-space. A Γ-centered **k**-point mesh is used, with the according values from table 3.1 for each polymorph. Both the structural relaxation and the following optimization at the equilibrium volume V_0 are carried out with the tetrahedron method including Blöchl corrections [15]. The number of grid points in the calculations is set to NEDOS=2001. The relaxation run is performed with the quasi-Newton algorithm RMM-DIIS [18] and the setting ISIF=3. In the optimization run the charge density from the first calculation is applied, by setting the tag ICHARG=11. The tag NBANDS is increased as well to include empty conduction bands. The file vasprun.xml was processed with PYTHON4VASP (p4v) for the construction of figures 3.11, 3.12 and 3.13.

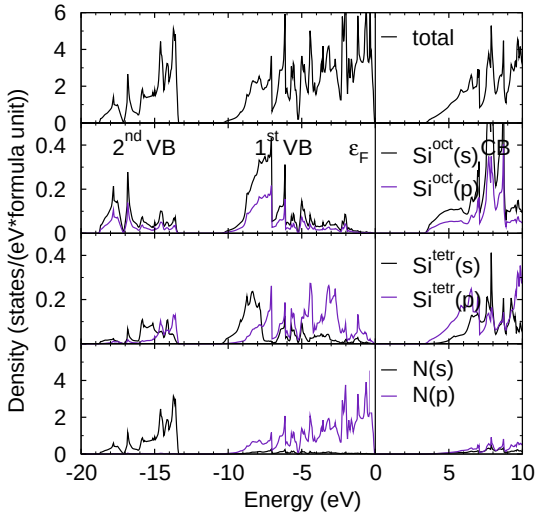

Figure 3.13: Orbital- and site-resolved partial DoS (LDoS) for γ-silicon nitride.

The PDoS of the three crystalline polymorphs of silicon nitride are very similar to one another. A phenomenological approach for describing the PDoS and bonding properties is conducted in reference [57] as well as in reference [58], by construction of a crystal orbital scheme. With the crystal orbital scheme the calculated PDoS of the three crystalline phases of Si_3N_4 are verified together, before further interpretation of their differences. The present findings are consistent with previous experimental findings [5, 55] and *ab-initio* results [48, 54, 56].

The general VB structure of all three crystalline phases are two distinct bands, the lower or 2nd VB and the upper or 1st VB. The 2nd valence band mainly consists of contributions from N ($2s$) electrons, with some Si ($3s$) and Si ($3p$) electrons. More specifically, the bonding σ orbitals of N ($2s$) and Si ($3s$) make up the lowest energy levels in the 2nd VB. The sp interaction between N ($2s$) and Si ($3p$) are mostly found in the 2nd valence band's higher levels. The 1st valence band reaches from approximately -10 eV up to the Fermi level E_F. Different groups [5, 55, 58] have described the 1st VB as consisting of three peaks. One group [54] suggested a five peak structure in the 1st VB. The three peak structure in the 1st VB is also indicated by the present results. It is most prominent

in the α-phase of crystalline Si_3N_4. The lowest peak in the 1st VB mainly consists of N ($2p$) and Si ($3s$) hybrid orbitals. The center peak in the 1st VB contains contributions from pp interaction between N ($2p$) and Si ($3p$) electrons. The VB peak closest to the Fermi level ε_F originates from N ($2p$) non-bonding lone pairs of electrons. Thus, the N ($2p$) bonding bands predominant in the center peak and N ($2p$) non-bonding bands found in the highest peak are merged in the 1st valence band of all three crystalline polymorphs of Si_3N_4. The boundary of these two sets of bands is indicated by the deep dip in the PDoS at approximately -2.5 eV, which has been reported by other groups as well [54]. In γ-Si_3N_4 this boundary is not as distinct as in the other two phases. The fairly delocalized N ($2p$) non-bonding lone pairs of electrons which dominate at the Fermi level result in flat bands for the VB in all three phases. The conduction band of the three crystalline polymorphs of Si_3N_4 contain linear combinations of the anti-bonding levels, mostly Si ($3p$) and N ($2p$).

The electronic structure of the crystalline Si_3N_4 polymorphs is mainly determined through the local short-range order, as observed in reference [59]. Since the local short-range order is very similar in α-, β- and γ-Si_3N_4, it is expected that their electronic structures should also share the main characteristics. Especially the PDoS of α-Si_3N_4 and β-Si_3N_4 match very well. The PDoS of γ-Si_3N_4 shows noteworthy differences. This is due to the octahedrally coordinated Si atoms (Si2 or Si^{oct}). Their ($3s$) electrons dominate the lower part of the 2nd VB, together with nitrogen ($2s$) electrons, as reported in reference [56]. This indicates an energetically favourable state compared to the tetragonal configuration Si^{tetr}. The CB edge in γ-Si_3N_4 mainly consists of Si^{oct} ($3s$) and Si^{tetr} ($3p$) anti-bonding states.

3.4 Optical properties - dielectric tensor

The determination of macroscopic optical properties from microscopic parameters in this work is based on density functional perturbation theory. The macroscopic optical properties are obtained with the macroscopic dielectric tensor, which relates the total electric field in a material to a slowly-varying external field. The microscopic dielectric tensor takes into account that on the atomic scale the microscopic electric field undergoes rapid oscillations. In the independent particle approximation (IPA), the macroscopic dielectric tensor is approximately described by the microscopic frequency dependent dielectric tensor, specifically by the long wavelength limit of the real part of the frequency dependent dielectric tensor. The implementation in VASP is the calculation of the response function in the framework of the PAW method. Detailed accounts are given in references [60] and [61]. In crystals of high symmetry, such as cubic and hexagonal crystals, the nomenclature of the isotropic medium can still be applied along high symmetry directions. A high symmetry direction can be a 3-, 4- or 6-fold rotation axis. In the two phases with hexagonal unit cells, α- and β-Si_3N_4, therefore the components of the dielectric tensor parallel ($\parallel$) and perpendicular ($\perp$) to the c-axes are inspected. The cubic unit cell of γ-Si_3N_4 indicates an isotropic dielectric tensor.

First the static-ion clamped (microscopic) dielectric tensor is obtained, without local field effects. For this the tag LEPSILON is set in INCAR. No summation over empty conduction bands is necessary. Gaussian smearing, ISMEAR=0 with SIGMA=0.1, is applied. **k**-

point sampling is perfomed with the optimized Γ-centered mesh for each of the three crystalline polymorphs. Following the determination of the static dielectric tensor, a second VASP calculation is performed for the frequency dependent dielectric tensor, with identical smearing and **k**-point sampling parameters but with the tag LOPTICS activated in INCAR. The summation over empty states leads to the imaginary part of the (Cartesian) dielectric tensor

$$\varepsilon^{(2)}_{\alpha\beta}(\hat{\mathbf{q}},\omega) = \frac{4\pi^2 e^2}{V} \lim_{q\to 0} \frac{1}{q^2} \sum_{n,m,\mathbf{k}} 2 f_{n\mathbf{k}} \langle u_{m\mathbf{k}+\mathbf{e}_\alpha q} | u_{n\mathbf{k}} \rangle \langle u_{n\mathbf{k}} | u_{m\mathbf{k}+\mathbf{e}_\beta q} \rangle \times \\ \times \left[\delta(\epsilon_{m\mathbf{k}} - \epsilon_{n\mathbf{k}} - \omega) - \delta(\epsilon_{m\mathbf{k}} - \epsilon_{n\mathbf{k}} + \omega) \right] . \tag{3.9}$$

Here $\hat{\mathbf{q}} = \mathbf{q}/|\mathbf{q}|$ is the unit vector, V is the cell volume, $f_{n\mathbf{k}}$ is the occupation function, $\mathbf{e}$ is the microscopic total electric field, ϵ is the one particle energy, and $\omega = \epsilon_{m\mathbf{k}} - \epsilon_{n\mathbf{k}}$ is the transition energy. In insulators as well as semiconductors only interband transitions ($n \neq m$) need to be considered, because no partially filled bands occur, unlike in metals. The real part of frequency dependent dielectric tensor is given by a Hilbert transform, the Kramers-Kronig transform as

$$\varepsilon^{(1)}_{\alpha\beta}(\omega) = 1 + \frac{2}{\pi} P \int_0^\infty \frac{\varepsilon^{(2)}_{\alpha\beta}(\omega')\omega'}{\omega'^2 - \omega^2 + i\eta} d\omega' , \tag{3.10}$$

where P denotes the principal value and η a complex shift of frequency $\omega^c = \omega + i\eta$ to perform a slight Lorentzian broadening. To optimize the summation over empty bands the tag NBANDS is adjusted until the diagonal values of the real frequency dependent dielectric tensor for zero frequency match the diagonal values of the microscopic static dielectric tensor from the first run. Thus a NBANDS value of 384, 192 and 192 was found for α-, β- and γ-Si_3N_4, respectively. The imaginary and real parts of the frequency dependent dielectric tensor are obtained from output file OUTCAR.

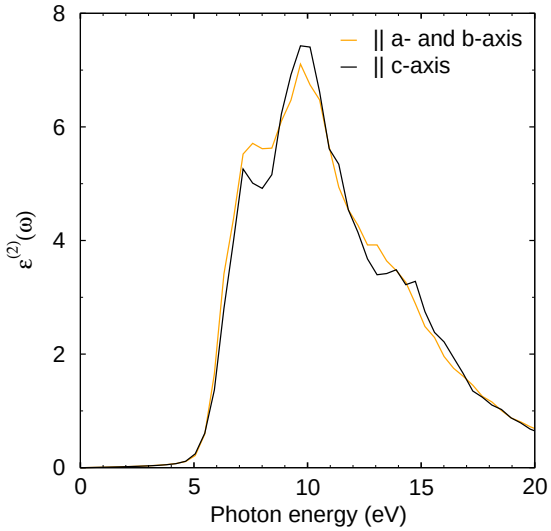

Figure 3.14: Absorption spectrum of α-Si_3N_4. Perpendicular to c-axis, parallel to a- and b-axis it is orange, whereas parallel to c-axis it is black.

The imaginary part of the frequency dependent dielectric tensor represents the absorption

spectrum of a material. The components parallel ($\parallel$) and perpendicular ($\perp$) to the c-axes are plotted in figures 3.14 and 3.15 for the phases with hexagonal cells. For cubic γ-Si_3N_4 one direction is sufficient, which is shown in figure 3.16. All three phases are transparent to photons $0.0 - 5.0$ eV and exhibit an absorption peak structure with a main peak or peaks around 9.5 eV that slopes down with increasing photon energies.

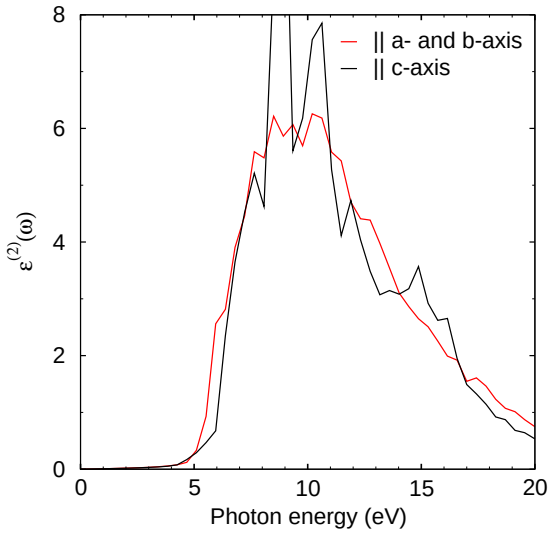

Figure 3.15: Absorption spectrum of β-Si_3N_4. Perpendicular to c-axis, parallel to a- and b-axis it is red, whereas parallel to c-axis it is black.

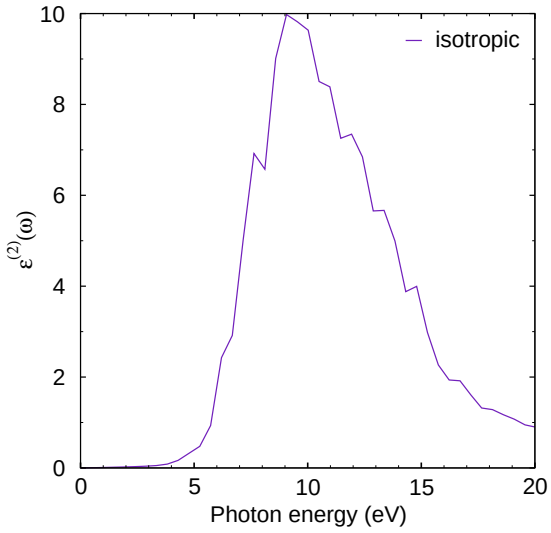

Figure 3.16: Absorption spectrum of γ-Si_3N_4. The cubic unit cell accounts for the isotropic behaviour of this phase.

In α-Si_3N_4 the imaginary frequency dependent dielectric tensor along the c-axis displays a slightly lower peak at 7.0 eV than in the other two directions, as well as a higher main peak at 9.5 eV. The peak at 14.0 eV is shifted to higher photon energies by 1.0 eV and more distinct. The absorption spectrum of β-Si_3N_4 has a comparatively high peak structure between 8.5 eV and 10.5 eV along the c-axis. Additionally a smaller peak at

14.8 eV is found. These features are lacking in the direction of the *a*- and *b*-axes. The main peak in the absorption spectrum of γ-Si_3N_4 is located at 9.0 eV. Clearly γ-Si_3N_4 shows optical isotropy, whereas α- and β-Si_3N_4 have slightly anisotropic characteristics parallel to the *c*-axis due to the hexagonal unit cells.

Table 3.11 shows the diagonal terms, xx, yy and zz, of the static dielectric tensor $\varepsilon^{\text{static}}$ including and excluding local field effects and of the frequency dependent real dielectric function at zero frequency $\varepsilon^{(1)}(0)$. The static dielectric tensor perpendicular to the *c*-axis, $\varepsilon^{\text{static}}(\perp)$, including local field effects of α-Si_3N_4 is higher than $\varepsilon^{\text{static}}(\parallel)$. It is the opposite in β-Si_3N_4, where $\varepsilon^{\text{static}}(\parallel)$ including local field effects is slightly larger than $\varepsilon^{\text{static}}(\perp)$. $\varepsilon^{\text{static}}$ including local field effects of γ-Si_3N_4 is somewhat lower than the calculation without local field effects. A trend is observed, more specifically that the values with local field effects included are lower than their counterparts obtained without considering local field effects. In the lower part of table 3.11 the results excluding local field effects are given. The values of the frequency dependent real dielectric tensor at the zero frequency limit agree well with the values obtained for $\varepsilon^{\text{static}}$, in all three polymorphs. Compared to published values of other *ab-initio* groups, as shown in table 3.11, both the α- and β-phase display less optical anisotropy in this work. The obtained value for γ-Si_3N_4 is considerably higher than the quoted reference [56], conceivably due to the different approach. Most likely the deviation of the present results to other published values is caused by using to few **k**-points in the calculation, as these quantities converge slowly with **k**-points.

	α-Si_3N_4		β-Si_3N_4		γ-Si_3N_4	
property	ref. [a]	present work	ref. [b]	present work	ref. [c]	present work
$\varepsilon^{\text{static}}$ ($\parallel$), incl. local field effects		4.244		4.324		5.285
$\varepsilon^{\text{static}}(\perp)$, incl. local field effects		4.300		4.237		5.285
$\varepsilon^{\text{static}}$ ($\parallel$)		4.397		4.462		5.440
$\varepsilon^{\text{static}}(\perp)$		4.452		4.388		5.440
$\varepsilon^{(1)}(0)$ ($\parallel$)	4.45	4.388	4.01	4.453	4.7	5.432
$\varepsilon^{(1)}(0)(\perp)$	4.09	4.442	3.67	4.379	4.7	5.432

[a] *Ab-initio* data from reference [54], which is obtained from an OLCAO approach based on DFT/LDA.
[b] *Ab-initio* data from reference [54], which is obtained from an OLCAO approach based on DFT/LDA.
[c] *Ab-initio* data from reference [56], which is obtained from an OLCAO approach based on DFT/LDA.

Table 3.11: Static dielectric tensor $\varepsilon^{\text{static}}$ and frequency dependent real dielectric tensor at zero frequency limit $\varepsilon^{(1)}(0)$, parallel to the *c*-axis ($\parallel$) and perpendicular to the *c*-axis ($\perp$), of the three crystalline phases of Si_3N_4 in the independent particle approximation (IPA). Top two lines give values including local field effects, whereas the remaining table states values without local field effects.

3.5 Vibrational properties - zone center phonons

According to the symmetry of the crystal structure different phonons occur. The phonons can be classified as acoustic and optical phonons. Acoustic phonons are used to determine the elastic properties of a crystalline phase, whereas optical phonons give insight into the vibrational modes of the atoms in the crystal. The mathematical formulation is based on group theory. This rather lengthy procedure is detailed in reference [62]. If N is the number of atoms in the lattice, each value of $\mathbf{k}$ has $3N$ phonons or normal modes, where 3 branches are acoustic and $3(N-1)$ are optical. Only the resulting optical phonons for each crystalline polymorph of silicon nitride with respect to the zone center, or Γ-point, are given here.

In general, at points of high symmetry the possible displacements of a crystal's atoms are described as unitary irreducible representations of the group corresponding to the crystal's space group. A set of generators or generating elements give the defining relations for each group. From these defining relations the group multiplication table can be derived, which completely defines the group. The unitary irreducible representations of a group are labelled according to Mulliken (1933), see reference [62]. This notation uses the labels A, B, E and T for real unitary irreducible representations of dimensions 1, 1, 2, and 3, respectively. This means that the A and B modes have single degeneracy, E modes are double degenerate and T modes are triple degenerate. Additionally the labelling ${}^1E$, ${}^2E$ is applied for conjugate pairs of complex unitary irreducible representations, each of dimension 1. The indices g and u denote the unitary irreducible representations which only differ in the sign of the group's character χ. The character χ of a group Λ of matrices $\mathbf{D}$ is defined as a function $\chi(\mathbf{D}) = \mathrm{tr}(\mathbf{D})$. Therefore g modes are symmetric modes with respect to inversion and reflection and u modes are antisymmetric modes.

The crystal symmetry of α-Si_3N_4 places this phase in space group 159 or C_{3v}^4 in Schönflies notation, as discussed in chapter 3.2.1. At the Γ-point the single valued representation of space group 159 is $\mathbf{G}_6^2$, with the generating elements $P = \{C_3^+|000\}$ and $Q = \{\sigma_{d1}|00\frac{1}{2}\}$. Formally, $\mathbf{G}_6^2$ denotes the second group of order six. The point group of the representation $\mathbf{G}_6^2$ is $3m$ (C_{3v}). The labels of the space group representation $\mathbf{G}_6^2$ are A_1, A_2 and E. The E modes are double degenerate. More specifically, the decomposition at the Γ-point is

$$\Gamma_{\mathrm{opt}}^{\alpha} = 13A_1 + 14A_2 + 27E, \tag{3.11}$$

as stated in reference [53]. The $13A_1$ and $27E$ modes of α-Si_3N_4 are both infrared and Raman active, whereas the $14A_2$ modes are inactive.

β-Si_3N_4 has space group 176 (C_{6h}^2). The single valued representation at the Γ-point is $\mathbf{G}_{12}^2$. The generating elements are $P = \{C_3^+|000\}$, $Q = \{C_2|00\frac{1}{2}\}$ and $R = \{I|00\frac{1}{2}\}$. The point group of the representation $\mathbf{G}_{12}^2$ is $6/m$ (C_{6h}). The labelling of the space group representation $\mathbf{G}_{12}^2$ at the Γ-point leads to

$$\begin{aligned}\Gamma_{\mathrm{opt}}^{\beta} = {} & 2A_u + 4A_g + 3B_g + 4B_u + 2({}^1E_{1g} + {}^2E_{1g}) + 4({}^1E_{1u} + {}^2E_{1u}) + \\ & 2({}^1E_{2u} + {}^2E_{2u}) + 5({}^1E_{2g} + {}^2E_{2g}),\end{aligned} \tag{3.12}$$

as given in reference [53]. The E modes consist of conjugate phonon pairs $E = {}^1E + {}^2E$, each of dimension 1. Six modes of β-Si_3N_4, $2A_u$ and $4E_{1u}$, are infrared active. The $4A_g$,

α-Si_3N_4 phonon type	exp.[a]	ref.[b]	present work	(*contd.*) phonon type	exp.	ref.	present work
E	1142	1306.6	1000.2	E	512, 514	601.4	577.9
E	1107	1273.2	990.9	E	499	589.9	547.3
A_2	inactive	1262.8	987.0	A_1	470	544.2	543.0
A_1	1040	1279.1	983.9	A_2	inactive	571.9	522.4
A_2	inactive	1201.1	954.5	A_2	inactive	522.6	495.1
E	1032	1225.2	942.6	A_1	460, 463	528.3	483.0
E	995	1141.6	921.5	E	440	528.5	468.0
A_1	975	974.4	912.8	E	412	518.2	441.7
E	951	1017.5	896.9	A_2	inactive	500.3	433.9
E	935	919.5	892.6	A_2	inactive	452.3	419.8
E	909, 914	835.9	884.6	E	391	468.4	410.0
A_2	inactive	1156.6	878.9	A_1	383	443.4	387.8
E	895	764.5	874.4	E	375	444.9	385.1
A_2	inactive	1113.8	864.1	A_2	inactive	383.7	360.2
A_1	868, 874	786.8	862.6	E	361	397.7	356.8
E	855	742.9	854.7	A_1	355, 356	413.1	350.1
E	848	701.3	841.7	E	337	386.6	340.4
E	763	675.3	835.0	E	321	344.7	335.0
A_1	688, 691	659.9	822.7	E	306	310.0	292.6
E	667	647.9	819.1	A_2	inactive	371.4	290.9
	gap			A_1	298, 300	336.9	287.1
A_2	inactive	865.0	689.9	E	282	261.8	268.2
A_2	inactive	715.9	674.4	A_2	inactive	264.5	257.6
E	600, 601	640.8	670.6	A_1	258	245.7	249.5
A_1	580	638.8	663.9	E	231	220.2	222.6
E	569	613.0	656.9	A_1	202	215.0	222.3
A_1	537	587.3	647.2	E	153	194.9	192.8
A_2	inactive	679.8	597.3				

[a] Raman and infrared absorption spectroscopy data from reference [63], in which the observed peaks are not associated with the phonon type. Additionally a total of 48 instead of 40 IR and Raman active peaks are measured.

[b] *Ab-initio* data from reference [53], which is obtained from an OLCAO approach based on DFT/LDA. The results include a phonon type assignment, thus the phonons are not necessarily in order of decreasing frequencies.

Table 3.12: Wave numbers (cm^{-1}) of zone center phonons in crystalline α-Si_3N_4. E modes are double degenerate. 13 A_1 and 27 E modes are Raman and infrared active. A_2 modes are inactive.

$2E_{1g}$ and $5E_{2g}$ modes of the β-phase are Raman active, adding up to eleven modes. The nine remaining modes of β-Si_3N_4, labeled B_g, B_u and E_{2u}, are inactive.

The space group of γ-Si_3N_4 is 227 (O_h^7). At the Γ-point the single valued representation is $\mathbf{G}_{48}^7$. The generating elements of the group are $P = \{S_{61}^- | \frac{1}{4}\frac{1}{4}\frac{1}{4}\}$, $Q = \{\sigma_x | \frac{1}{4}\frac{1}{4}\frac{1}{4}\}$, $R = \{\sigma_z | \frac{1}{4}\frac{1}{4}\frac{1}{4}\}$ and $S = \{C_{2c} | \frac{1}{4}\frac{1}{4}\frac{1}{4}\}$. The point group of the representation $\mathbf{G}_{48}^7$ is $m3m$ (O_h). The labels of the space group representation $\mathbf{G}_{48}^7$ for the phonon modes of γ-Si_3N_4 at the Γ-point are given as

$$\Gamma_{\text{opt}}^{\gamma} = A_{1g} + 2A_{2u} + E_g + 2E_u + T_{1g} + 4T_{1u} + 2T_{2u} + 3T_{2g} \tag{3.13}$$

in reference [50], where the E modes are double degenerate and the T modes are triple degenerate. The phonon modes $4T_{1u}$ are infrared active. The $1A_{1g}$, $1E_g$ and $3T_{2g}$ modes are Raman active in γ-Si_3N_4, whereas the A_{2u}, E_u, T_{1g} and T_{2u} modes are inactive.

β-Si_3N_4 phonon type	exp.[a]	ref.[b]	present work	(*contd.*) phonon type	exp.	ref.	present work
B_u	inactive	1296.8	1029.5	E_{2g}	619	638.1	597.2
E_{2g}	1047	1309.5	1007.9	E_{1u}	580	573.2	550.6
E_{1u}	1040	1156.1	995.3	B_u	inactive	475.4	541.7
A_g	939	1183.2	908.6	A_g	451	513.9	442.5
E_{2g}	928	990.7	896.0	E_{2g}	229	474.1	431.5
E_{1u}	985	807.8	863.4	E_{1u}	447	478.7	411.1
B_g	inactive	789.1	852.8	B_g	inactive	434.6	394.1
E_{2u}	inactive	651.4	838.7	A_u	380	401.7	356.9
E_{1g}	865	700.6	834.8	E_{2u}	inactive	233.0	297.4
A_u	910	598.4	825.5	B_g	inactive	241.5	262.6
	gap			B_u	inactive	212.8	243.2
A_g	732	690.2	705.8	E_{1g}	210	295.7	218.9
	gap			A_g	186	208.7	198.3
B_u	inactive	601.5	631.8	E_{2g}	144	133.9	177.6

[a] Raman and infrared absorption spectroscopy data from reference [63], in which the measured peaks are not associated with the phonon type. 6 IR and 11 Raman active peaks are observed in accordance with group theory, which permits an approximate phonon type assignment. Thus the phonons are not necessarily in order of decreasing frequencies.

[b] *Ab-initio* data from reference [53], which is obtained from an OLCAO approach based on DFT/LDA. The results include a phonon type assignment, thus the phonons are not necessarily in order of decreasing frequencies. Additionally a total of 6 instead of 5 E_{2g} modes are stated. The omitted mode has a wave number of 233.4 cm^{-1} and is conceivably a typo.

Table 3.13: Wave numbers (cm^{-1}) of zone center phonons in crystalline β-Si_3N_4. $E = ^1E + ^2E$ modes are conjugate phonon pairs, each of dimension 1. 2 A_u and 4 E_{1u} modes are Raman active. 4 A_g, 2 E_{1g} and 5 E_{2g} modes are infrared active. 3 B_g, 4 B_u and 2 E_{2u} modes are inactive.

The VASP determination of phonon frequencies via interatomic force constants is performed with density functional perturbation theory. The PAW method for constructing

the wave functions is applied. Specifically the tags IBRION=8 and LEPSILON=.TRUE. are set in the INCAR file. LEPSILON calculates the Born effective charge tensor from Hellmann-Feynman forces and IBRION=8 the Hessian matrix. The Hessian matrix is the matrix of the second derivatives of the energy with respect to the atomic positions. With it atomic force constants are obtained required for the calculation of phonon frequencies. The symmetries of each system are used to reduce the number of displacements that are considered.

γ-Si_3N_4 phonon type	exp.[a]	ref.[b]	present work	(*contd.*) phonon type	exp.	ref.	present work
A_{1g}	979.5	972	938.3	T_{2u}	inactive	631	604.8
A_{2u}	inactive	946	912.7	T_{1u}	(IR)	619	588.4
T_{2g}	845	840	810.2	E_g	522	522	502.0
T_{1u}	(IR)	819	782.5	T_{1g}	inactive	504	486.0
A_{2u}	inactive	782	759.9	E_u	inactive	455	431.1
E_u	inactive	775	752.3	T_{2g}	420	415	404.1
T_{1u}	(IR)	729	709.0	T_{1u}	(IR)	406	396.1
T_{2g}	727	726	698.3	T_{2u}	inactive	317	304.4

[a] Rietveld refinement of synchrotron x-ray powder diffraction data from reference [25], in which some of the observed Raman peaks are associated with Raman active modes. The phonon type assignment is not in accordance with group theory, as the E_g mode is assigned twice. Thus the assignment of the reference is only regarded for the low E_g mode at 522 cm^{-1} and the T_{2g} mode at 727 cm^{-1} in this table. Infrared (IR) active modes are not obtained.

[b] *Ab-initio* data from reference [50]. VASP calculations within GGA as well as LDA are performed. The exchange-correlation energy functionals are not stated. The wave functions are constructed with the PAW method. The results include a phonon type assignment.

Table 3.14: Wave numbers (cm^{-1}) of zone center phonons in crystalline γ-Si_3N_4. E modes are double degenerate and T modes are triple degenerate. 1 A_{1g}, 1 E_g and 3 T_{2g} modes are Raman active. 4 T_{1u} modes are infrared active. 2 A_{2u}, 2 E_u, 1 T_{1g} and 2 T_{2u} modes are inactive.

In α-Si_3N_4 the phonon frequencies at the Γ-point are between $193 - 671$ cm^{-1} and $819 - 1000$ cm^{-1}, whereas in the gap only inactive modes are present. Compared to *ab-initio* results of reference [53] the phonons in α-Si_3N_4 with the largest wave numbers are approximately softer by 20%. More specifically, this applies to the top 4 E modes, the top 2 A_1 modes and the top 5 A_2 modes. The A_1 modes in α-Si_3N_4 obtained are slightly harder than the other *ab-initio* values of reference [53]. The experimental values [63] show a phonon gap between 700 and 820 cm^{-1}. The region above is between 820 and 1040 cm^{-1}, disregarding the top 2 modes around 1200 cm^{-1}, and the region below contains modes from 700 to below 200 cm^{-1}. Both regions and the gap are indicated by the results in this work and are in very good agreement. β-Si_3N_4 shows phonon frequencies between $178 - 597$ cm^{-1} and $825 - 1029$ cm^{-1}, with only the A_g mode in the gap at 706 cm^{-1}. In comparison to *ab-initio* findings [53], the upper A_u and E_{1g} modes are considerably harder in this work, thus these phonons are moved out of the gap in agreement with the experiment. The Raman active modes are consistent with the calculations of reference [53]. Compared to experimental findings of reference [63], a trend of infrared active modes to be

underestimated by $\approx 10\%$ can be noticed. The Raman active modes agree excellent with the experiment, with only the E_{2g} mode at 431 cm^{-1} sticking out. It has a considerably higher frequency than in the experiment, 240 cm^{-1}. The phonon frequencies of γ-Si_3N_4 are in the range $304-938$ cm^{-1}, without any noteworthy gap. This is in contrast to the modes of the other two crystalline polymorphs of silicon nitride. All vibrational modes, infrared and Raman active as well as inactive modes, of γ-Si_3N_4 are in fair agreement, although slightly softer, compared to *ab-initio* results of reference [50]. The phonon type assignment is identical. With respect to experimental results of reference [25], in which the first assignment of modes to Raman bands is performed, the modes in this work are also slightly lower.

For the three crystalline phases, α-, β- and γ-Si_3N_4, the calculated phonon modes are in general slightly softer, approximately by $5-10\%$, than reported in the references, with larger discrepancies for increasing wave number. This effect may be due to the selected method. Frequencies are very volume dependent. PBE yields too large volumes and therefore too low frequencies. In all three polymorphs the modes at higher frequencies mostly contain contributions from nitrogen atoms. The low frequency modes are mainly dominated by the displacements of the silicon atoms. Notably, the octahedral Si atoms of the γ-phase contribute to the infrared active modes T_{1u}. The octahedrally coordinated silicon atoms are also found to be dominant in most inactive modes of γ-silicon nitride. The Raman active modes can be assigned to the tetrahedral Si atoms and the N atoms.

Chapter 4

Optimized soft potentials

In computational applications the required cpu time is exceedingly important. Thus this chapter compares the results of the VASP calculations from the last chapter, chapter 3, to calculations performed with softer PAW PBE potentials, which are more efficient. A soft and a very soft potential are inspected in addition to the regular potential previously discussed, in order to determine whether one or both are suitable for calculating the properties of the amorphous phases of silicon nitride in chapter 5. The VASP potential file applied in chapter 3, POTCAR.SiN, requires a cut-off energy $E_{\mathrm{cut,\,SiN}} = 520$ eV (400 eV) for variable (fixed) cell volume calculations and constructs basis sets with 250 plane waves per atom. The softer potential file, POTCAR.$\mathrm{Si_sN_{vs}}$, needs a cut-off energy $E_{\mathrm{cut,\,Si_sN_{vs}}}$ of 260 eV (200 eV). The softest used potential, POTCAR.$\mathrm{Si_{vs}N_{es}}$, only requires a cut-off energy $E_{\mathrm{cut,\,Si_{vs}N_{es}}} = 210$ eV (160 eV) and applies 32 plane waves per atom.

In general, higher **k**-point meshes are required for softer potentials to obtain similar smooth energy volume curves. This has been taken into account in the selection of meshes in table 3.1, during the preliminary testing of the **k**-point convergence. Thus a $4 \times 4 \times 4$ mesh is applied for α-Si_3N_4, a $4 \times 4 \times 8$ mesh for β-Si_3N_4 and a mesh of $6 \times 6 \times 6$ for γ-Si_3N_4. In table 4.1 the core radii for each l quantum numbers of the used potentials is given.

core radii (Å)	POTCAR.∗		
l	SiN	$\mathrm{Si_sN_{vs}}$	$\mathrm{Si_{vs}N_{es}}$
0	1.9	1.8	1.9
1	1.9	2.1	2.4
2	1.9	2.1	2.4

Table 4.1: Core radii for each l quantum number as applied by VASP.

For testing the two softer potentials the ground state energy of crystalline α-, β- and γ-silicon nitride are determined. One phase is then selected for further comparison of electronic and vibrational properties. Specifically, the density of states of β-Si_3N_4 is compared to the values from chapter 3.3. To obtain results concerning lattice vibrations the zone center phonons of β-Si_3N_4 are calculated, assigned and compared to the values from chapter 3.5. The calculation of the properties with the two optimized potentials is performed as detailed in the respective chapters, 3.2.2, 3.3.1 and 3.5.

4.1 Electronic properties

4.1.1 Ground state energy

Ground state energy E_0 and cell volume V_0 are derived from the Birch-Murnaghan equation of state (3.1). The chart in figure 4.1 shows the data points including fit that are calculated with each POTCAR for the three crystalline phases. A general trend of rising ground state energy relative to the atom with lower plane wave cut-off can be clearly seen for all three polymorphs of silicon nitride.

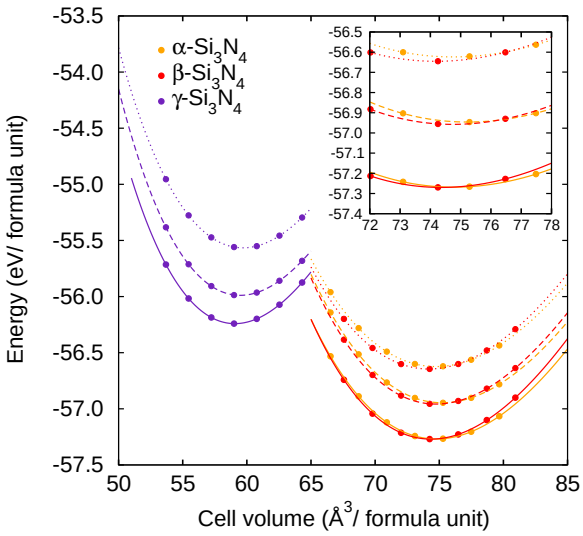

Figure 4.1: Equations of state of crystalline Si_3N_4. The solid lines represent the fits to results obtained with the regular potential POTCAR.SiN, the dashed lines those of the soft POTCAR.Si_sN_{vs}, and the dotted lines are fits to values obtained with the very soft POTCAR.$Si_{vs}N_{es}$. The inset shows the region around the minimum of α- and β-Si_3N_4.

E_0 (eV/formula unit)	POTCAR.∗					
	SiN		Si_sN_{vs}		$Si_{vs}N_{es}$	
phase	E_0	ΔE (meV)	E_0	ΔE (meV)	E_0	ΔE (meV)
α-Si_3N_4	-57.267	0.0	-56.946	0.561	-56.622	1.126
β-Si_3N_4	-57.269	0.0	-56.956	0.547	-56.643	1.093
γ-Si_3N_4	-56.218	0.0	-55.966	0.448	-55.543	1.201

Table 4.2: Ground state energy E_0 of the crystalline silicon nitride phases (per formula unit). The difference in ground state energy to results obtained with the regular potential POTCAR.SiN is given in meV. Energies are specified with respect to spherical non-spin polarized atoms.

Table 4.2 lists the calculated ground state energy E_0 per formula unit of the silicon nitride phases for the three inspected potentials. With all three potentials the naturally stable β-phase has the lowest ground state energy, as expected. The inset in figure 4.1 shows the region around the minimum of α- and β-Si_3N_4. The fits to results of the β-phase lie lower than those of the α-phase, indicating that β-Si_3N_4 is the stable polymorph. The energy difference between α- and β-Si_3N_4 slightly increases for the optimized potentials. The high pressure polymorph γ-Si_3N_4 has a higher ground state energy with respect to the α- and β-phase obtained with the same potential. The difference in ground state energy ΔE_0 in meV for results of each phase between regular and soft potential as well as regular and very soft potential are given in table 4.2. Noteworthy is the similar tendency of higher E_0 for both optimized potentials, regardless of the particular phase, i.e. a uniform shift of the energy is observed.

V_0 (Å^3/formula unit)	POTCAR.*		
phase	SiN	Si_sN_{vs}	$Si_{vs}N_{es}$
α-Si_3N_4	74.70	75.85	74.16
β-Si_3N_4	74.33	74.40	73.69
γ-Si_3N_4	58.96	59.12	59.35

Table 4.3: Equilibrium cell volume V_0 of the crystalline silicon nitride phases (per formula unit).

Table 4.3 displays the equilibrium cell volume V_0 per formula unit of α-, β- and γ-Si_3N_4 for comparison. Interestingly α-Si_3N_4 shows a somewhat "mixed" tendency for the applied potentials. The lowest ground state energy is achieved with the SiN-potential but the smallest cell volume with $Si_{vs}N_{es}$-potential. Nonetheless, the calculated cell volume is in both cases very close to the results obtained with the regular potential, as the values for V_0 differ by less than 0.8%. VASP calculations of β-Si_3N_4 show that the $P6_3$-modification tends to converge towards the $P6_3m$-structure, see table 3.3 in chapter 3.2.1. In preliminary tests this is also verified for the optimized soft potentials, before further calculations are performed. All three potentials lead to comparable results. The cell volume obtained with the Si_sN_{vs}-potential has the greatest deviation, approximately 0.6%. The third phase, γ-Si_3N_4, shows reasonable results with both optimized soft potentials. The difference is less than 1.0% when comparing the Si_sN_{vs}-potential to the SiN-potential. Even the softest potential leads to results only 1.5% off.

The results obtained with the very soft potential for α-Si_3N_4 and β-Si_3N_4 are closer to experimental values, see table 3.6, than those from the calculation with the regular potential, indicating that the $Si_{vs}N_{es}$-potential is an excellent compromise for further calculations with amorphous phases to ensure both accuracy and high efficiency.

4.1.2 Density of states

From here on only the properties of β-Si_3N_4 are inspected and compared, as the results for ground state energy E_0 and equilibrium cell volume V_0 obtained in chapter 4.1.1 displayed an overall consistency in accordance with the applied potential, for all three crystalline polymorphs of silicon nitride.

β-Si_3N_4		present work, POTCAR.*		
property (eV)	exp. [a]	SiN	Si_sN_{vs}	$Si_{vs}N_{es}$
CB min.		Γ	Γ	Γ
VB max.		$\Gamma \rightarrow A$	$\Gamma \rightarrow A$	$\Gamma \rightarrow A$
E_g min.	4.6-5.5	4.25	4.20	4.17
E_g at Γ		4.45	4.41	4.40
bottom 1st VB		-10.14	-9.96	-10.07
top 2nd VB		-14.73	-14.62	-14.94
width 1st VB	10-12	10.14	9.96	10.07
width 2nd VB	4-5	3.79	3.70	3.52
full width VB		18.52	18.32	18.46

[a]Data cited in reference [41], from XPS and BIS as well as from photoemission experiments.

Table 4.4: KS PBE band gap E_g of β-Si_3N_4 with the three potentials, min. and direct at the Γ-point. The experimental values for E_g denote the optical band gap. The VB widths and the location of the CB min. and VB max. are detailed.

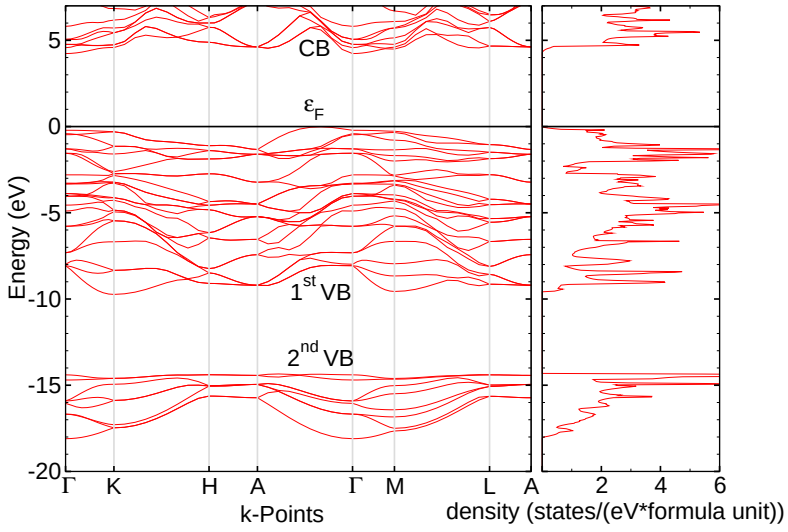

Figure 4.2: DoS and band structure of β-Si_3N_4 with regular potential POTCAR.SiN.

The **k**-point path is selected as in table 3.9. The DoS and band structure of β-Si_3N_4 are in excellent agreement for both optimized potentials. Figures 4.2, 4.3 and 4.4 show the density of states and band structure for VASP calculation with the regular SiN-potential, soft Si_sN_{vs}-potential, and very soft $Si_{vs}N_{es}$-potential, respectively. The results are summarized in table 4.4.

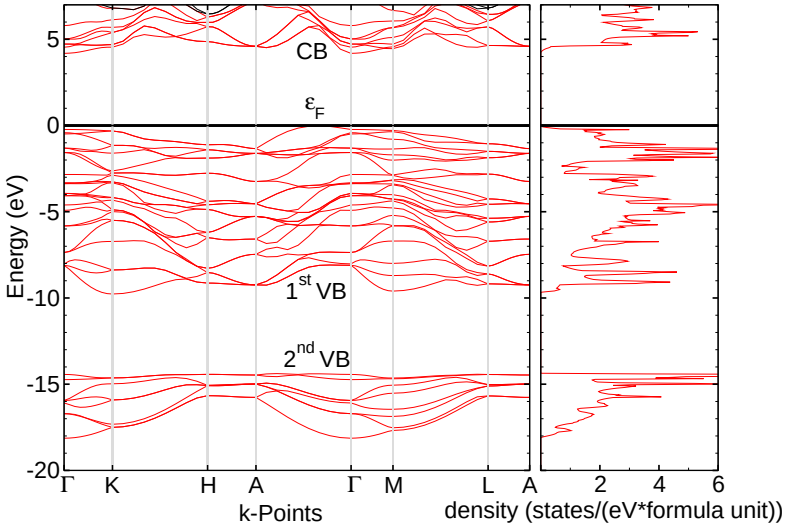

Figure 4.3: DoS and band structure of β-Si_3N_4, obtained with soft potential POTCAR.Si_sN_{vs}.

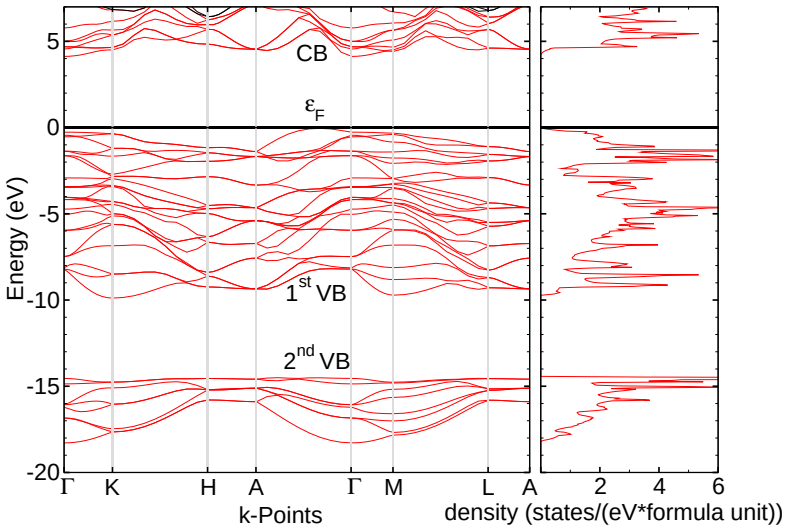

Figure 4.4: DoS and band structure of β-Si_3N_4, obtained with very soft potential POTCAR.$Si_{vs}N_{es}$.

The full valence band in β-Si_3N_4 calculated with the soft potential is the narrowest, with 18.4 eV. It consists of a 1st and 2nd VB with a width of 10.0 eV and 3.7 eV, respectively. The widths obtained with the very soft potential are slightly larger for the 1st VB, 10.1 eV, and smaller for the 2nd VB, 3.5 eV. The full width of the VB is 18.5 eV. This indicates an increase in the separating gap between the 1st and 2nd VB in calculations with the very

soft potential of 0.3 eV compared to the regular potential and of 0.2 eV in comparison to the soft potential. The VB maximum as well as the CB minimum of β-Si_3N_4 are at the same respective points in **k**-space for both of the optimized potentials as they are in the calculation with the regular potential. The experimental reference values for E_g min. of β-Si_3N_4 listed in table 4.4 are larger by $\approx 10-30$ % for all three inspected potentials. This is due to the general band gap underestimation in density functional theory. Within DFT, the results for the indirect Kohn-Sham PBE band gap, E_g min., and direct KS PBE band gap, E_g at Γ, are consistent for both optimized potentials. A trend of slightly decreasing indirect and direct KS PBE band gap with softer potential is observed. On the other hand, even results with the very soft potential deviate by less than 2 % from values obtained with the regular potential, which is very reasonable.

4.2 Vibrational properties - zone center phonons

The zone center phonons of β-Si_3N_4 obtained with the optimized potentials are compared to the phonons calculated with the regular potential. The results are given in table 4.5. A general tendency can be observed. The softer the potential, the lower the modes with large wave numbers and the higher the modes with small wave numbers. For the soft potential POTCAR.Si_sN_{vs} the trend goes from slight underestimation to overestimation with the A_g mode at 708.8 cm^{-1}, whereas this occurs lower, with the E_{1u} mode at 554.0 cm^{-1}, in calculations with the very soft potential POTCAR.$Si_{vs}N_{es}$. A comparison of the potentials shows that the phonon frequencies may differ in absolute values, but the phonon assignment remains largely the same. One exception is the very soft potential POTCAR.$Si_{vs}N_{es}$, which switches two phonon frequencies by placing the E_{2g} mode at 443.5 cm^{-1} and the A_g mode at 440.5 cm^{-1}.

4.3 Discussion

Compared to the regular potential SiN, the ground state energy shows a minimum at the same cell volume, within 1.5 %, for both optimized potentials Si_sN_{vs} and $Si_{vs}N_{es}$. Similarly, the density of states are in exceptional agreement for all three potentials. The Kohn-Sham PBE band gap is reproduced accurately, within 2.0 %. The calculated phonons and their respective type assignments agree well. Even the very soft potential exhibits only errors of 50 cm^{-1} for the high frequency modes and only 10 cm^{-1} for modes with a frequency below 400 cm^{-1}. On average, the errors remain well below 5.0 %, which is in fact small compared to the DFT/PBE errors, and tiny compared to effective many body potentials. Using such a potential the the number of plane waves per atom can be reduced to about 30 PW, very respectable, at a modest loss of accuracy.

It is concluded that both optimized potentials can be used for VASP calculations of amorphous silicon nitride and the amorphous silicon-nitrogen alloys. Since the very soft potential $Si_{vs}N_{es}$ is quite accurate, and is the most efficient regarding computational time, it is selected for further calculations.

β-Si_3N_4			POTCAR.∗		
phonon type	exp.[a]	ref.[b]	SiN	Si_sN_{vs}	$Si_{vs}N_{es}$
B_u	inactive	1296.8	1029.5	1022.9	973.3
E_{2g}	1047	1309.5	1007.9	1004.4	953.7
E_{1u}	1040	1156.1	995.3	992.2	936.3
A_g	939	1183.2	908.6	906.0	850.9
E_{2g}	928	990.7	896.0	895.7	835.6
E_{1u}	985	807.8	863.4	862.8	799.4
B_g	inactive	789.1	852.8	851.2	791.8
E_{2u}	inactive	651.4	838.7	836.8	776.2
E_{1g}	865	700.6	834.8	832.2	771.5
A_u	910	598.4	825.5	822.5	761.4
		gap			
A_g	732	690.2	705.8	708.8	698.7
		gap			
B_u	inactive	601.5	631.8	630.1	601.3
E_{2g}	619	638.1	597.2	600.0	582.0
E_{1u}	580	573.2	550.6	555.5	554.0
B_u	inactive	475.4	541.7	538.2	523.4
A_g	451	513.9	442.5	445.4	443.5 (E_{2g})
E_{2g}	229	474.1	431.5	438.6	440.5 (A_g)
E_{1u}	447	478.7	411.1	416.1	421.3
B_g	inactive	434.6	394.1	401.4	416.5
A_u	380	401.7	356.9	364.3	379.6
E_{2u}	inactive	233.0	297.4	299.0	304.4
B_g	inactive	241.5	262.6	266.1	272.6
B_u	inactive	212.8	243.2	248.0	258.7
E_{1g}	210	295.7	218.9	220.5	223.9
A_g	186	208.7	198.3	199.0	198.7
E_{2g}	144	133.9	177.6	175.4	183.4

[a] Raman and infrared absorption spectroscopy data from reference [63], in which the measured peaks are not associated with the phonon type. 6 IR and 11 Raman active peaks are observed in accordance with group theory, which permits an approximate phonon type assignment. Thus the phonons are not necessarily in order of decreasing frequencies.

[b] *Ab-initio* data from reference [53], which is obtained from an OLCAO approach based on DFT/LDA. The results include a phonon type assignment, thus the phonons are not necessarily in order of decreasing frequencies. Additionally a total of 6 instead of 5 E_{2g} modes are stated. The omitted mode has a wave number of 233.4 cm^{-1} and is conceivably a typo.

Table 4.5: Comparison of wave numbers (cm^{-1}) of zone center phonons in β-Si_3N_4 obtained with the three potentials to experimental and *ab-initio* references. $E = {}^1E + {}^2E$ modes are conjugate phonon pairs, each of dimension 1. 2 A_u and 4 E_{1u} modes are Raman active. 4 A_g, 2 E_{1g} and 5 E_{2g} modes are infrared active. 3 B_g, 4 B_u and 2 E_{2u} modes are inactive.

Chapter 5

Amorphous silicon-nitrogen alloys

Here amorphous silicon nitride a-Si_3N_4 and the amorphous silicon-nitrogen alloys a-Si_xN_y are inspected. In addition an analysis of the according hydrogenated structures, a-Si_3N_4:H and a-Si_xN_y:H, is performed. More specifically, the alloys indicated in table 5.1 are taken into consideration.

	atoms in super cell				H content
alloy	Si	N	H	total	(at.%)
a-Si	96			96	
a-Si_3N	96	32		128	
a-Si_3N_2	96	64		160	
a-Si_3N_3	96	96		192	
a-Si_3N_4	96	118		224	
a-Si_3N_5	84	140		224	
a-Si_3N_3:H	96	96	32	224	14.3
a-Si_3N_4:H	87	116	20	223	9.0
a-Si_3N_4:NH_3	84	119	21	224	9.4

Table 5.1: Number of atoms in the super cells of the amorphous silicon-nitrogen alloys. Hydrogen content, where applicable, is given in a percentage of the total number of atoms per super cell.

The structural and electronic properties of amorphous unhydrogenated and hydrogenated silicon nitride, a-Si_3N_4 and a-Si_3N_4:H, and silicon-nitrogen alloys a-Si_xN_y and a-Si_xN_y:H are derived. Where available, the results are compared to experimental data and to other simulation results. The focus is placed on a-Si_3N_3, a-Si_3N_4, a-Si_3N_3:H and a-Si_3N_4:H. These specific alloys are selected because they are in the stoichiometric range of technical applications [2, 64]. One important aspect is to verify whether hydrogen acts as an electron donor or acceptor in amorphous hydrogenated silicon nitride a-Si_3N_4:H and in the silicon-nitrogen alloy a-Si_3N_3:H, as both tendencies have been reported [64, 65]. As outlined in chapter 1, the main areas of interest are structural defects, their correlation with electronic defect levels as well as the formation of Si random percolation networks in the amorphous silicon-nitrogen alloys.

VASP is used for *simulated annealing* [13] performed with the optimized very soft potential POTCAR.$Si_{vs}N_{es}$. These *ab-initio* molecular dynamics (MD) simulations are performed within density functional theory. The electron-ion interaction is handled with the PAW method [16]. The exchange-correlation energy functional is parametrized with the PBE scheme [20]. The core radii for the l quantum numbers is given in table 4.1. The calculations are performed with a cut-off energy of $E_{\text{cut}} = 160$ eV, as discussed in chapter 4. Where possible without compromising the results, a lower cut-off energy E_{cut} of 120 eV is used for

the expansion of the plane wave basis set. Only the Γ-point is used to sample the Brillouin zone. The simulations are conducted with velocity scaling, in which every 50 steps v is rescaled to yield

$$\frac{v^2}{2m} = \frac{3}{2}k_B T\,. \tag{5.1}$$

The model structures are generated from crystalline α-Si_3N_4, with certain atoms replaced by others in the POSCAR file to account for the different stoichiometry. The model structure of amorphous silicon a-Si is constructed from crystalline silicon with a fcc diamond unit cell and the amorphous silicon-nitrogen alloy a-Si_3N_4:NH_3 is created from α-Si_3N_4 and ammonia. Vegard's law is applied to calculate the change in cell volume when atoms of one element are substituted by atoms of another element. With the model structures simulated annealing calculations are performed at a high temperature, 5500 K. At this temperature the structures melt and are in a liquid state. Then the temperature is lowered, in general in increments of 500 K, for each consecutive MD run until amorphous structures are obtained. Finally a quenched MD run relaxes the ions into the local minimum. This is called the quenched-from-melt procedure. The temperature at which the quenched-from-melt procedure is carried out depends on the properties that are to be deduced and are stated in each chapter separately.

5.1 Structural properties

The structural properties of amorphous silicon nitride and of the amorphous silicon-nitrogen alloys are investigated through the quenched-from-melt structures. Initially, the volume per atom and density are calculated, followed by an inspection of the temperature history. Then the mean square displacement and diffusion coefficient are obtained to deduct the dynamical properties of the liquid alloys. The pair correlation function is interpreted after this and the bond angle distribution as well. The calculation of the coordination numbers of atoms to gain insight into the local environment, occurrence of structural defects and the possibility of formation of a random percolation network of silicon concludes the chapter.

5.1.1 Volume per atom and density

The volume per atom VPA and from it the mass density ρ is calculated. This is performed to evaluate whether the model structures are comparable to experimental findings and other simulation results. Experimentally a wide range of densities is observed in the amorphous silicon-nitrogen alloys including stoichiometric silicon nitride, although densities between 2.8 eV and 3.0 eV are preferable in most technical applications [64].

	VPA (Å^3/atom)			ρ (g/cm^3)		
alloy	exp. [a]	sim. [b]	present work	exp. [c]	sim. [d]	present work
a-Si	19.66		20.51	2.37		2.27
a-Si_3N	15.69		16.08	2.60		2.54
a-Si_3N_2	13.30		13.42	2.80		2.78
a-Si_3N_3	11.71	11.68	11.65	2.98	2.99	3.00
a-Si_3N_4	10.57	10.08[e], 10.60	10.38	3.15	3.14	3.20
a-Si_3N_5	9.72		10.38	3.29		3.08
a-Si_3N_3:H	11.71		11.65	2.98		3.02
a-Si_3N_4:H	10.57		10.84	2.77[f], 3.15		3.09
a-Si_3N_4:NH_3	10.34		10.84	3.18		3.05

[a] XPS and IR absorption data from reference [6] of hydrogenated alloys.
[b] MD simulation data from reference [66], which is based on a classical force field approach.
[c] XPS and IR absorption data from reference [6] of hydrogenated alloys.
[d] MD simulation data from reference [66], which is based on a classical force field approach.
[e] *Ab-initio* data from reference [48]. VASP calculations with the Perdew-Zunger parametrization of the Ceperly-Alder functional within LDA are performed. The wave functions are constructed with the PAW method.
[f] IR absorption data from reference [67] with ratios N/Si = 1.3 and H/Si = 0.9.

Table 5.2: Volume per atom VPA and mass density ρ of amorphous silicon-nitrogen alloys. Reference values are quoted where available. In experimental samples there is always some hydrogen present, due to the small volume and molar mass compared to Si or N it is usually disregarded. The density obtained in the present work includes the hydrogen contribution as can be taken from table 5.1.

The VPA and density ρ of the amorphous silicon-nitrogen alloys and of a-Si are obtained from the quenched-from-melt structures, which are first annealed down to a temperature of 1500 K and 500 K, respectively. The results, given in table 5.2, are well within the range indicated by available references.

In amorphous silicon a-Si the volume per atom is 20.51 Å^3. The Si-richest alloy a-Si_3N has a smaller VPA of 16.08 Å^3. The remaining substoichiometric alloys display decreasing volumes per atom from 13.42 Å^3 to 11.65 Å^3 in a-Si_3N_2 and a-Si_3N_3, respectively. Amorphous silicon nitride a-Si_3N_4 and the suprastoichiometric alloy a-Si_3N_5 are found to have an volume per atom of 10.38 Å^3. The largest decrease in VPA is observed between a-Si and a-Si_3N. The density ρ increases by $8-11\%$ for each alloy from 2.27 g/cm^{-3} in a-Si to 3.20 g/cm^{-3} in a-Si_3N_4, whereas it decreases in the suprastoichiometric alloy a-Si_3N_5 to 3.08 g/cm^{-3}.

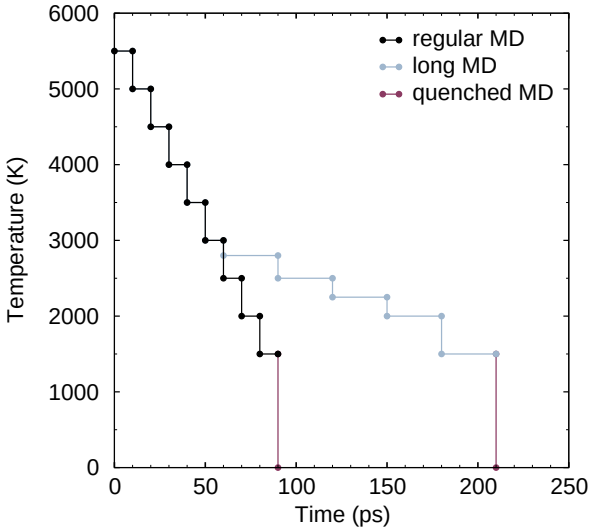

Figure 5.1: Annealing history of MD runs including quenched MD.

The actual annealing history for the MD calculations is shown in figure 5.1. The regular MD runs are performed over 10 ps, whereas the long MD runs over 30 ps. Afterwards a quenched MD run relaxes the atoms into the instantaneous ground state.
To ensure that the simulated annealing procedure yields amorphous structures of sufficient quality, the running average of the energy is compared to the energy after ionic relaxation. Specifically, from the VASP calculations carried out at 2500 K a running average of the energy is taken over 1000 time steps. Simultaneously, every 1000 time steps a snapshot of the structure is taken and relaxed into the local minimum with a quenched MD run. For a-Si_3N_4 at 2500 K this is illustrated over 10 ps in figure 5.2. It is easily seen that the relaxed configuration roughly follows the average energy in simulated annealing and the tendency of lower energies with longer run duration is achieved. Therefore it is of importance to determine at which run times this decrease in energy stops. Typically, the energy settles in 5 ps, but it is also possible that the energy increases during a MD run. There is no guarantee that a longer simulation time actually lowers the energy.

Previous work [66] suggests that temperatures above 5000 K combined with long simulation times of 100 ps are required to obtain a stable amorphous state instead of a metastable

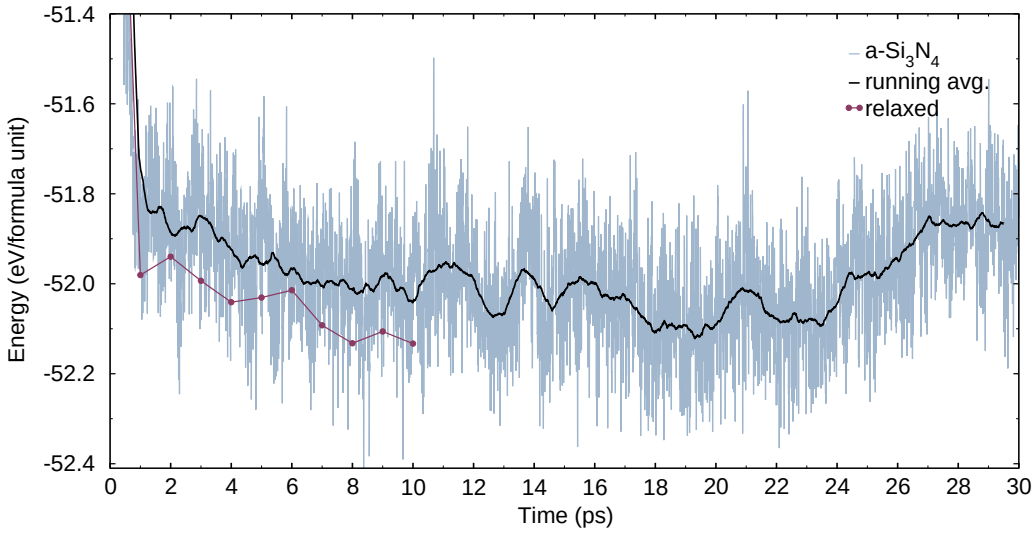

Figure 5.2: DFT energy, running average and relaxed energy of amorphous silicon nitride a-Si_3N_4 at 2500 K.

state in the quenched-from-melt structure. The high temperatures are used in the initial simulated annealing procedure. Regarding the MD run time a VASP run of 30 ps is performed at 2500 K, as shown in figure 5.2. The structure relaxes into a minimum after approximately 10 ps, but begins to settle into an energetically more unfavourable state after 25 ps. This indicates that jump diffusion processes, stochastic processes where one atom jumps to another site, accumulate defects in the structure. Therefore a MD time between 10 ps and 20 ps at each temperature is suggested, in order to avoid accumulation of defects.

5.1.2 Mean square displacement and diffusion coefficient

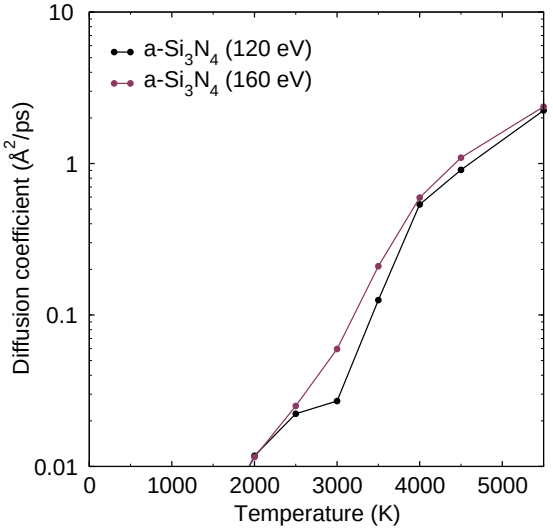

Figure 5.3: Diffusion coefficients of amorphous silicon nitride a-Si_3N_4. Comparison of simulations with different plane wave cut-off energies 120 eV and 160 eV.

The diffusion of atoms in materials is described by Fick's first and second law of diffusion. First step for determining the diffusion coefficients of the amorphous silicon-nitrogen alloys is to identify the minimal cut-off energy E_{cut} of the plane wave basis set. For this, a-Si_3N_4 is calculated with two settings of the flag ENCUT in the INCAR file. The comparison of diffusion coefficients obtained with different cut-off energies for a-Si_3N_4 is pictured in figure 5.3 on a semi-logarithmic scale. The agreement is good, within statistical uncertainties. Merely the curve with the lower E_{cut} shows an uncharacteristic dent between 2500 K and 4000 K which is not reproduced by the calculation with the higher cut-off energy. Therefore it is recommended to apply a cut-off energy of $E_{\text{cut}} = 160$ eV for determining the diffusion coefficients.
VASP, during the quenching of the structure from the molecular dynamics simulation, stores the positions of all sets in the file XDATCAR. From this the mean square displacement (msd) is calculated, which can be used to obtain the diffusion coefficient $D(t)$. A linear mean square displacement shows that the phase is liquid. At and below 0.3 Å^2 the msd is considered constant, indicating a solid phase.

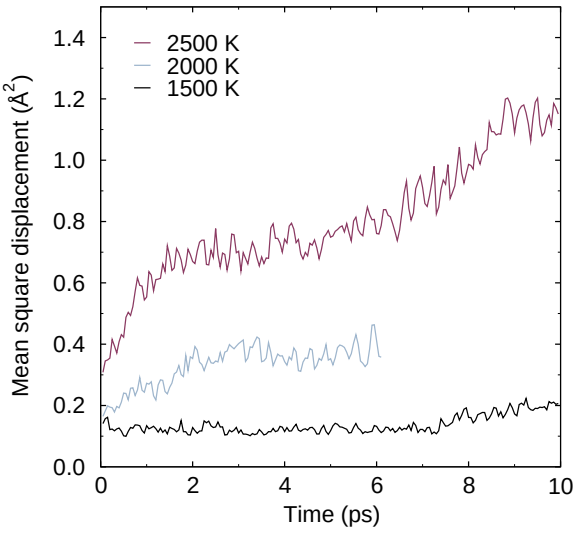

Figure 5.4: Mean square displacement (msd) of amorphous silicon nitride a-Si_3N_4 at different temperatures. A constant msd indicates a solid, whereas a linearly increasing msd shows a liquid phase.

The mean square displacement of amorphous silicon nitride at different temperatures is plotted in figure 5.4. The experimental melting point of crystalline Si_3N_4 is 2173 K [68]. Thus the transition from solid to liquid in amorphous silicon nitride is to be expected somewhere around 2200 K. This agrees with the simulation results, where at 1500 K we see no liquid-like diffusion. At 2000 K, and even more so at 2500 K, the msd displays liquid characteristics. Interestingly, the msd of amorphous silicon nitride a-Si_3N_4 at 2500 K exhibits features similar to plateaus between 1.5 ps and 4.5 ps, between 5.0 ps and 6.0 ps as well as after 8.5 ps. This indicates that the structure spontaneously "freezes" in certain configurations, which is facilitated by the stoichiometric Si and N content. Therefore even higher temperatures than in experiments are required to observe significant diffusion in amorphous silicon nitride or to successfully melt the structure in MD simulations.

The diffusion coefficients $D(t)$ of amorphous silicon a-Si and silicon-nitrogen alloys a-Si_3N_y

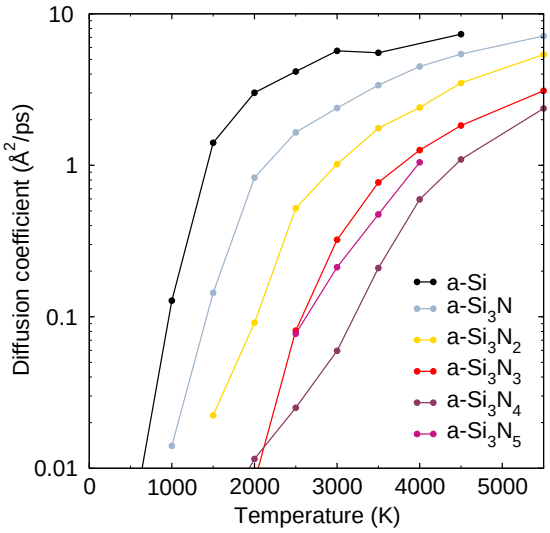

Figure 5.5: Diffusion coefficient of amorphous silicon and silicon-nitrogen alloys with varying stoichiometry. The substoichiometric alloys as well as the suprastoichiometric silicon nitrogen alloy a-Si_3N_5 display a higher diffusivity than a-Si_3N_4.

with y $= 1, 2, 3, 4, 5$ are plotted in figure 5.5. Clearly the substoichiometric structures as well as the suprastoichiometric alloy show higher diffusion at lower temperatures. Amorphous silicon nitride a-Si_3N_4 exhibits the lowest diffusivity at any given temperature. To obtain a rough feeling for the temperature at which the amorphous silicon-nitrogen alloys freeze in our simulations we arbitrarily set a threshold of 0.1 Å^2/ps for the diffusion coefficient and determined at which temperature $D(t)$ drops below this value. Table 5.3 gives the temperature at which the onset of diffusion occurs.

alloy	$T_{\mathrm{Si,N}}$ (K)	T_{H} (K)
a-Si	960	
a-Si_3N	1420	
a-Si_3N_2	2020	
a-Si_3N_3	2580	
a-Si_3N_4	3210	
a-Si_3N_5	2640	
a-Si_3N_3:H	2350	1650
a-Si_3N_4:H	2740	1550
a-Si_3N_4:NH_3	3160	1720

Table 5.3: Onset of diffusion for Si, N as well as for H in amorphous silicon and amorphous silicon-nitrogen alloys. The threshold for diffusion is set to be 0.1 Å^2/ps.

The diffusion of hydrogen is displayed separately, to account for the different diffusive character of hydrogen in comparison to Si or N. In the silicon-nitrogen alloy derived from silicon nitride and ammonia a-Si_3N_4:NH_3 the H atoms are slightly less diffusive than in a-Si_3N_3:H or a-Si_3N_4:H, and cross the threshold at a temperature of 1720 K. Si and N atoms

in a-Si_3N_4:NH_3 begin diffusing above 3160 K, as given in table 5.3. This is the highest onset of diffusion in the inspected hydrogenated alloys. The diffusion coefficients of figure 5.5 are used as a "scale" for a-Si_3N_3:H and a-Si_3N_4:H in figures 5.6 and 5.7, respectively. The diffusion of Si and N atoms in a-Si_3N_3:H takes place at lower temperatures than in the unhydrogenated alloy a-Si_3N_3, starting at approximately 2350 K. At temperatures upward of 2800 K the diffusivity follows the curve obtained for a-Si_3N_3, albeit at slightly higher values. Diffusion of H in a-Si_3N_3:H is observed at temperatures above 1650 K. In a-Si_3N_4:H the H atoms remain diffusive down to a significantly lower temperature than for Si and N diffusion in the same alloy. The H diffusion coefficient in hydrogenated amorphous silicon nitride crosses the threshold of 0.1 $Å^2$/ps at 1550 K. For Si and N atoms diffusion takes place upward of 2740 K.

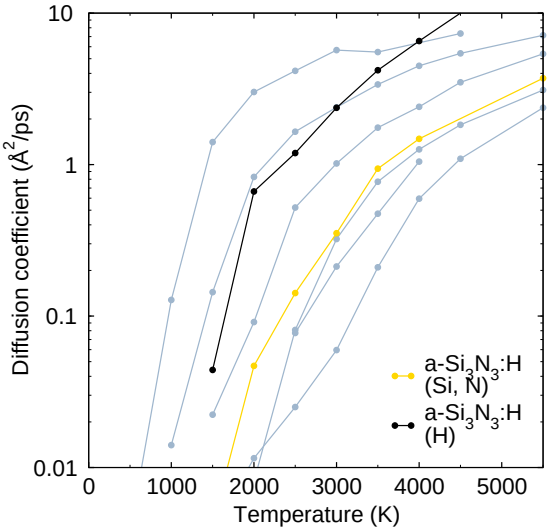

Figure 5.6: Diffusion coefficient of hydrogenated amorphous a-Si_3N_3:H.

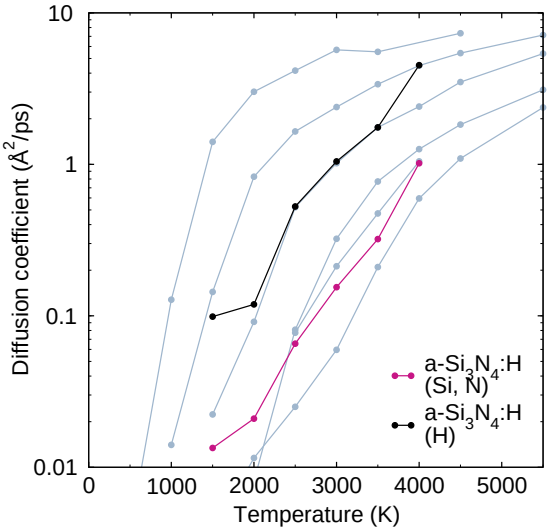

Figure 5.7: Diffusion coefficient of hydrogenated amorphous silicon nitride a-Si_3N_4:H.

5.1.3 Pair correlation function

In crystals the atomic configuration leads to sharp peaks of the neighboring atoms at certain distances from each atom. However, in amorphous materials this order is not given and the pair correlation function represents a statistical measure for the number of neighboring atoms. The pair correlation function (pcf) is defined as

$$g(\mathbf{r}) = \frac{V}{4\pi \mathbf{r}^2 N^2} \langle \sum_i \sum_{j \neq i} \delta\left(\mathbf{r} - \mathbf{r}_{ij}\right) \rangle \,, \tag{5.2}$$

where V is the volume, N is the number of atoms and the indices $i, j = 1, \ldots, N$. It is the conditional probability density of finding an atom at $\mathbf{r}$, if there is one at the coordinate origin. Close to any central atom the pair correlation function is approximately zero. It then rises to the first maximum, where the nearest neighbor atoms are located. The minima of the pair correlation function indicate the regions at which there is only a low probability of finding another atom. The maxima correspond to the typical or average neighbor distances between the atoms. In amorphous materials, far from each atom the pair correlation function approaches unity, as there is no long range order. To obtain the various bond lengths the element specific local environments are considered. More specifically, the neighbor pairs Si-Si, Si-N, Si-H, N-N, and N-H are taken into account in the partial pcf. The data is obtained from the quenched-from-melt structures of the molecular dynamics simulations performed at a temperature of 500 K for *a*-Si, at 2000 K for *a*-Si_3N_3:H and at 1500 K for the remaining amorphous silicon-nitrogen alloys. An average of 200 sets from VASP's XDATCAR output file are inspected.
As done for the diffusion coefficient, prior to calculation of all alloys the cut-off energy's effect on the pair correlation function in the structure *a*-Si_3N_4 is evaluated using $E_{\text{cut}} = 120$ eV and $E_{\text{cut}} = 160$ eV. The results with $E_{\text{cut}} = 160$ eV are almost the same as with $E_{\text{cut}} = 120$ eV, which can be seen by comparing the panels in the top row of figure 5.8. The lower cut-off energy leads to virtually identical pair correlation functions. Thus $E_{\text{cut}} = 120$ eV is used in the remaining calculations.

From the first maximum in the partial pcf the average bond length is deduced. The bond lengths are in excellent agreement with reference values of other groups [7, 69]. The results of bond lengths as well as the selected cut-off radii of all inspected structures are given in table 5.4. The r_{cut} are used for calculating the bond angle distributions as well as the coordination numbers of the atoms in the discussion of their local environments.
The first inspected phase is amorphous silicon, *a*-Si, see the center left panel in figure 5.8. It shows the characteristic average Si-Si bond distance of 2.3 Å, as documented in references [7, 69]. A smaller, wider peak is located at 3.7 Å. With the trigonometric relation $a^2 = b^2 + c^2 - 2bc\cos\theta$ it is easily verified that, for $b = c = 2.3$ Å and the bond angle $\theta = 105°$ typical for tetrahedral coordination, this results in a second nearest neighbor distance of 3.7 Å for Si-Si in corner-sharing tetrahedral configurations. Thus the peak around 3.7 Å gives indication of the predominance of corner-sharing Si tetrahedra in amorphous silicon *a*-Si.
The introduction of nitrogen into the structure causes the appearance of the Si-N bond, as can be taken from the partial pcf of *a*-Si_3N_3 and *a*-Si_3N_4 in figure 5.8. The typical value of the Si-N bond length is 1.7 Å for the amorphous alloys, in excellent agreement with experimental findings from reference [8] and *ab-initio* results given in reference [7].

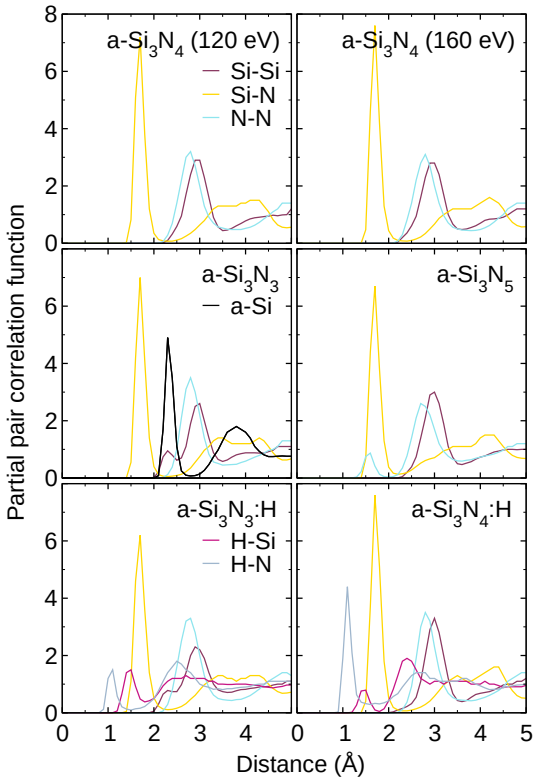

Figure 5.8: Partial pair correlation functions of the amorphous silicon-nitrogen alloys. The top row shows a comparison between amorphous stoichiometric silicon nitride a-Si_3N_4 with a cut-off energy E_{cut} of 120 eV and 160 eV. The center row gives the partial pcf of a-Si_3N_3, a-Si and a-Si_3N_5. The bottom row displays the hydrogenated alloys a-Si_3N_3:H and a-Si_3N_4:H, where in addition to the partial pcf for Si-Si, Si-N, and N-N those for H-Si and H-N are shown.

By applying the same reasoning as above, for Si-N bonds of about 1.7 Å an occurrence of Si-Si peaks at 2.9 Å with an angle of 117° for Si-N-Si units as well as N-N peaks at 2.7 Å with an angle of 105° for N-Si-N units is expected in corner-sharing SiN_4 tetrahedral configuration. These Si-Si and N-N peaks are indeed observed in the amorphous silicon-nitrogen alloys. In the alloys the Si-Si peak at 2.9 Å increases with increasing nitrogen content, while the Si-Si peak at 2.3 Å decreases. Where Si-Si distances of 2.3 Å are indicative of true Si-Si bonds and therefore of Si-Si pairs and Si-Si clusters in the amorphous silicon-nitrogen alloys, Si-Si peaks around 2.4 Å rather point to edge-sharing SiN_4 tetrahedra. Edge-sharing SiN_4 tetrahedra are obtained with an angle of approximately 90° for participating Si-N-Si as well as N-Si-N units and they result in twofold rings, specifically in quasi-planar squares with alternating Si and N atoms at the vertices. They have been experimentally found to be the dominant nitrogen pair defects in silicon [8]. Due to the similar values the Si-Si distances in edge-sharing SiN_4 tetrahedra are almost indistinguishable from true Si-Si bonds in the partial pair correlation function. Therefore the edge-sharing SiN_4 tetrahedra which constitute the square structures are further discussed with the other structural defects in chapter 5.1.5. The N-N nearest neighbor peaks occur at distances approximately 2.7 Å from the central atom in the substoichiometric silicon-nitrogen alloys and in stoichiometric silicon nitride, and are therefore indicative of the corner-sharing SiN_4 tetrahedral coordination. Merely in the

suprastoichiometric silicon-nitrogen alloy a-Si_3N_5, shown in the center right panel in figure 5.8, a true N-N bond is observed, which is located at 1.6 Å.

alloy	d_{Si-Si} (Å)	d_{Si-N} (Å)	d_{N-N} (Å)	d_{H-N} (Å)	d_{H-Si} (Å)
a-Si	2.3				
a-Si_3N	2.3	1.7	2.8		
a-Si_3N_2	2.3	1.7	2.8		
a-Si_3N_3	2.3	1.7	2.8		
a-Si_3N_4	2.9	1.7	2.8		
a-Si_3N_5	3.0	1.7	1.6		
a-Si_3N_3:H	2.3	1.7	2.8	1.1	1.5
a-Si_3N_4:H	3.0	1.7	2.8	1.1	1.5
a-Si_3N_4:NH_3	3.0	1.7	2.8	1.1	2.4
r_{cut} (Å)	2.6	2.1	1.8	1.3	1.8

Table 5.4: Average Si-N bond lengths d_{Si-N} as well as the other nearest neighbor distances d between atom types of amorphous silicon-nitrogen alloys. The cut-off radii r_{cut} are deduced from the partial pair correlation function of amorphous silicon-nitrogen alloys.

Hydrogenated phases are also inspected. The dominant Si-N bonds in the hydrogenated amorphous alloys show the same lengths as in the unhydrogenated silicon-nitrogen structures. The distances of H to N as well as H to Si are presented for the hydrogenated substoichiometric alloy a-Si_3N_3:H at the bottom left panel in figure 5.8. Clearly the Si-Si peak, located at 2.3 Å in a-Si_3N_3 and a-Si_3N_3:H, is lower in the hydrogenated than in the unhydrogenated phase, due to the bonding of hydrogen to silicon. Hydrogen thus cures some Si defects in this structure and reduces the tendency to form Si-Si pairs and Si-Si clusters. In a-Si_3N_3:H hydrogen is also found at distances of 1.1 Å from N atoms. The bottom right panel in figure 5.8 shows the distances of hydrogen to nitrogen and silicon in hydrogenated stoichiometric silicon nitride a-Si_3N_4:H. The hydrogen atoms in a-Si_3N_4:H are generally located approximately 1.1 Å from nitrogen neighbors and 1.5 Å from silicon atoms. This correlates with the fact that nitrogen has a smaller covalent radius than silicon. The results for a-Si_3N_4:NH_3 are similar, as can be seen in table 5.4. Hydrogen clearly is located closer to nitrogen atoms, the distance being 1.1 Å again, than to silicon, where the Si-H distance is 2.4 Å. Summed up, hydrogen bonds to nitrogen and silicon in the Si-rich alloy a-Si_3N_3:H, whereas in a-Si_3N_4:H and a-Si_3N_4:NH_3 hydrogen primarily bonds to nitrogen.

5.1.4 Bond angle distribution

In the amorphous silicon-nitrogen alloys the bond angles within the Si-N-Si and N-Si-N bonding units can be in a range of values. This results in a distribution of bond angles in contrast to the distinct bond angles in the crystalline phases. The bond angle distribution has an effect on the band gap of the structure [70]. Together with the previously determined bond lengths it facilitates an analysis of the short range order. The quenched-from-melt

structures of the VASP molecular dynamics simulation are used. As cut-off radii the values corresponding to each alloy from table 5.4 are used. By averaging over 200 sets, as performed in the previous chapter for the pair correlation function, the bond angle distribution becomes statistically more significant.

bonding unit	angle θ (°)
$Si-N-Si$	117
$N-Si-N$	105

Table 5.5: Average bond angle distribution of amorphous silicon nitride phases.

The bond angle distribution of amorphous silicon, devoid of nitrogen, has a peak at 105° and is illustrated in figure 5.9. All inspected amorphous silicon-nitrogen alloys show a very similar picture. This is independent of the stoichiometry of the phase and can easily be verified by comparing figures 5.9, 5.10 and 5.11. The maximum of the Si-N-Si bonding unit's distribution lies at 117° for all structures. The N-Si-N maximum is located at 105°, very close to the result for the pure silicon phase. The hydrogenated alloys exhibit a very similar bond angle distribution and are therefore not illustrated separately. The calculated average bond angles are given in table 5.5.

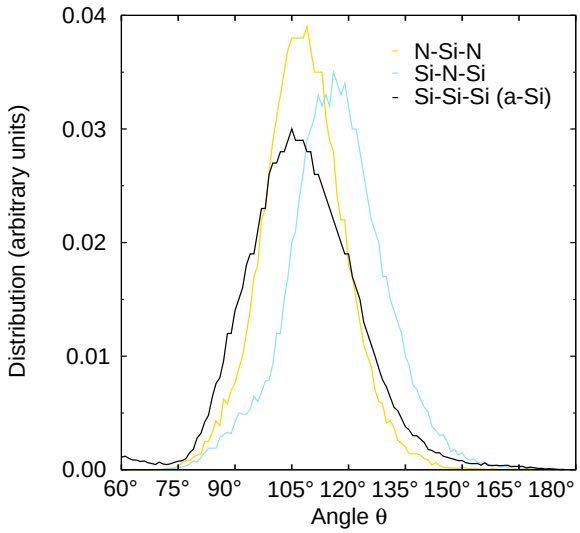

Figure 5.9: Bond angle distribution of the amorphous substoichiometric silicon-nitrogen alloy a-Si_3N_3 in an overlay plot with the bond angle distribution of amorphous silicon a-Si at 500 K.

These results lead to the conclusion that all amorphous silicon-nitrogen alloys consist mainly of SiN_4 tetrahedral units as well as NSi_3 triangular units. This has been reported extensively [7, 69, 71]. In off-stoichiometric alloys the majority atom type apparently functions as the bonding partner for silicon as well as nitrogen without significant change to the bond angle distribution. Aside from this a smaller peak or shoulder at 90° in the distribution of the Si-N-Si bonding unit is apparent in most alloys. It indicates the presence of twofold rings with alternating Si and N atoms, as discussed in the previous chapter and documented by reference [8].

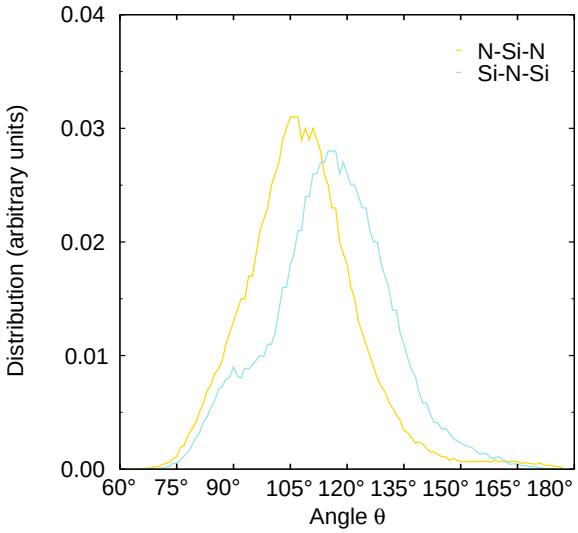

Figure 5.10: Bond angle distribution of amorphous stoichiometric silicon nitride a-Si_3N_4.

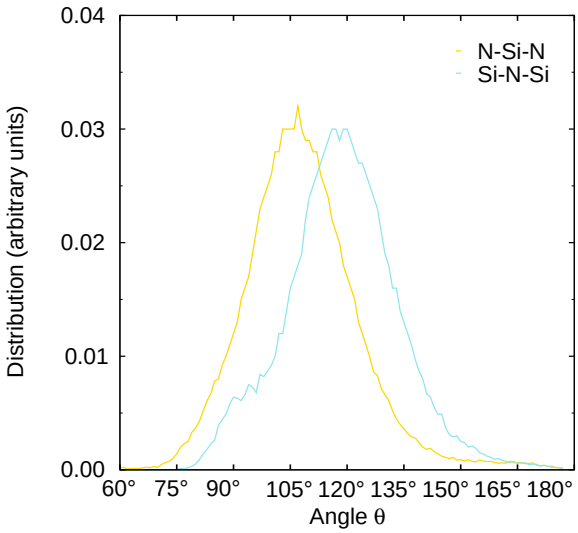

Figure 5.11: Bond angle distribution of the amorphous suprastoichiometric silicon-nitrogen alloy a-Si_3N_5.

5.1.5 Local environment

The coordination number of an atom describes how many nearest neighbors are present. This value changes significantly for different distances from the central atom. Thus the coordination number depends critically on the applied cut-off radius r_{cut}. Here the respective cut-off radii from table 5.4 in chapter 5.1.3 are used, after preliminary tests whether the selected r_{cut} leads to stable results. The focus is placed on a-Si_3N_3, a-Si_3N_4, and the respective hydrogenated alloys.

Figure 5.12: Silicon defects in the amorphous silicon-nitrogen alloys. (far left) 2-fold coordinated Si, (left) 3-fold coordinated Si, more specifically a K center, (right) 5-fold coordinated Si, (far right) a Si-Si unit or Si cluster with one Si-Si bond.

Two interesting aspects of the inspected phases can be obtained from this analysis. First there is the issue of structural defects, caused by under- and overcoordination. Structural defects are an indication what to expect concerning the electronic defects of these structures. The possible structural defects include 2-fold, 3-fold and 5-fold coordinated silicon atoms, the Si-Si unit as well as 2-fold and 4-fold coordinated nitrogen atoms [3]. 2-fold and 3-fold coordinated Si, illustrated in figure 5.12, as well as 2-fold coordinated N, in figure 5.13, are characterized by dangling bonds. A Si dangling bond, if it consists of a Si central atom with three N nearest neighbors, is called a K center. K centers cause gap states close to the middle of the band gap [72]. The N dangling bond, if it is a N atom bonded to two Si atoms, is denoted a N or N_2 center. N_2 centers lead to additional levels above the valence band maximum. Both types of dangling bonds are localized according to reference [73]. It is also possible that a threefold coordinated Si atom has one or more Si nearest neighbors instead of nitrogen and that a twofold N atom possesses other nitrogen nearest neighbors. In these cases the term dangling bond applies, but not the more specific terms K center or N_2 center, respectively.

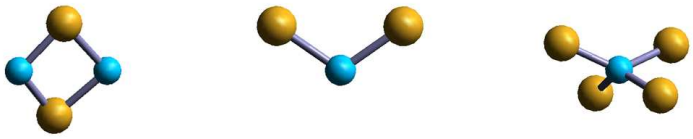

Figure 5.13: Square structure and nitrogen defects in the amorphous silicon-nitrogen alloys. (left) Square structure, four-membered ring, twofold ring or edge-sharing tetrahedra, (center) 2-fold coordinated N, more specifically a N center or N_2 center, (right) 4-fold coordinated N.

Figure 5.13 also illustrates 4-fold coordinated nitrogen and figure 5.12 shows 5-fold

coordinated silicon and a Si cluster with a Si-Si bond. 4-fold coordinated nitrogen and 5-fold coordinated silicon are called floating bonds. In reference [9] two more structural defects are proposed, in analogy to the defects in crystal structures. A N vacancy as well as a Si antisite is considered. The N vacancy is best described by a Si_3N_4 unit missing one N atom. This defect is considered in the present work through the analysis of threefold coordinated Si atoms. In the Si antisite, an additional Si atom fills the empty place of the N vacancy. The Si antisite can be regarded as a Si cluster of at least three neighboring Si atoms and is discussed in the present work by inspecting Si clusters. The findings in reference [9] are of most interest for electronic defects and their correlation to structural defects. In chapter 5.2.2 the PDoS of the amorphous silicon-nitrogen alloys are inspected and the consequences of structural defects for the respective electronic structure are interpreted. Another noteworthy structural defect is the so called square structure [4], four-membered ring or twofold ring [7]. It consists of a quasi-planar square with alternating Si and N atoms at the corners as shown in figure 5.13 and gives rise to what has been described as two edge-sharing tetrahedra, each with a Si central atom joined by two N atoms.
Secondly, through the analysis of Si-Si units it is possible to deduce whether silicon tends to form clusters or random percolation networks in non-stoichiometric silicon-nitrogen alloys obtained with the quenched-from-melt procedure, which are indicators of structural heterogeneity and phase separation. If, for instance, most silicon atoms feature at least one silicon nearest neighbor, this fact points to a tendency of clustering and if most silicon atoms have more than one silicon nearest neighbor it indicates the presence of random percolation networks. On the other hand, the more the amorphous network contains SiN_4 tetrahedra and triangular NSi_3 units, the less probable it is to observe Si clusters or even networks. The matter of hydrogen restoring this general structure is discussed as well. Experimental findings exist that do not indicate structural heterogeneity [6], but on the other hand reference [5] reports segregation of amorphous silicon-nitrogen alloys into Si clusters and SiN_4 units. Structural heterogeneity has been documented in previous VASP simulations for molten Si-rich oxides [74] as well as for the hydrogenated amorphous silicon-nitrogen alloy a-Si_3N_3:H [4].

Due to the relative low number of atoms in the applied super cells and the fast annealing compared to experiment, it is possible that the concentration of structural defects is overestimated. This issue has been previously researched [7]. For example, an approximate experimental concentration is given as 10^{17} cm^{-3} for twofold coordinated nitrogen. As there are about 10^{22} atoms/cm^3 it implies that at least 10^5 atoms are required in a super cell for realistic defect concentrations. Thus the discussion in this work is to be viewed as phenomenological and qualitative. By further optimizing the applied potentials as well as the implemented methods, larger super cells may be used, therefore future work is expected to deliver quantitative results as well.
The VASP calculations are performed in long MD simulations with 30000 steps, at 1 fs each. The liquid structures from the MDs at 3000 K are used. Gradually the temperature is decreased until solidification, from an initial value of 2800 K to 2500 K for a-Si_3N_3 and a-Si_3N_4. The long MD runs for the hydrogenated alloys are performed down to lower temperatures due to the higher diffusivity of hydrogen. Specifically, they are additionally carried out at 2250 K and 2000 K for a-Si_3N_3:H and at 1500 K for a-Si_3N_4:H. It is important to take into account that if the temperature is too high in the MD simulations and the structure is still liquid, the probability of observing phase separation in the quenched

structure diminishes. On the other hand, if the temperature is too low, then there is too little diffusion. Since diffusion facilitates the possibility of segregation, the temperatures are selected according to the results presented in table 5.3 of chapter 5.1.2. The cut-off radii are chosen as given in table 5.4 of chapter 5.1.3. After the long MD simulations a quenched MD run is conducted to ensure that the obtained structures represent the energetically most favourable configuration. The states are assigned to geometric defects by setting the INCAR-flag LORBIT = 10. Thus a PROCAR output file is written, which describes the spatial arrangement of electronic states. More localized states are viewed with the respective POSCAR atom number. From the OUTCAR output file the coordination of these atoms is obtained.

alloy (%)	$Si_{[2]}$	$Si_{[3]}$	$Si_{[4]}$	$Si_{[5]}$	$N_{[2]}$	$N_{[3]}$	$N_{[4]}$
a-Si_3N_4			99.0	1.0	2.3	94.5	3.1
a-Si_3N_4:H	1.1	9.2	83.9	5.7	0.9	87.9	11.2
a-Si_3N_3	1.0	6.3	82.3	10.4	1.0	94.8	4.2
a-Si_3N_3:H	1.0	8.3	74.0	16.7	1.0	90.6	8.3

Table 5.6: Percentage of coordination types occurring for Si and N atoms of amorphous silicon-nitrogen alloys in the quenched-from-melt structures. The total percentage of each element adds up to (100.0 ± 0.1) %, because of truncating effects. The index in brackets indicates the coordination number. Artificial Si bonds due to square structures are not included in the count.

alloy (%)	0 Si NN	1 Si NN	2 Si NN	3 Si NN	4 Si NN
a-Si_3N_4	100.0				
a-Si_3N_4:H	82.8	16.1	1.1		
a-Si_3N_3 expected[a]	31.6	42.2	21.1	4.7	0.4
a-Si_3N_3	42.7	29.2	19.8	4.2	4.2
a-Si_3N_3:H	52.1	26.0	9.4	7.3	5.2

[a]Estimate obtained with the binomial distribution for 4-fold coordinated silicon.

Table 5.7: Percentage of Si nearest neighbors (NN) of Si atoms in amorphous silicon-nitrogen alloys. The total percentage of each alloy adds up to (100.0 ± 0.1) %, because of truncating effects. All Si atoms with one or more Si NN form either Si clusters or a random percolation network. Artificial Si bonds due to square structures are not included in the count.

The results for the coordination numbers are given in table 5.6. No experimental findings of overcoordination defects are known to exist and they are likely to be calculation relics, therefore the interpretation of 5-fold coordinated silicon and 4-fold coordinated nitrogen is omitted. Concerning the matter of structural defects, the Si-rich alloy a-Si_3N_3, possesses far more undercoordinated N and Si atoms than the stoichiometric a-Si_3N_4. In amorphous silicon nitride a-Si_3N_4 only some defects are present. Specifically, slight concentrations

of 2-fold coordinated N are found. Both hydrogenated alloys display more coordination defects than the respective unhydrogenated structures, except for 2-fold coordinated N atoms in a-Si_3N_4:H. The hydrogenated amorphous silicon-nitrogen alloy a-Si_3N_3:H shows an increase by 2.0 % for threefold coordinated silicon compared to a-Si_3N_3. The the same number of undercoordinated N atoms are observed in a-Si_3N_3 and a-Si_3N_3:H. Amorphous silicon nitride initially contains no undercoordinated silicon, but hydrogenated silicon nitride a-Si_3N_4:H has 1.1 % and 9.2 % two- and threefold coordinated Si atoms. There are fewer twofold coordinated N atoms, by 1.4 %, in a-Si_3N_4:H. The square structure is observed in all inspected amorphous alloys in low concentrations. A precise count is not conducted, but approximate values around $5.0 - 10.0$ % are observed. Findings of reference [4] are in fair agreement.

Table 5.7 states the number of Si atoms that display zero, one or more Si nearest neighbor and the figures 5.14, 5.15, 5.16 and 5.17 give an illustration of the super cells for the interpretation regarding the possibility of structural heterogeneity in the quenched-from-melt structures.

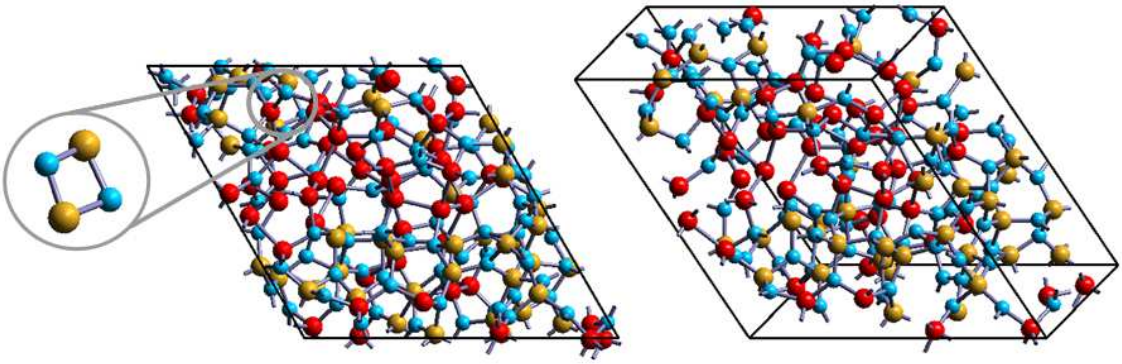

Figure 5.14: Super cell of a-Si_3N_3. Nitrogen is indicated by blue atoms, silicon with nitrogen neighbors by yellow atoms and silicon with one or more silicon nearest neighbor by red atoms. The Si atoms with Si nearest neighbors are found throughout the super cell and form a random percolation network, thus indicating structural heterogeneity. Additionally a square structure and its location in the super cell is illustrated.

In a-Si_3N_3 there is a strong indication of structural heterogeneity, because the super cell contains a random percolation network of silicon apart from the SiN_4 tetrahedra linked through nitrogen atoms. The super cell with the Si-Si network colored in red is shown in figure 5.14. By considering Si atoms with 2 or more Si nearest neighbors it is observed that at least 28.2 % of the Si atoms are part of the Si-Si network. In total, more than half of the silicon atoms display one or more Si nearest neighbors. No N-N bonds are present, due to the substoichiometric nitrogen content in a-Si_3N_3. For a rough estimate to compare these results to, the binomial distribution $P(k) = \binom{n}{k} p^k (1-p)^{n-k}$ for 4-fold coordinated Si gives, with $n = 4$ the total number of bonds per Si atom, $k = 0, 1, 2, 3, 4$ the number of Si-Si bonds on one Si atom and $p = 0.25$ the probability of Si-Si bonds, percentages of 31.6 %, 42.2 %, 21.1 %, 4.7 % and 0.4 % for Si atoms with 0, 1, 2, 3 or 4 Si nearest neighbors, respectively. It shows that the quenched-from-melt structure of a-Si_3N_3 contains more Si atoms without any Si nearest neighbors, fewer with one Si NN and slightly more silicon

atoms that are part of the Si-Si network than are expected from a binomial distribution.

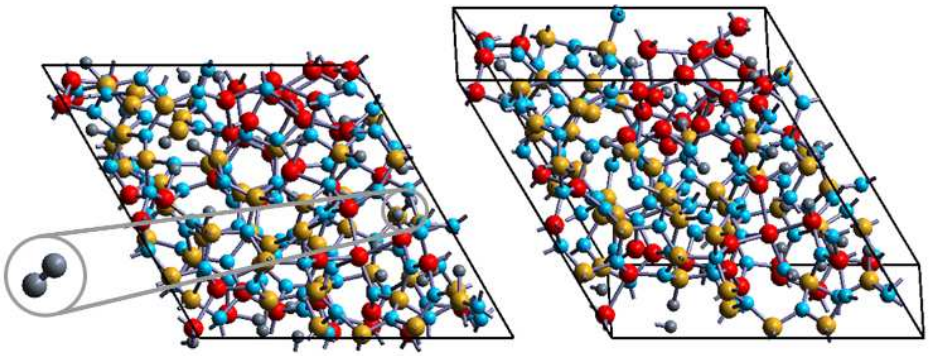

Figure 5.15: Super cell of a-Si_3N_3:H. Nitrogen is indicated by blue atoms, hydrogen by grey atoms, silicon with nitrogen neighbors by yellow atoms and silicon with one or more silicon nearest neighbor by red atoms. The Si atoms with Si nearest neighbors are observed throughout the super cell, albeit less than in the unhydrogenated alloy. This indicates curing of defects by hydrogen. Additionally a hydrogen dimer and its location in the super cell is shown.

The hydrogenated silicon-nitrogen alloy a-Si_3N_3:H also exhibits structural heterogeneity, but noticeably less than a-Si_3N_3. A region with a Si-Si network as well as SiN_4 tetrahedra linked through N atoms are again found in the super cell, as illustrated in figure 5.15. Just as with a-Si_3N_3, no N-N bonds are present in a-Si_3N_3:H. Hydrogen significantly bonds more to Si atoms than to N atoms, which can be explained with the substoichiometric nitrogen content. A single hydrogen dimer is observed in a-Si_3N_3:H, but not in a-Si_3N_4:H. The two H atoms are located 0.77 Å from each other, without any other nearest neighbors.

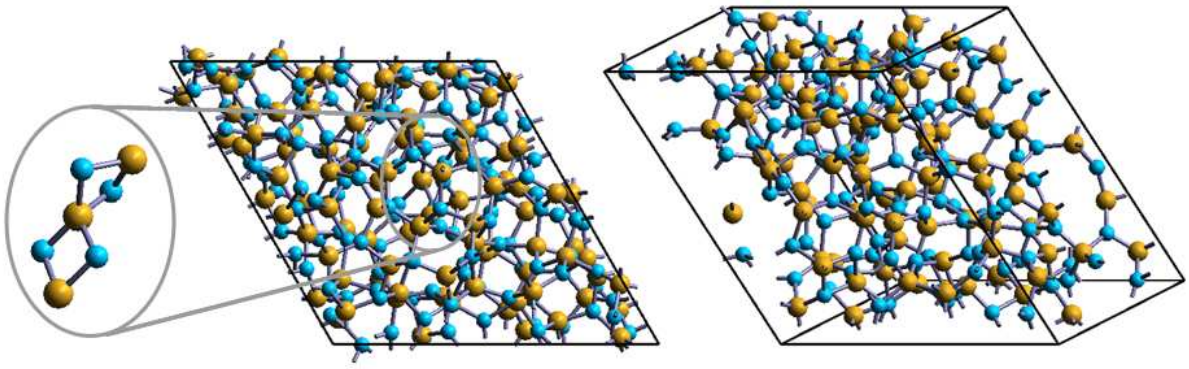

Figure 5.16: Super cell of a-Si_3N_4. Nitrogen is indicated by blue atoms and silicon with nitrogen neighbors by yellow atoms. No Si-Si bonds are observed. Additionally two adjoining square structures and their location in the super cell are depicted.

No indication of structural heterogeneity or phase separation is found in quenched-from-melt a-Si_3N_4, because only Si-N bonds are present in this stoichiometric structure. This finding, illustrated in figure 5.16, is given through the absence of any Si nearest neighbors of silicon central atoms. It can be also verified in table 5.7.

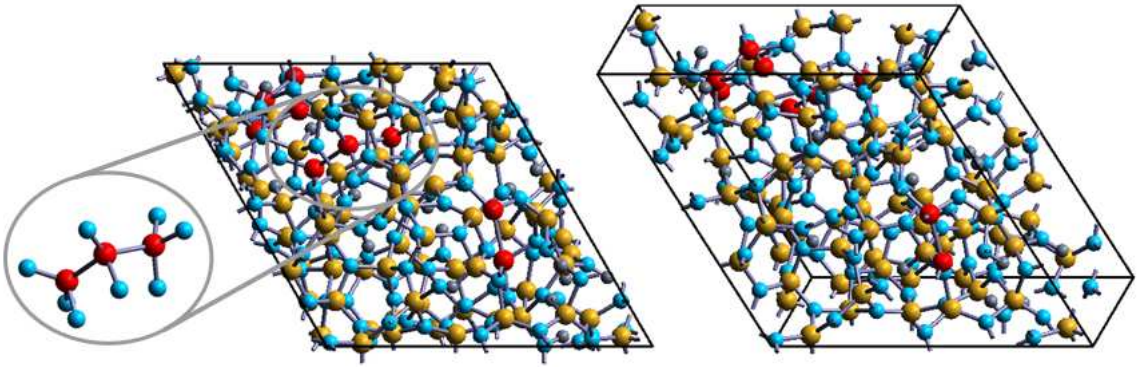

Figure 5.17: Super cell of a-Si_3N_4:H. Nitrogen is indicated by blue atoms, hydrogen by grey atoms, silicon with nitrogen neighbors by yellow atoms and silicon with one or more silicon nearest neighbor by red atoms. Some Si-Si bonds are observed. Additionally three neighboring Si atoms and their location in the super cell are shown.

In a-Si_3N_4:H randomly some Si-Si neighbors are introduced, see figure 5.17. Therefore a few Si clusters are present, more than in a-Si_3N_4, where there are no such clusters, but significantly less than in a-Si_3N_3 or a-Si_3N_3:H. Hydrogen tends to bond to N atoms, which is the opposite as in a-Si_3N_3:H. Nitrogen is more electronegative than silicon, thus if enough nitrogen is available for bonding hydrogen prefers nitrogen [75]. This is the case in a-Si_3N_4:H. Because of this, some silicon atoms do not have sufficient nitrogen nearest neighbors, leaving them either undercoordinated or prone to bond to other silicon atoms. It can be concluded that hydrogen leads to the occurrence of Si-Si neighbors in the quenched-from-melt structure of amorphous silicon nitride a-Si_3N_4, whereas in the Si-rich silicon-nitrogen alloy a-Si_3N_3 hydrogen restores the regular configuration of SiN_4 tetrahedra and mostly planar NSi_3 triangles.

5.2 Electronic properties

The electronic properties of amorphous silicon nitride a-Si_3N_4 and silicon-nitrogen alloys a-Si_3N_3, a-Si_3N_3:H and a-Si_3N_4:H are determined. A calculation of the density of states is performed, in order to obtain characteristics of valence bands, conduction bands as well as Kohn-Sham PBE band gaps. The partial density of states is interpreted as well, with focus on the electronic levels of possible structural defects and on random percolation networks of silicon nearest neighbors.

5.2.1 Density of states

The density of states (DoS) in a-Si_3N_3, a-Si_3N_4, a-Si_3N_3:H and a-Si_3N_4:H are inspected. Information regarding the valence and conduction bandwidths as well as the fundamental band gap are derived and compared to available reference values. For the purpose of determining the fundamental band gaps of the amorphous silicon-nitrogen alloys the energy levels of the valence electrons in the quenched-from-melt structures are considered as crystal orbitals [57]. The KS PBE band gap between highest occupied crystal orbital (HOCO) and lowest unoccupied crystal orbital (LUCO) is determined. Since the electronic structure of crystalline silicon nitride is controlled by the short-range order, it is expected that the amorphous alloys show a nearly identical DoS, as suggested by reference [59]. Furthermore, due to the amorphous nature of the systems and thus to the possibility of coordination defects, impurity states within the gap as well as tailing of bands into the gap are expected. A general problem in DFT is deciding where to exactly place the VB maximum and CB minimum, and further whether a certain level is considered as a defect level or as the top of the band. In the present work the VB maximum is the highest level with full occupation as derived by VASP, and the CB minimum is the lowest level with zero occupation. All levels between these two are considered as defect levels.

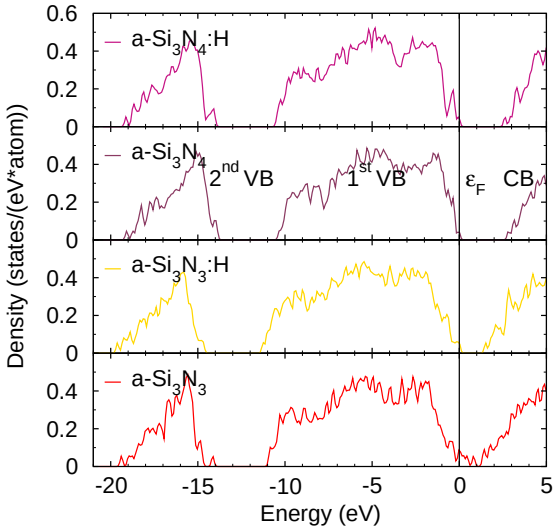

Figure 5.18: Density of states (DoS) of the amorphous silicon-nitrogen alloy a-Si_3N_3 and amorphous silicon nitride a-Si_3N_4, as well as of hydrogenated a-Si_3N_3:H and a-Si_3N_4:H.

In the VASP calculations, the solidified structures from the long MD simulations with 30 ps at 1500 K are applied. A quenched MD run then relaxes the structure into the energetically most favourable configuration. For the quenched MD the flag LORBIT=10 is set in the INCAR file for output of the DOSCAR file, which contains information about the density of states.
In figure 5.18 the density of states (DoS) of the inspected alloys are shown. The Γ-point of the Brillouin zone is inspected, as there are no distinct symmetry points in amorphous structures. The DoS are divided by the number of Si and N atoms in the respective unit cell to facilitate comparison. The Fermi level in the plots is set to 0.0 eV and represents the highest fully occupied energy level.

	a-Si_3N_3			a-Si_3N_4		
property (eV)	exp. [a]	ref. [b]	present work	exp. [c]	ref. [d]	present work
E_g min.	2.6	2.4	1.43	3.85[e], 4.55	4.5, 5.3[f]	2.79
bottom 1st VB	-12.2	-14.2	-10.82	-12.2	-11.8	-10.36
top 2nd VB	-14.4	-17.0	-14.18	-14.3	-16.6	-14.00
bottom 2nd VB	-21.1	-21.4	-19.46	-21.4	-19.9	-19.15
width 1st VB	12.2	14.2	10.82	12.2	11.8	10.36
width 2nd VB	6.7	4.4	5.28	7.1	3.3	5.15
full width VB	21.1	21.4	19.46	21.4	19.9	19.15

[a] PES and XPS data from reference [76].
[b] Tight-binding data from reference [57].
[c] Optical absorption data from reference [77] for E_g min. PES and XPS data from reference [76].
[d] Tight-binding data from reference [78].
[e] Photoemission data from reference [79].
[f] Tight-binding data from reference [57].

Table 5.8: Kohn-Sham PBE band gap E_g and the VB widths of the amorphous silicon-nitrogen alloy a-Si_3N_3 and of amorphous silicon nitride a-Si_3N_4. The Γ-point of the Brillouin zone is inspected.

In tables 5.8 and 5.9 the results concerning conduction band (CB), Kohn-Sham PBE band gap E_g and valence band (VB) are given. The values, albeit slightly lower, are in reasonable agreement with results from *ab-initio* methods [4, 57, 78, 80] and from experimental findings [6, 76, 77, 79, 81]. As in the crystalline polymorphs of silicon nitride the VB in general consists of two parts, the upper or 1st VB and the lower or 2nd VB, separated by a gap. In unhydrogenated and hydrogenated a-Si_3N_3 and a-Si_3N_4 the full VB width ranges between 19.2 eV and 19.7 eV. The lower VB exhibits widths between 4.9 eV and 5.3 eV. The separating gap is around $3.4 - 3.8$ eV and the upper VB width is between 10.3 eV and 11.2 eV. In the Si-rich a-Si_3N_3 the KS PBE band gap E_g between the VB maximum and the conduction band (CB) minimum is 1.43 eV, with defect levels located within the gap. The KS PBE band gap E_g of the hydrogenated amorphous silicon-nitrogen alloy a-Si_3N_3:H is 1.52 eV, also with defect levels in the gap. Amorphous silicon nitride a-Si_3N_4 has a KS PBE band gap E_g of 2.79 eV, and in a-Si_3N_4:H the KS PBE band gap E_g is 2.61 eV. In unhydrogenated as well as hydrogenated amorphous silicon nitride no defect levels are observed in the KS PBE band gap.

property (eV)	a-Si_3N_3:H exp. [a]	a-Si_3N_3:H ref. [b]	a-Si_3N_3:H present work	a-Si_3N_4:H exp. [c, d]	a-Si_3N_4:H present work
E_g min.	2.6, 3.2[e]	1.7, 2.2	1.52	5.1[f], 5.5	2.61
bottom 1st VB	-11.5	-10.0, -11.0	-11.23	-11.7	-10.32
top 2nd VB	-13.3	-14.5, -15.5	-14.73	-13.8	-14.09
bottom 2nd VB		-18.5, -19.5	-19.65	-21.2	-19.15
width 1st VB	11.5	10.0, 11.0	11.23	11.7	10.32
width 2nd VB		4.0, 4.5	4.92	7.4	5.06
full width VB		18.5, 19.5	19.65	21.2	19.15

[a] Optical absorption data from reference [81] for E_g min. PES and XPS data from reference [76].
[b] *Ab-initio* data from reference [4]. The first value is of the low density alloy, 2 g/cm^3, whereas the second value is of the high density alloy, 3 g/cm^3.
[c] Optical absorption data from reference [81] for E_g min. XPS data from reference [80] of a-SiN_x:H, $x = 1.4$.
[d] No *ab-initio* data on band gap or bandwidths known to the author at the time of research, thus the column is omitted.
[e] Optical absorption data from reference [6].
[f] Optical absorption data from reference [6].

Table 5.9: Kohn-Sham PBE band gap E_g and the VB widths of the hydrogenated amorphous silicon-nitrogen alloy a-Si_3N_3:H and of hydrogenated amorphous silicon nitride a-Si_3N_4:H. The Γ-point of the Brillouin zone is inspected.

The amorphous silicon-nitrogen alloy a-Si_3N_3 and amorphous silicon nitride a-Si_3N_4 have a similar VB. A difference is that in a-Si_3N_3 both the upper and lower VB are slightly wider and thus shifted towards lower energies, by $0.2 - 0.5$ eV. Additionally the bands exhibit tails that reach into the gaps. The tailing indicates undercoordination and overcoordination and will be discussed further in the context of partial DoS, see chapter 5.2.2. Another noteworthy difference is the smaller Kohn-Sham PBE band gap of a-Si_3N_3 compared to the stoichiometric a-Si_3N_4. The general band gap underestimation of the applied method, as noted previously in chapter 3.3.1, is an issue to be addressed in further work, for example by implementation of other functionals. In amorphous silicon-nitrogen alloys with a Si random percolation network a small optical gap around 2.0 eV is found experimentally [82]. For DFT calculations this indicates an even smaller Kohn-Sham PBE band gap in such structures, in line with the present results.
Regarding the curing effect of hydrogenation, it is observed that the unhydrogenated amorphous silicon-nitrogen alloy a-Si_3N_3 has more electronic states in the KS PBE band gap, because the E_g of hydrogenated amorphous silicon-nitrogen alloy a-Si_3N_3:H is larger and shows less tailing into the KS PBE band gap as well as VB gap. This effect is not reproduced in a-Si_3N_4:H, as the addition of hydrogen to stoichiometric amorphous silicon nitride a-Si_3N_4 adds valence electrons. Thus the KS PBE band gap E_g even shows a slight decrease from a-Si_3N_4 to a-Si_3N_4:H. Nevertheless, the KS PBE band gap of a-Si_3N_4:H is larger than of a-Si_3N_3:H. It is concluded that of relevance to the KS PBE band gap in amorphous silicon-nitrogen alloys is foremost stoichiometry of the structure and secondly the curing of defects through hydrogen in Si-rich alloys.

5.2.2 Partial density of states

The orbital-resolved partial density of states (PDoS) in *a*-Si_3N_3, *a*-Si_3N_4, *a*-Si_3N_3:H and *a*-Si_3N_4:H are presented for determining the electronic contributions to the valence band (VB) and conduction band (CB). Then levels at the edge of the band gap or within the gap are inspected to deduce the corresponding electronic defects. Electronic defects are often closely associated with structural defects, because under- or overcoordination commonly results in states located at mid gap or at the band edges.
For instance, the potential of twofold coordinated nitrogen atoms is more negative or repulsive than of their threefold coordinated counterparts. Similarly, threefold coordinated silicon atoms display a more positive or attractive potential than fourfold coordinated silicon. The wrongly coordinated atoms have an effect on the PDoS. Undercoordination of silicon leads to an additional level in the silicon PDoS, lower in energy than the ideal DoS of the conduction band. Undercoordination of nitrogen on the other hand adds a level to the nitrogen PDoS of the valence band which is higher in energy [3]. The levels associated with Si-Si bonds lie in the gap just above the VB maximum. In reference [9] an electronic defect is presented in the form of the DoS of a so called Si antisite. The Si antisite is if one N atom of the Si_3N_4 unit is replaced by a Si atom. It reportedly leads to a fully occupied gap level and a single electron below the conduction band minimum. The Si antisite can be viewed as a description of the Si network or a Si cluster with Si-Si bonds. Thus, for large super cells the band gap is expected to shrink in structures where there are more Si clusters or a Si random percolation network present, due to the accumulation of defect levels in the gap [82].

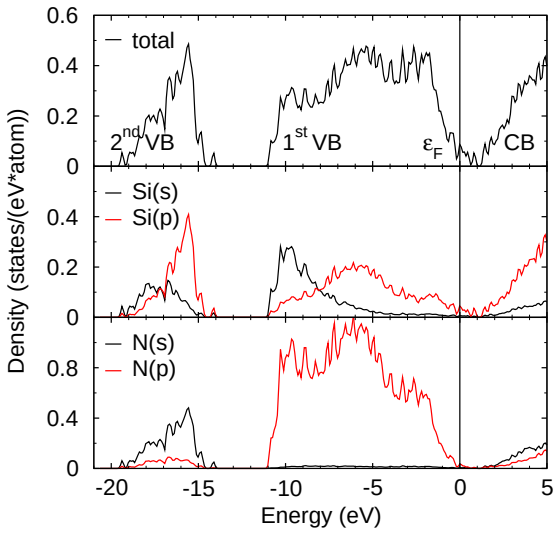

Figure 5.19: Orbital-resolved partial density of states (PDoS) of the amorphous silicon-nitrogen alloy *a*-Si_3N_3.

The results of two different VASP calculations are interpreted. First the quenched-from-melt structures from chapter 5.2.1 are applied for obtaining the orbital-resolved partial density of states (PDoS). In the quenched MD simulation the flag LORBIT=10 is set in the INCAR file to obtain the required information. The Γ-point of the Brillouin zone is inspected. For comparison the PDoS are divided by the number of Si and N atoms in the respective unit cell. The highest fully occupied energy level is located at 0.0 eV.
Secondly, for observing electronic defects the quenched-from-melt structures from chap-

ter 5.1.5 are used.

Figures 5.19, 5.20, 5.21 and 5.22 display the orbital-resolved partial DoS of a-Si_3N_3, a-Si_3N_4, a-Si_3N_3:H and a-Si_3N_4:H, respectively. In amorphous silicon nitride a-Si_3N_4 and in the amorphous silicon-nitrogen alloy a-Si_3N_3 a high degree of hybridization occurs. Much as in the crystalline phases of Si_3N_4 the Si valence electrons form sp^3 hybrid orbitals and nitrogen shows sp^2 hybridization as well as a non-bonding lone pair of N ($2p$) electrons. The hybrid orbitals from both atomic species make up the σ and σ^* orbitals of the amorphous silicon-nitrogen alloys including a-Si_3N_4 and the non-bonding N ($2p$) electrons form π orbitals [57].

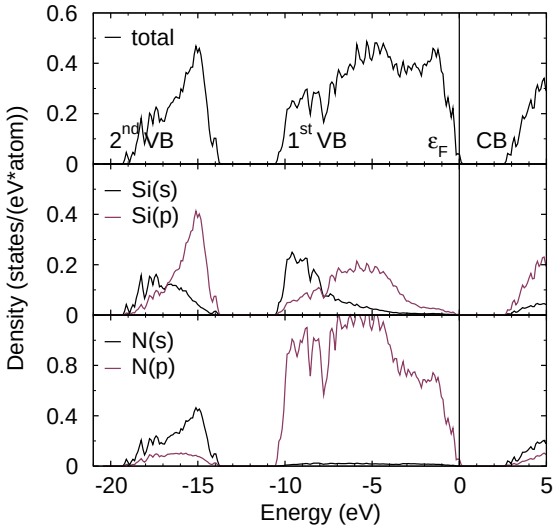

Figure 5.20: Orbital-resolved partial density of states (PDoS) of the amorphous silicon-nitrogen alloy a-Si_3N_4.

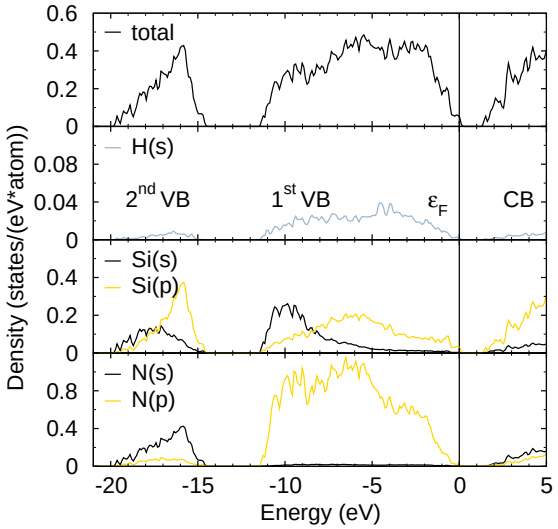

Figure 5.21: Orbital-resolved partial density of states (PDoS) of the amorphous silicon-nitrogen alloy a-Si_3N_3:H.

The lower valence band (VB) mostly contains contributions from N ($2s$) and Si ($3s$) electrons at deeper levels and from N ($2s$) and Si ($3p$) electrons at higher energies. The upper VB shows indication of the characteristic three peak structure, as discussed in chapter 3.3.2. Contributions to the peak at deep levels arise mainly from N ($2p$) and Si ($3s$) electrons. The middle peak is from N ($2p$) and Si ($3p$) electrons and the peak closest to the Fermi level predominantly originates from N ($2p$) electrons.

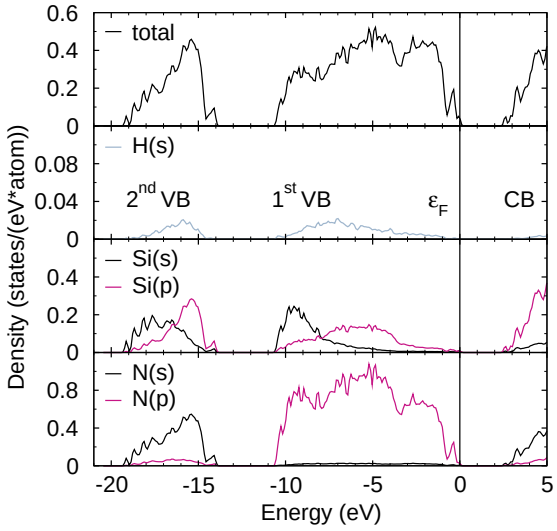

Figure 5.22: Orbital-resolved partial density of states (PDoS) of the amorphous silicon-nitrogen alloy a-Si_3N_4:H.

In the Si-rich alloy a-Si_3N_3, due to the substoichiometric nitrogen content, some valence electrons deviate from the octet rule. This causes N ($2p$) electrons to recede from the Kohn-Sham PBE band gap E_g with Si ($3p$) electrons filling part of the levels as well as significant tailing of all electronic contributions into the KS PBE band gap. Tailing is also observed in hydrogenated a-Si_3N_3:H. The H ($1s$) electrons in a-Si_3N_3:H are mainly found in the upper VB and most likely originate from Si-H bonds, whereas in a-Si_3N_4:H they occur in the higher levels of the lower VB as well as in the upper VB, where they indicate N-H bonds and Si-H bonds, respectively.

To deduce the nature of the highest occupied crystal orbital (HOCO), the lowest unoccupied crystal orbital (LUCO) and the gap states in a-Si_3N_3 and a-Si_3N_3:H as well as the HOCO and LUCO in a-Si_3N_4 and a-Si_3N_4 an analysis of localizations of electrons is performed with the quenched-from-melt structures from chapter 5.1.5. The results are presented in tables 5.10, 5.11, 5.12 and 5.13.
The HOCO in a-Si_3N_3 mainly consists of Si ($3p$) electrons that are part of the Si-Si network. The localization of electrons at the HOCO is less than the localizations at defect levels. The first defect level or gap state shows a localization of Si ($3p$) electrons of a fourfold coordinated silicon atom that has one Si nearest neighbor atom (NN). The nitrogen nearest neighbor atoms of the silicon atom display localized N ($2p$) electrons at this level. To the second gap state above the HOCO in a-Si_3N_3 mainly a twofold and a threefold coordinated silicon atom, hence both undercoordinated, contribute to the level with Si ($3s$) electrons and a twofold coordinated nitrogen atom adds N ($2p$) electrons. The third defect level is dominated by localizations of Si ($3p$) and Si ($3p$) electrons. These Si atoms constitute

part of the Si-Si network and one Si atom in close proximity is threefold coordinated. The next higher defect level also consists mainly of Si ($3s$) and Si ($3p$) electrons of Si atoms in the Si-Si network with a slight contribution from a threefold coordinated Si. Additionally an undercoordinated N atom shows localization of N ($2p$) electrons at this level. The fifth defect level above the HOCO arises mostly from Si ($3s$) and Si ($3p$) electrons within the Si-Si network. A contribution from a threefold coordinated Si atom is observed. The LUCO in a-Si_3N_3 mainly displays a localization of Si ($3p$) electrons from the Si-Si network. The results for a-Si_3N_3 are in general agreement with reference [72], which states that Si dangling bonds give rise to levels near the middle of the gap and N dangling bonds create levels slightly above the VB edge.

a-Si_3N_3	gap state	contribution	description
LUCO		Si ($3p$)	Si-Si network: $Si_{[3]}$, $Si_{[4]}$
	5	Si ($3s$), ($3p$)	Si-Si network: $Si_{[3]}$, $Si_{[4]}$
	4	Si ($3s$), ($3p$)	Si-Si network: $Si_{[3]}$, $Si_{[4]}$
		N ($2p$)	$N_{[2]}$ (N_2 center)
	3	Si ($3s$), ($3p$)	Si-Si network: $Si_{[3]}$, $Si_{[4]}$
	2	Si ($3p$)	$Si_{[2]}$, $Si_{[3]}$ (K center)
		N ($2p$)	$N_{[2]}$ (N_2 center)
	1	Si ($3s$), ($3p$)	$Si_{[4]}$
		N ($2p$)	$N_{[3]}$
HOCO		Si ($3p$)	Si-Si network: $Si_{[4]}$
		N ($2p$)	$N_{[3]}$

Table 5.10: HOCO, LUCO and gap states in the amorphous silicon-nitrogen alloy a-Si_3N_3. The column labelled "contribution" describes which electrons show a high localization and the last column states which atoms participate in the forming of the levels.

a-Si_3N_3:H	gap state	contribution	description
LUCO		Si ($3s$), ($3p$)	Si-Si cluster: $Si_{[4]}$
	5	Si ($3p$)	$Si_{[2]}$, $Si_{[3]}$ with 1H NN
	4	Si ($3p$)	$Si_{[2]}$, $Si_{[3]}$ with 1H NN
	3	Si ($3p$)	Si-Si network: $Si_{[4]}$
		N ($2p$)	$N_{[2]}$ (N_2 center)
	2	Si ($3s$), ($3p$)	Si-Si network: $Si_{[4]}$
	1	Si ($3s$), ($3p$)	Si-Si network with 1H NN: $Si_{[4]}$
HOCO		Si ($3p$)	Si-Si network with 1H NN: $Si_{[4]}$

Table 5.11: HOCO, LUCO and gap states in the hydrogenated amorphous silicon-nitrogen alloy a-Si_3N_3:H. The column labelled "contribution" describes which electrons show a high localization and the last column states which atoms participate in the forming of the levels. NN is the abbreviation for nearest neighbor atom.

The hydrogenated amorphous silicon-nitrogen alloy a-Si_3N_3:H has a HOCO that shows a

localization of Si ($2p$) electrons originating from Si atoms within the Si-Si network that partially have hydrogen nearest neighbors. The first three defect levels above the HOCO lie very close to each other and share noteworthy characteristics. They mostly contain contributions from Si ($3p$) electrons and to a lesser extent from Si ($3s$) electrons, both of Si atoms that constitute the Si-Si network. The first defect level displays Si atoms which have hydrogen nearest neighbor. The third defect level above the HOCO additionally consists of localizations of N ($2p$) electrons from a twofold coordinated N atom. The fourth and fifth defect level above the HOCO mainly arise from Si ($3p$) electrons belonging to twofold and threefold coordinated Si atoms. The LUCO is found to contain contributions from Si ($3s$) and Si ($3p$) electrons of a Si-Si cluster.

a-Si_3N_4	state	contribution	description
	+1	Si ($3s$)	$Si_{[5]}$
LUCO		Si ($3p$)	$Si_{[3]}$ (K center)
HOCO		N ($2p$)	$N_{[2]}$ (N_2 center)
	-1	N ($2p$)	$N_{[2]}$ (N_2 center)

Table 5.12: HOCO, LUCO and states directly above the LUCO and below the HOCO in amorphous silicon nitride a-Si_3N_4. The column labelled "contribution" describes which electrons show a high localization and the last column states which atoms participate in the forming of the levels.

a-Si_3N_4:H	state	contribution	description
	+1	Si ($3s$), ($3p$)	$Si_{[3]}$ with 1H NN
		N ($2s$), ($2p$)	$N_{[2]}$ (N_2 center)
LUCO		Si ($3s$), ($3p$)	Si-Si cluster: $Si_{[3]}$, $Si_{[4]}$
		N ($2s$), ($2p$)	$N_{[3]}$
HOCO		Si ($3s$), ($3p$)	Si-Si unit: $Si_{[4]}$
		N ($2p$)	$N_{[3]}$ with 1H NN
	-1	Si ($3s$), ($3p$)	Si-Si unit: $Si_{[4]}$
		N ($2p$)	$N_{[3]}$ with 1H NN
		N ($2p$)	$N_{[2]}$ (N_2 center)

Table 5.13: HOCO, LUCO and states directly above the LUCO and below the HOCO in hydrogenated amorphous silicon nitride a-Si_3N_4:H. The column labelled "contribution" describes which electrons show a high localization and the last column states which atoms participate in the forming of the levels. NN is the abbreviation for nearest neighbor atom.

In amorphous silicon-nitride a-Si_3N_4 a defect free Kohn-Sham PBE band gap E_g is observed. The HOCO, as well as the occupied level 0.40 eV below, displays a localization of N ($2p$) electrons from a N-center or twofold coordinated nitrogen atom. The LUCO is located 1.52 eV above the HOCO at a temperature and contains contributions mainly from localizations of Si ($3p$) electrons from a K-center or threefold coordinated Si atom backbonded to three N atoms. The level above the LUCO exhibits localized Si($3s$)

electrons from a fivefold coordinated silicon atom.
The HOCO of a-Si_3N_4:H shows a localization of Si ($3s$) and Si ($3p$) electrons from a Si dimer and of N ($2p$) electrons from a threefold coordinated N atom with one hydrogen nearest neighbor atom. The LUCO mostly consists of electronic Si ($3s$) an Si ($3p$) contributions from three Si atoms, threefold and fourfold coordinated, bonded to one another and of N ($2s$) and N ($2p$) electrons from a threefold coordinated nitrogen adjacent to the threefold coordinated Si atom.

We find that twofold coordinated nitrogen N ($2p$) electrons dominate the HOCO in a-Si_3N_4, whereas in a-Si_3N_3 N ($2p$) and Si ($3p$) electrons are present. The gap states in a-Si_3N_3 are mostly from Si atoms within the Si random percolation network. The hydrogenated amorphous alloy a-Si_3N_3:H incidentally has the same number of defect states as a-Si_3N_3. The contributions to defect states in a-Si_3N_3:H mainly arise from Si atoms that belong to the Si-Si network, as in a-Si_3N_3. Hydrogen nearest neighbors to Si atoms with localized electrons are found in three defect levels as well as in the HOCO. In a-Si_3N_3:H hydrogen bonds to nitrogen and silicon. Hydrogenated a-Si_3N_4:H exhibits Si-Si nearest neighbors not observed in stoichiometric a-Si_3N_4. Hydrogen atoms are localized at the HOCO and immediately below, but are bonded predominantly to nitrogen atoms.
The localization of electrons from wrongly coordinated atoms depends on the degree of hybridization of these atoms. The more hybridization occurs the less localized the valence electrons are. The hydrogenated alloys show significantly less localization of electronic defects with energies close to the band gap as given by VASP, almost by an order of magnitude at HOCO and LUCO. This indicates that the addition of hydrogen to a-Si_3N_3 or a-Si_3N_4 facilitates hybridization of orbitals.

Chapter 6

Conclusions

In chapter 3 the structural, electronic, optical and vibrational properties of crystalline silicon nitride are presented. The VASP calculations are performed with the regular potential POTCAR.SiN (cut-off energy $E_{\text{cut}} = 400$ eV). A convergence of energy is obtained with a $4 \times 4 \times 4$ **k**-point mesh for α-Si_3N_4, with a $4 \times 4 \times 8$ **k**-point mesh for β-Si_3N_4 and with a $6 \times 6 \times 6$ mesh for γ-Si_3N_4.
By comparison of ground state energies E_0 it is confirmed that β-Si_3N_4 is the stable polymorph of crystalline silicon nitride, while α-Si_3N_4 is a metastable phase. The high pressure phase γ-Si_3N_4 exhibits a significantly higher energy than α-Si_3N_4 and β-Si_3N_4, indicating that it does not form in standard conditions. The space group of α-Si_3N_4 is $P31c$. The hexagonal unit cell contains 28 atoms, with lattice constants $a_0 = 7.81$ Å and $c_0 = 5.66$ Å. The ratio c/a in α-Si_3N_4 therefore is determined as 0.727 and the equilibrium volume as $V_0 = 74.70$ Å^3 per formula unit. In α-Si_3N_4 a bulk modulus $B_0 = 220$ GPa is obtained. For β-Si_3N_4 space group $P6_3$ is ruled out and $P6_3m$ is established as the correct space group. The unit cell of β-Si_3N_4 is hexagonal with 14 atoms. Lattice constants $a_0 = 7.66$ Å and $c_0 = 2.92$ Å of β-Si_3N_4 result in a ratio $c/a = 0.382$ as well as in an equilibrium volume $V_0 = 74.33$ Å^3 per formula unit. The bulk modulus in β-Si_3N_4 is calculated to be $B_0 = 234$ GPa. A significant difference between the elastic constants C_{11} and C_{33} is observed, indicating a high degree of elastic anisotropy in β-Si_3N_4. γ-Si_3N_4 has the inverse spinel structure, thus octahedrally coordinated Si atoms are present, in addition to tetrahedrally coordinated Si atoms. The space group of γ-Si_3N_4 is $Fd\overline{3}m$ and the primitive fcc unit cell contains 14 atoms. The fcc unit cell has a lattice constant $a_0 = 7.7839$ Å and the equilibrium volume is $V_0 = 58.96$ Å^3 per formula unit. The bulk modulus in γ-Si_3N_4 is determined as $B_0 = 292$ GPa. The transition pressure of α-Si_3N_4 and β-Si_3N_4 to γ-Si_3N_4 are established as $p_t^{\alpha\to\gamma} = 10.7$ GPa and $p_t^{\beta\to\gamma} = 11.0$ GPa.
The chemical bonds in the crystalline polymorphs of Si_3N_4 are found to be sp^3 hybrid orbitals of Si atoms and sp^2 hybrid orbitals of N atoms. A pair of N ($2p$) electrons does not participate in bonding but forms a non-bonding π orbital. The electronic band structures of the three crystalline phases exhibit similar characteristics. Two wide valence bands (VB) are separated by a gap of 2.8-4.8 eV in the DFT calculations. The lower VB, 3.8-5.5 eV, is found to be dominated by N ($2s$) electrons. The upper VB consists of three peaks, with a total width of 9.7-10.9 eV. The lowest peak in the upper VB originates from N ($2p$) and Si ($3s$) hybrid orbitals. The center peak mostly consists of N ($2p$) as well as Si ($3p$) electrons. The highest peak in the upper VB, which is separated by a deep dip at -2.5 eV from the center peak, mainly contains non-bonding N ($2p$) electrons. Flat bands for the VB are observed due to the delocalized nature of the non-bonding N ($2p$) electrons. The minimal Kohn-Sham PBE band gaps E_g are indirect interband thresholds in the three crystalline polymorphs of Si_3N_4. It is determined that α-Si_3N_4 has the largest KS PBE band gap E_g, 4.65 eV, followed by 4.25 eV in β-Si_3N_4 and 3.34 eV in γ-Si_3N_4. The anti-bonding octahedrally coordinated Si^{oct} ($3s$) states and the anti-bonding tetrahedrally coordinated Si^{tetr} ($3p$) states in the conduction band (CB) of γ-Si_3N_4, which are significantly lower in energy than the Si^{tetr} ($3s$) and the Si^{oct} ($3p$), respectively, result in the smaller KS PBE band gap of the γ-phase compared to α-Si_3N_4 and β-Si_3N_4.

As an approximation to the macroscopic dielectric tensor the static dielectric tensor with and without local field effects is calculated using density functional theory. The results obtained for the static dielectric tensor including local field effects are slightly lower than the values excluding local field effects. In α-Si_3N_4 the static dielectric constant perpendicular to the c-axis, $\varepsilon^{\text{static}}(\perp)$, is larger than $\varepsilon^{\text{static}}$ ($\parallel$), whereas in β-Si_3N_4 the static dielectric constant parallel to the c-axis, $\varepsilon^{\text{static}}$ ($\parallel$), is larger than $\varepsilon^{\text{static}}(\perp)$. γ-Si_3N_4 displays optically isotropic behaviour. The absorption spectra of α-Si_3N_4, β-Si_3N_4 and γ-Si_3N_4 indicate transparency towards photons with energies below 5.0 eV as well as an increase in absorption which peaks at $9.0 - 9.5$ eV.

The vibrational modes of the crystalline Si_3N_4 polymorphs are established for the Γ-point in accordance with group theory. In α-Si_3N_4 14 A_1 and 27 E modes occur, which are both infrared and Raman active, as well as 14 inactive A_2 modes. The phonon wave numbers are in the range $193 - 1000$ cm^{-1}, with a gap between 671 cm^{-1} and 819 cm^{-1}. In the gap only 2 inactive A_2 modes are present, close to the low wave number end. β-Si_3N_4 displays 6 infrared active modes, $2A_u$ and 4 E_{1u}, 11 Raman active modes, 4 A_g, 2 E_{1g} and 5 E_{2g}, as well as 9 inactive modes, 3 B_g, 4 B_u and 2 E_{2u}. As in the α-phase, the high wave number phonons are separated by a gap from the low wave number phonons. Specifically, the phonon wave numbers in β-Si_3N_4 lie between $178 - 597$ cm^{-1} and $825 - 1029$ cm^{-1}. One Raman active A_g mode is centered in the gap at 706 cm^{-1} and an inactive B_g mode is located at the low wave number end of the gap. In γ-Si_3N_4, 4 infrared active T_{1u} modes, 5 Raman active modes, 1 A_{1g}, 1 E_g and 3 T_{2g}, as well as 7 inactive modes, 2 A_{2u}, 2 E_u, $1T_{1g}$ and 2 T_{2u}, are found between 304 cm^{-1} and 938 cm^{-1}, without any significant gap. The three inspected Si_3N_4 polymorphs mainly show contributions from Si atoms to vibrational modes at low wave numbers. Notably, the infrared active T_{1u} modes in γ-Si_3N_4 are dominated by the displacements of octahedrally coordinated Si^{oct} atoms. At high wave numbers contributions from N atoms to the vibrational modes in α-, β- and γ-Si_3N_4 are predominantly observed.

The VASP calculations with the regular potential POTCAR.SiN reproduce the properties of crystalline Si_3N_4 exceptionally well. In order to verify the accuracy of the optimized soft potentials POTCAR.Si_sN_{vs} (cut-off energy $E_{\text{cut}} = 200$ eV) and POTCAR.$Si_{vs}N_{es}$ (cut-off energy $E_{\text{cut}} = 160$ eV) for further application with the amorphous silicon-nitrogen alloys the results for the electronic and vibrational properties of the crystalline Si_3N_4 polymorphs are compared in chapter 4.

All three potentials confirm β-Si_3N_4 as the stable crystalline phase. A slight shift to higher ground state energies E_0 for softer potentials is observed in the three inspected polymorphs of crystalline Si_3N_4. Interestingly, the equilibrium volume V_0 of α- and β-Si_3N_4 obtained with the very soft potential POTCAR.$Si_{vs}N_{es}$ is closer to experimental findings than from calculations with the regular potential POTCAR.SiN. The equilibrium volume V_0 per formula unit with the very soft potential is established as 74.16 Å^3 in α-Si_3N_4, as 73.69 Å^3 in β-Si_3N_4 and as 59.35 Å^3 in γ-Si_3N_4. The results for E_0 and V_0 show sufficient consistency across the applied potentials. Thus a further comparison of the three crystalline phases is not necessary and β-Si_3N_4 is selected as reference structure. The full valence bandwidth obtained with the soft potential POTCAR.Si_sN_{vs} is the narrowest and therefore closest to other *ab-initio* calculations. The separating gap between upper and lower VB tends to increase with softer potentials, whereas the widths of upper and lower VB decrease. VB maximum and CB minimum are located between $\Gamma \rightarrow A$ and at the Γ-point, respectively, for all three potentials. The indirect Kohn-Sham PBE band gap, E_g min., and the direct

KS PBE band gap, E_g at Γ, are found to be in excellent agreement for the optimized soft potentials. It is observed that for softer potentials the KS PBE band gaps E_g min. as well as E_g at Γ tend to decrease. This difference is only small, less than 2 % for both optimized potentials.

For the zone center phonons of β-Si_3N_4 a comparison is conducted. The vibrational modes are in fair agreement for the three potentials, although the high wave number modes are shifted to higher values and low wave number modes come to be located at lower values for the potential POTCAR.Si_sN_{vs} and even more so for POTCAR.$Si_{vs}N_{es}$. The phonon type assignment and the relative order of phonons in calculations with the regular potential POTCAR.SiN are identical to those in the optimized soft potentials. An exception is the switching of positions of a A_g and a E_{2g} mode for the potential POTCAR.$Si_{vs}N_{es}$ around 442 cm^{-1}. From the calculations conducted with the optimized soft potentials it is concluded that both are suitable for VASP calculations of amorphous silicon nitride and silicon-nitrogen alloys.

The very soft potential POTCAR.$Si_{vs}N_{es}$ is selected for the calculations in chapter 5, due to the greater efficiency compared to the potential POTCAR.Si_sN_{vs} regarding computational time. The model structures of the amorphous silicon-nitrogen alloys are obtained from crystalline α-Si_3N_4, with approximately 200 atoms per super cell. More specifically, the super cells of a-Si, a-Si_3N, a-Si_3N_2, a-Si_3N_3, a-Si_3N_4, a-Si_3N_5, a-Si_3N_3:H, a-Si_3N_4:H and a-Si_3N_4:NH_3 are constructed by variation of the nitrogen and hydrogen content. *Simulated annealing* is performed in increments of -500 K starting at 5500 K. This high temperature guarantees rapid melting and equilibration. The structural and electronic properties are studied in detail for structures quenched (relaxed) from the melt.

The determination of the structural properties for the amorphous silicon-nitrogen alloys as well as a-Si includes mean square displacements and diffusion coefficients $D(t)$, the partial pair correlation functions, bond angle distributions and finally an analysis of the local environment. The volume per atom gradually decreases with increasing nitrogen content from 20.51 $Å^3$ in a-Si to 10.38 $Å^3$ in a-Si_3N_5, whereas the density ρ increases from 2.27 g/cm^{-3} in a-Si to 3.20 g/cm^{-3} in a-Si_3N_4 and then decreases to 3.08 g/cm^{-3} in the suprastoichiometric alloy a-Si_3N_5.

As dynamical properties the mean square displacements and from them the diffusion coefficients are calculated. Amorphous silicon nitride a-Si_3N_4 displays a constant small mean square displacement below 2000 K, which means that the structure is solid. At higher temperatures the mean square displacement begins to increase linearly with time, indicating a molten or liquid phase. Plateaus in the mean square displacement of a-Si_3N_4 are observed even at 2500 K, which shows that the structure spontaneously freezes in a configuration during the MD. Therefore higher temperatures are required in the simulations to avoid this. The onset of diffusion in a-Si_3N_4, at which the diffusion coefficient becomes sizeable ($D(t) = 0.1Å^2$/ps), is determined at a temperature of 3210 K. The substoichiometric alloys as well as the suprastoichiometric alloy exhibit a greater diffusivity, thus a lower temperature at which diffusion occurs. In a-Si_3N_3 the onset of diffusion is at 2580 K. The diffusion of hydrogen is evaluated separately from Si and N diffusivity. The hydrogenated alloys have a lower temperature at which diffusion is observed than the respective unhydrogenated alloys. In a-Si_3N_3:H diffusion of Si and N takes place upward of 2350 K and in a-Si_3N_4:H above 2740 K. Hydrogen is significantly more diffusive. In a-Si_3N_3:H hydrogen diffusion is present above 1650 K, whereas the onset of diffusion for H in a-Si_3N_4:H lies at

a slightly lower temperature, 1550 K.

Partial pair correlation functions and bond angle distributions are deduced by averaging over 200 sets of the MD evaluated at a a temperature below freezing, as monitored by the mean square displacement. *a*-Si displays a pair correlation function with a Si-Si bond length of 2.3 Å and a second nearest neighbor distance of 3.7 Å, in agreement with corner-sharing tetrahedral configuration. In the substoichiometric silicon-nitrogen alloys, in *a*-Si_3N_4 and in the inspected hydrogenated alloys the partial pair correlation functions indicate that the Si-N bond with an average length of 1.7 Å is dominant and no N-N bonds are observed. Merely in the suprastoichiometric silicon-nitrogen alloy *a*-Si_3N_5 true N-N bonds are observed at a distance of 1.6 Å in addition to the Si-N bonds at 1.7 Å. The Si-Si nearest neighbor peak at $2.3 - 2.4$ Å is indicative of either a true Si-Si bond or a nitrogen pair defect arranged in a quasi-planar square structure (Si-N-Si-N). It is found to decrease in the alloys with increasing nitrogen content in favour of the Si-Si second nearest neighbor peak at 2.9 Å. This tendency in the partial pair correlation functions, together with the N-N first neighbor peak at 2.7 Å, is evidence for mostly corner-sharing SiN_4 tetrahedra in the amorphous silicon-nitrogen alloys. The hydrogenated alloy *a*-Si_3N_3:H displays a lower Si-Si peak at 2.3 Å than *a*-Si_3N_3, pointing to curing of Si defects and reduction of Si-Si pairs as well as clusters through hydrogen. In the Si-rich alloy *a*-Si_3N_3:H, hydrogen bonds to nitrogen and to silicon, whereas in *a*-Si_3N_4:H and *a*-Si_3N_4:NH_3 hydrogen prefers nitrogen.

The bond angle distribution in the unhydrogenated as well as hydrogenated alloys shows a maximum at 117° for the Si-N-Si bonding unit and a maximum of 105° for the N-Si-N bonding unit. It is concluded that all inspected amorphous silicon-nitrogen alloys mainly contain SiN_4 tetrahedra and NSi_3 triangular units. To some extent a shoulder at 90° in the Si-N-Si distribution is found in all inspected alloys, which indicates a small number of the quasi-planar square structures that result from the presence of edge-sharing tetrahedra.

The analysis of the local environment concludes the calculation of the structural properties. In order to relate the findings to the interpretation of the electronic properties the focus is placed on the technically relevant alloys, *a*-Si_3N_3, *a*-Si_3N_4, *a*-Si_3N_3:H and *a*-Si_3N_4:H. Two aspects are considered, namely the occurrence of structural defects and the issue of random Si percolation networks including possible H induced curing. Structural defects are coordination defects, such as $Si_{[2]}$, $Si_{[3]}$, $Si_{[5]}$, $N_{[2]}$ and $N_{[4]}$, as well as defects originating from variations in bonding partners, such as the aforementioned square structures and Si-Si clusters with one or more Si-Si bond. In the Si-rich amorphous alloy *a*-Si_3N_3, significantly more coordination defects are observed than in amorphous silicon nitride *a*-Si_3N_4. Specifically, silicon defects dominate in *a*-Si_3N_3, whereas in *a*-Si_3N_4 nitrogen defects are mostly found. The hydrogenated alloys, *a*-Si_3N_3:H and *a*-Si_3N_4:H, display a greater number of undercoordinated Si and N atoms than the according unhydrogenated alloys. The only exception are twofold coordinated N atoms, which are less common in *a*-Si_3N_4:H than in *a*-Si_3N_4. No N-N bonds are found in any of these four alloys, thus Si-N, Si-Si as well as N-H in *a*-Si_3N_4:H and additionally Si-H in *a*-Si_3N_3:H occur. The formation of a Si percolation network is observed in *a*-Si_3N_3 and in *a*-Si_3N_3:H, albeit more in the unhydrogenated alloy. *a*-Si_3N_4:H displays a few randomly introduced Si-Si neighbors, whereas no such tendency is found in stoichiometric *a*-Si_3N_4. Hydrogen functions to restore the regular configuration of SiN_4 tetrahedra and NSi_3 triangular units in the Si-rich alloy *a*-Si_3N_3:H, but in *a*-Si_3N_4:H hydrogen increases the likelihood of Si-Si neighbors.

The inspected electronic properties are the density of states (DoS) and electronic gaps as well as the orbital-resolved partial density of states (PDoS) to obtain the electronic

levels in the vicinity of the gaps. The density of states of the amorphous alloys exhibits similarities to the DoS of the crystalline Si_3N_4 polymorphs. As in the crystalline phases, a lower VB and an upper VB, separated by a gap, is present. The upper VB shows the same electronic contributions that result in its three peak structure, although less distinct. The Kohn-Sham PBE band gap in the Si-rich alloy a-Si_3N_3, $E_g = 1.43$ eV, is significantly smaller than in a-Si_3N_4, $E_g = 2.79$ eV, due to tailing of levels into the gap. Hydrogenation induces a slight widening of the KS PBE band gap to 1.52 eV in a-Si_3N_3:H, whereas the addition of hydrogen to the stoichiometric alloys results in a small decrease of the KS PBE band gap to 2.61 eV in a-Si_3N_4:H. As there is less tailing into the gap in a-Si_3N_3:H than in a-Si_3N_3, but more in a-Si_3N_4:H than in a-Si_3N_4, it is concluded that incorporation of hydrogen into the Si-rich alloy cures defects, whereas it adds levels in the stoichiometric case. The hydrogenated alloy a-Si_3N_4:H shows Si-Si bonds, whereas in a-Si_3N_4 no such bonds are present. The curing effect of hydrogen is small compared to the change in the KS PBE band gap from substoichiometric a-Si_3N_3 to amorphous silicon nitride a-Si_3N_4, indicating stoichiometry as a primary factor determining the gap.

The orbital-resolved partial density of states in the amorphous silicon-nitrogen alloys show a high degree of hybridization, much as in the crystalline polymorphs of Si_3N_4. As is observed in the crystalline phases, the Si valence electrons form sp^3 hybrid orbitals and the N valence electrons display sp^2 hybridization as well as a non-bonding pair of N ($2p$) electrons. In a-Si_3N_3 the Si ($3p$) electrons dominate the VB maximum, whereas in a-Si_3N_4 the N ($2p$) electrons reside just below the top of the VB. Tailing of Si ($3s$) and ($3p$) electrons into the gap from the VB and tailing of all electronic contributions from the CB is found in a-Si_3N_3 as well as in a-Si_3N_3:H. H ($1s$) electrons mainly occur in the upper VB of the Si-rich alloy a-Si_3N_3:H, but in a-Si_3N_4:H they additionally contribute to the higher levels of the lower VB. The high degree of hybridization in the amorphous silicon-nitrogen alloys results in a low localization of electrons at any energy level. The addition of hydrogen to a-Si_3N_3 or a-Si_3N_4 decreases the localization further, thereby showing smearing of levels over the super cell.

A defect analysis of the highest occupied crystal orbital (HOCO) levels and lowest unoccupied crystal orbital (LUCO) levels as well as of gap states is carried out. Notably, in stoichiometric amorphous silicon nitride a-Si_3N_4 the N ($2p$) electrons at the HOCO originate from an undercoordinated $N_{[2]}$ atom and the Si ($3p$) electrons at the LUCO from an undercoordinated $Si_{[3]}$ atom. In the Si-rich alloy a-Si_3N_3, the main contribution at the HOCO arises from N ($2p$) electrons of a $N_{[3]}$ atom as well as from Si ($3p$) electrons of a $Si_{[4]}$ atom within the random percolation network. No gap states are observed in a-Si_3N_4 or a-Si_3N_4:H, whereas in a-Si_3N_3 and a-Si_3N_3:H some defect levels are located in the band gap. The lower gap states in a-Si_3N_3 consist of localized electrons from structural defects and the upper gap states as well as the LUCO in a-Si_3N_3 are mainly dominated by Si ($3s$) and ($3p$) electrons from Si atoms within the random percolation network. The gap states and the LUCO in a-Si_3N_3:H mostly originate from Si atoms in the network as well. Hydrogen atoms in the substoichiometric alloy a-Si_3N_3:H are found as nearest neighbor atoms to Si atoms with localizations at some gap states as well as at the HOCO. In a-Si_3N_4:H, where hydrogen prefers nitrogen as a bonding partner, the N atoms with localizations at the HOCO and immediately below possess hydrogen nearest neighbors. Additionally, Si-Si nearest neighbors are randomly introduced in a-Si_3N_4:H, similar as in a-Si_3N_3:H. A trend is observed, that the greater the number of Si atoms in the network, the more this appears to lead to a shrinking of the band gap. Therefore it is concluded that in the substoichiometric alloys a-Si_3N_3 and a-Si_3N_3:H the band gap is comparatively

small due to accumulation of energy levels within the gap, from electronic contributions of structural defects or of Si atoms that are located close to other Si atoms in clusters or in a random percolation network.

This work presents important physical properties of crystalline silicon nitride and of the amorphous silicon-nitrogen alloys from *ab-initio* calculations performed with VASP. It aims to function as a vantage point for further studies on this scientifically demanding and technologically interesting material.

Curriculum Vitae

Personal data

Name	Thomas Watts
Place and date of birth	Vienna, Austria, on February 20$^{\mathbf{th}}$, 1982
Nationality	AUT

Education

since WS 2004	University of Vienna – undergraduate course physics
WS 2003 to SS 2004	University of Vienna – undergraduate course astronomy
1997 to 2002	Secondary College for Chemical Technology Vienna, Specialization: Leather and Natural Matters. Diploma project: *Qualitative Comparison of Analytical Methods for Determination of Organic Carbon in Soils*, Gontarev/ Watts, cooperation with the University of Natural Resources and Applied Life Sciences, Vienna 2002

Internships

WS 2009/ SS 2010	University of Vienna, Prof. Georg Kresse, *computational quantum mechanics*
SS 2009	Technical University Vienna, Prof. Johann Summhammer, *solar cells*
WS 2008	University of Vienna, Prof. Georg Reischl, *electronics*
July 2008	Technical University Vienna, Prof. Johann Summhammer, *Determination of solar cell module characteristics by flash tester – Automation of the experimental setup with the software Flasher V.2*
SS 2007	University of Vienna, Prof. Michael Zehetbauer, *materials physics*
August 2000	Böhringer Ingelheim Austria, *quality control*
August 1999	Böhringer Ingelheim Austria, *SDS phoresis*

Languages

English	native speaker
German	mother tongue

Additional skills

Computer OS	Linux, MS Windows
Programming languages	C, Fortran, Visual Basic
Scripting languages	awk, bash

Vienna, December 2011

Bibliography

[1] M. A. Green, *High performance silicon solar cells*, Trans Tech SA, 1987.

[2] F. L. Riley, *Silicon nitride and related materials*, J. Am. Ceram. Soc. **83** (2000), 245–265.

[3] J. Robertson and M. J. Powell, *Gap states in silicon nitride*, Appl. Phys. Lett. **44** (1984), 415–417.

[4] K. Jarolimek, R. A. de Groot, G. A. de Wijs, and M. Zeman, *Atomistic models of hydrogenated amorphous silicon nitride from first principles*, Phys. Rev. B **82** (2010), 205201.

[5] G. Wiech and A. Simunek, *Analysis of the electronic and local structure of amorphous $SiN_x : H$ alloy films in terms of Si_K, Si_L, and N_K x-ray emission bands*, Phys. Rev. B **49** (1994), 5398–5405.

[6] M. M. Guraya, H. Ascolani, G. Zampieri, J. I. Cisneros, J. H. Dias da Silva, and M. P. Cantão, *Bond densities and electronic structure of amorphous $SiN_x : H$*, Phys. Rev. B **42** (1990), 5677–5684.

[7] L. Giacomazzi and P. Umari, *First-principles investigation of electronic, structural, and vibrational properties of a-Si_3N_4*, Phys. Rev. B **80** (2009), 144201.

[8] R. Jones, S. Öberg, F. Berg Rasmussen, and B. Bech Nielsen, *Identification of the dominant nitrogen defect in silicon*, Phys. Rev. Lett. **72** (1994), 1882–1885.

[9] F. de Brito Mota, J. F. Justo, and A. Fazzio, *Structural and electronic properties of silicon nitride materials*, Int. J. Quant. Chem. **70** (1998), 973–980.

[10] P. Hohenberg and W. Kohn, *Inhomogeneous electron gas*, Phys. Rev. **136** (1964), B864–B871.

[11] W. Kohn and L. J. Sham, *Self-consistent equations including exchange and correlation effects*, Phys. Rev. **140** (1965), A1133–A1138.

[12] N. W. Ashcroft and N. D. Mermin, *Solid state physics*, 1976.

[13] W. H. Press, S. A. Teukolsky, W. T. Vetterling, and B. P. Flannery, *Numerical recipes in FORTRAN: The art of scientific computing*, Cambridge University Press, 1992.

[14] M. Methfessel and A. T. Paxton, *High-precision sampling for Brillouin-zone integration in metals*, Phys. Rev. B **40** (1989), 3616–3621.

[15] P. E. Blöchl, O. Jepsen, and O. K. Andersen, *Improved tetrahedron method for Brillouin-zone integrations*, Phys. Rev. B **49** (1994), 16223–16233.

[16] P. E. Blöchl, *Projector augmented-wave method*, Phys. Rev. B **50** (1994), 17953–17979.

[17] G. Kresse and D. Joubert, *From ultrasoft pseudopotentials to the projector augmented-wave method*, Phys. Rev. B **59** (1999), 1758–1775.

[18] P. Pulay, *Convergence acceleration of iterative sequences. The case of SCF interation*, Chem. Phys. Lett. **73** (1980), 393–398.

[19] H. J. Monkhorst and J. D. Pack, *Special points for Brillouin-zone integrations*, Phys. Rev. B **13** (1976), 5188–5192.

[20] J. P. Perdew, K. Burke, and M. Ernzerhof, *Generalized gradient approximation made simple*, Phys. Rev. Lett. **77** (1996), 3865–3868.

[21] C.-M. Wang, X. Pan, M. Rohle, F. L. Riley, and M. Mitomo, *Silicon nitride crystal structure and observations of lattice defects*, J. Mater. Sci. **31** (1996), 5281–5298.

[22] A. Togo and P. Kroll, *First-principles lattice dynamics calculations of the phase boundary between β-Si_3N_4 and γ-Si_3N_4 at elevated temperatures and pressures*, J. Comput. Chem. **29** (2008), 2255–2259.

[23] M. Yashima, Y. Ando, and Y. Tabira, *Crystal structure and electron density of α-silicon nitride: Experimental and theoretical evidence for the covalent bonding and charge transfer*, J. Phys. Chem. B **111** (2007), 3609–3613.

[24] D. Hardie and K. H. Jack, *Crystal structures of silicon nitride*, Nature **180** (1957), 332–333.

[25] J. Z. Jiang, K. Stahl, R. W. Berg, D. J. Frost, T. J. Zhou, and P. X. Shi, *Structural characterization of cubic silicon nitride*, Europhys. Lett. **51** (2000), 62–67.

[26] P. Villars and L. D. Calvert, *Pearson's handbook of crystallographic data for intermetallic phases*, Vol. 3, 1985.

[27] Landolt-Boernstein, *Space group 159*, Springer Science+Business Media, 2010.

[28] H. Toraya, *Crystal structure refinement of α-Si_3N_4 using synchrotron radiation powder diffraction data: unbiased refinement strategy*, J. Appl. Cryst. **33** (2000), 95–102.

[29] UCL, *Space group 159 - symmetry operations*, University of London, 2010.

[30] Landolt-Boernstein, *Space group 176*, Springer Science+Business Media, 2010.

[31] P. Goodman and M. O'Keeffe, *The space group of β-Si_3N_4*, Acta Cryst. B **36** (1980), 2891–2893.

[32] O. Borgen and H. M. Seip, *The crystal structure of β-Si_3N_4*, Acta Chem. Scand. **15** (1961), 1789.

[33] S. N. Ruddlesden and P. Popper, *On the crystal structures of the nitrides of silicon and germanium*, Acta Cryst. **11** (1958), 465–468.

[34] B. Vassiliou and F. G. Wilde, *A hexagonal form of silicon nitride*, Nature **179** (1957), 435–436.

[35] P. Popper and S. N. Ruddlesden, *Structure of the nitrides of silicon and germanium*, Nature **179** (1957), 1129.

[36] Landolt-Boernstein, *Space group 173*, Springer Science+Business Media, 2010.

[37] R. Gruen, *The crystal structure of β-Si_3N_4; structural and stability considerations between α- and β-Si_3N_4*, Acta Cryst. B **35** (1979), 800–804.

[38] Y. Bando, *Weak asymmetry in β-Si_3N_4 as revealed by convergent-beam electron diffraction*, Acta Cryst. B **39** (1983), 185–189.

[39] D. du Boulay, N. Ishizawa, T. Atake, V. Streltsov, K. Furuya, and F. Munakatae, *Synchrotron x-ray and ab initio studies of β-Si_3N_4*, Acta Cryst. B **60** (2004), 388–405.

[40] R. Belkada, M. Kohyama, T. Shibayanagi, and M. Naka, *Relative stability of $P6_3/m$ and $P6_3$ structures of β-Si_3N_4*, Phys. Rev. B **65** (2002), 92104.

[41] R. Belkada, T. Shibayanagi, M. Naka, and M. Kohyama, *Ab-initio calculations of the atomic and electronic structure of β-silicon nitride*, J. Am. Ceram. Soc. **83** (2000), 2449–2454.

[42] UCL, *Space group 176 - symmetry operations*, University of London, 2010.

[43] Landolt-Boernstein, *Space group 227*, Springer Science+Business Media, 2010.

[44] C. Kocer, N. Hirosaki, and S. Ogata, *Ab-initio calculation of the ideal tensile and shear strength of cubic silicon nitride*, Phys. Rev. B **67** (2003), 35210.

[45] A. Zerr, G. Miehe, G. Serghiou, M. Schwarz, E. Kroke, R. Riedel, H. Füß, P. Kroll, and R. Böhler, *Synthesis of cubic silicon nitride*, Nature **400** (1999), 340–342.

[46] UCL, *Space group 227 - symmetry operations*, University of London, 2010.

[47] F. Birch, *Finite elastic strain of cubic crystals*, Phys. Rev. **71** (1947), 809–824.

[48] S. Zh. Karazhanov, P. Kroll, A. Holt, A. Bentzen, and A. Ulyashin, *Comparative analysis of electronic structure and optical properties of crystalline and amorphous silicon nitrides*, J. Appl. Phys. **106** (2009), 53717.

[49] J. C. Idrobo, H. Iddir, A. Ziegler, S. Ögüt, R. O. Ritchie, and N. D. Browning, *Ab-initio structural energetics of β-Si_3N_4 surfaces*, Phys. Rev. B **72** (2005), 241301.

[50] C. M. Fang, G. A. de Wijs, H. T. Hintzen, and G. de With, *Phonon spectrum and thermal properties of cubic Si_3N_4 from first-principles calculations*, J. Appl. Phys. **93** (2003), 5175–5180.

[51] A. E. H. Love, *A treatise on the mathematical theory of elasticity*, Dover Publications, 1944.

[52] Y.M. Li, M.B. Kruger, J.H. Nguyen, W.A. Caldwell, and R. Jeanloz, *High pressure x-ray diffraction study of β-silicon nitride*, Solid State Commun. **103** (1997), 107–112.

[53] W. Y. Ching, Y. N. Xu, J. D. Gale, and M. Ruhle, *Ab-initio total energy calculation of α- and β-silicon nitride and the derivation of effective pair potentials with application to lattice dynamics*, J. Am. Ceram. Soc. **81** (1998), 3189–3196.

[54] Y. Xu and W. Y. Ching, *Electronic structure and optical properties of α- and β-phases of silicon nitride, silicon oxynitride, and with comparison to silicon dioxide*, Phys. Rev. B **51** (1995), 17379–17389.

[55] C. Sénémaud, M. Driss-Khodja, A. Gheorghiu, S. Harel, G. Dufour, and H. Roulet, *Electronic structure of silicon nitride studied by both soft x-ray spectroscopy and photoelectron spectroscopy*, J. Appl. Phys. **74** (1993), 5042–5046.

[56] S.-D. Mo, L. Ouyang, W. Y. Ching, I. Tanaka, Y. Koyama, and R. Riedel, *Interesting physical properties of the new spinel phase of Si_3N_4 and C_3N_4*, Phys. Rev. Lett. **83** (1999), 5046–5049.

[57] J. Robertson, *Electronic structure of silicon nitride*, Philos. Mag. B **63** (1991), 47–77.

[58] L. Benco, *Crystal orbital scheme for Si_3N_4*, Ceram. Int. **24** (1998), 333–339.

[59] S. Y. Ren and W. Y. Ching, *Electronic structures of α- and β-silicon nitride*, Phys. Rev. B **23** (1981), 5454–5463.

[60] M. Gajdoš, K. Hummer, G. Kresse, J. Furthmüller, and F. Bechstedt, *Linear optical properties in the projector augmented-wave methodology*, Phys. Rev. B **73** (2006), 45112.

[61] J. Harl, *The linear response function in density functional theory: Optical spectra and improved description of the electron correlation*, Ph.D. Thesis, 2008.

[62] C. Bradley and A. Cracknell, *The mathematical theory of symmetry in solids: Representation theory for point groups and space groups*, Oxford Classic Texts in the Physical Sciences, Oxford University Press, 2010.

[63] N. Wada, S.A. Solin, J. Wong, and S. Prochazka, *Raman and IR absorption spectroscopic studies on alpha, beta, and amorphous Si_3N_4*, J. Non-Cryst. Solids **43** (1981), 7 –15.

[64] H. F. W. Dekkers, L. Carnel, G. Beaucarne, and W. Beyer, *Diffusion mechanism of hydrogen through pecvd $SiN_x : H$ for a fast defect passivation of mc-Si solar cells*, E-PVSEC Proceedings (2005).

[65] W. M. Arnoldbik, C. H. M. Marée, A. J. H. Maas, M. J. van den Boogaard, F. H. P. M. Habraken, and A. E. T. Kuiper, *Dynamic behavior of hydrogen in silicon nitride and oxynitride films made by low-pressure chemical vapor deposition*, Phys. Rev. B **48** (1993), 5444–5456.

[66] M. Ippolito and S. Meloni, *Atomistic structure of amorphous silicon nitride from classical molecular dynamics simulations*, Phys. Rev. B **83** (2011), 165209.

[67] J. J. Mei, H. Chen, W. Z. Shen, and H. F. W. Dekkers, *Optical properties and local bonding configurations of hydrogenated amorphous silicon nitride thin films*, J. Appl. Phys. **100** (2006), 73516.

[68] D. R. Lide (ed.), *Handbook of chemistry and physics*, 84$^{\text{th}}$ Edition, CRC Press, 2003.

[69] F. de Brito Mota, J. F. Justo, and A. Fazzio, *Structural properties of amorphous silicon nitride*, Phys. Rev. B **58** (1998), 8323–8328.

[70] R. J. Sokel, *The electronic structure of silicon nitride*, J. Phys. Chem. Solids **41** (1980), 899–906.

[71] R. K. Kalia, A. Nakano, K. Tsuruta, and P. Vashishta, *Morphology of pores and interfaces and mechanical behavior of nanocluster-assembled silicon nitride ceramic*, Phys. Rev. Lett. **78** (1997), 689–692.

[72] J. Robertson, W.L. Warren, and J. Kanicki, *Nature of the Si and N dangling bonds in silicon nitride*, J. Non-Cryst. Solids **187** (1995), 297–300.

[73] G. Pacchioni and D. Erbetta, *Electronic structure and spectral properties of paramagnetic point defects in Si_3N_4*, Phys. Rev. B **60** (1999), 12617–12625.

[74] S. Q. Wu, C. Z. Wang, Z. Z. Zhu, and K. M. Ho, *Structural and dynamical heterogeneity in molten si-rich oxides*, Appl. Phys. Lett. **96** (2010), 43121.

[75] F. de Brito Mota, J. F. Justo, and A. Fazzio, *Hydrogen role on the properties of amorphous silicon nitride*, J. Appl. Phys. **86** (1999), 1843–1847.

[76] R. Kaercher, L. Ley, and R. L. Johnson, *Electronic structure of hydrogenated and unhydrogenated amorphous SiN_x ($0 < x < 1.6$): A photoemission study*, Phys. Rev. B **30** (1984), 1986–1910.

[77] J. Bauer, *Optical properties, band gap, and surface roughness of Si_3N_4*, Phys. Status Solidi A **39** (1977), 411–418.

[78] A.N. Sorokin, A.A. Karpushin, V.A. Gritsenko, and H. Wong, *Electronic structures of silicon nitride revealed by tight binding calculations*, J. Non-Cryst. Solids **354** (2008), 1531–1536.

[79] E. A. Davis, N. Piggins, and S. C. Bayliss, *Optical properties of amorphous $SiN_x : H$ films*, J. Phys. C Solid State **20** (1987), 4415–4427.

[80] A. Iqbal, W. B. Jackson, C. C. Tsai, J. W. Allen, and Jr. C. W. Bates, *Electronic structure of silicon nitride and amorphous silicon/silicon nitride band offsets by electron spectroscopy*, J. Appl. Phys. **61** (1987), 2947–2954.

[81] H. Kurata, M. Hirose, and Y. Osaka, *Wide optical-gap, photoconductive a-$Si_xN_{1-x} : H$*, Jpn. J. Appl. Phys. **20** (1981), L811–L813.

[82] M. M. Guraya, H. Ascolani, G. Zampieri, J. H. Dias da Silva, M. P. Cantão, and J. I. Cisneros, *Electronic structure of amorphous Si-N compounds*, Phys. Rev. B **49** (1994), 13446–13451.